# Monitoring Microstructural Evolution of Alloy 617 with Non-Linear Acoustics for Remaining Useful Life Prediction; Multiaxial Creep-Fatigue and Creep-Ratcheting

## Fuel Cycle

**Dr. Cliff Lissenden**
Pennsylvania State University

**In collaboration with**:
North Carolina State University
Tuskegee University

Sue Lesica, Federal POC
David Hurley, Technical POC

**NEU P** Nuclear Energy University Programs

**U.S. Department of Energy**

**Project Title:**      Monitoring microstructural evolution of Alloy 617 with nonlinear acoustics for remaining useful life prediction; multiaxial creep-fatigue and creep-ratcheting 10-915

**Period:**         January 1, 2010 through August 30, 2014

**Report Date:**    October 30, 2014

**Recipient:**      Pennsylvania State University, North Carolina State University, Tuskegee University

**Award No.:**      00102946

**PI:**             Cliff Lissenden, (814) 863-5754, Lissenden@psu.edu

**Co-PIs:**         Tasnim Hassan, thassan@ncsu.edu
                    Vijaya Rangari, rangariv@tuskegee.edu

**TABLE OF CONTENTS**

# PART I. ABSTRACT

The research built upon a prior investigation to develop a unified constitutive model for design-by-analysis of the intermediate heat exchanger (IHX) for a very high temperature reactor (VHTR) design of next generation nuclear plants (NGNPs). Model development requires a set of failure data from complex mechanical experiments to characterize the material behavior. Therefore uniaxial and multiaxial creep-fatigue and creep-ratcheting tests were conducted on the nickel-base Alloy 617 at 850 and 950°C. The time dependence of material behavior, and the interaction of time dependent behavior (e.g., creep) with ratcheting, which is an increase in the cyclic mean strain under load-controlled cycling, are major concerns for NGNP design.

This research project aimed at characterizing the microstructure evolution mechanisms activated in Alloy 617 by mechanical loading and dwell times at elevated temperature. The acoustic harmonic generation method was researched for microstructural characterization. It is a nonlinear acoustics method with excellent potential for nondestructive evaluation, and even online continuous monitoring once high temperature sensors become available. It is unique because it has the ability to quantitatively characterize microstructural features well before macroscale defects (e.g., cracks) form. The nonlinear acoustics beta parameter was shown to correlate with microstructural evolution using a systematic approach to handle the complexity of multiaxial creep-fatigue and creep-ratcheting deformation. Mechanical testing was conducted to provide a full spectrum of data for: thermal aging, tensile creep, uniaxial fatigue, uniaxial creep-fatigue, uniaxial creep-ratcheting, multiaxial creep-fatigue, and multiaxial creep-ratcheting. Transmission Electron Microscopy (TEM), Scanning Electron Microscopy (SEM), and Optical Microscopy were conducted to correlate the beta parameter with individual microstructure mechanisms.

We researched application of the harmonic generation method to tubular mechanical test specimens and pipes for nondestructive evaluation. Tubular specimens and pipes act as waveguides, thus we applied the acoustic harmonic generation method to guided waves in both plates and shells. Magnetostrictive transducers were used to generate and receive guided wave modes in the shell sample and the received signals were processed to show the sensitivity of higher harmonic generation to microstructure evolution. Modeling was initiated to correlate higher harmonic generation with the microstructure that will lead to development of a life prediction model that is informed by the nonlinear acoustics measurements.

# PART II. OBJECTIVES, EFFORT, AND ACCOMPLISHMENTS

# 1. FULL STATEMENT OF OBJECTIVES

The research built upon a prior investigation to develop a unified constitutive model intended for design-by-analysis of the intermediate heat exchanger (IHX) for a very high temperature reactor (VHTR) design of next generation nuclear plants (NGNPs). Model development required a set of failure data from complex mechanical experiments to characterize the material behavior. Therefore uniaxial creep and multiaxial creep-fatigue and creep-ratcheting were conducted on the nickel-base Alloy 617 at temperatures of 850 and 950 °C. The time dependence of material behavior, and the interaction of time dependent behavior (e.g., creep) with ratcheting, which is an increase in the cyclic mean strain under load-controlled cycling, are major concerns for NGNP design.

This research project aimed at characterizing the microstructure mechanisms activated in Alloy 617 by mechanical loading and dwell times at elevated temperature. The acoustic harmonic generation method was researched for microstructural characterization. It is a nonlinear acoustics method with excellent potential for nondestructive evaluation, and even online continuous monitoring once high temperature sensors become available. It is unique because it has the ability to quantitatively characterize microstructural features well before macroscale defects (e.g., cracks) form. The nonlinear acoustics beta parameter was correlated to microstructural evolution using a systematic approach to handle the complexity of multiaxial creep-fatigue and creep-ratcheting deformation. Mechanical testing provided a full spectrum of data for: thermal aging, tensile creep, uniaxial creep-fatigue, multiaxial creep-fatigue, and multiaxial creep-ratcheting. Microscopy was conducted to correlate the beta parameter with individual microstructure mechanisms.

The four tasks that were performed in order to meet the overall objectives are listed below and provide the format for this final report. These are the tasks that were described in the original proposal.

- Material microstructure evolution: mechanical testing to generate strain localization, creep cavitation, and thermal aging
- Nonlinear acoustics methodology, experimental procedures, and results
- Microstructural evaluation
- Constitutive model development based on measurable microstructural variables

# 2. DESCRIPTION OF EFFORT PERFORMED

This section summarizes the key elements of the work performed over the course of the project. It is separated into four subsections based on the objectives described in the previous section: material microstructure evolution, nonlinear acoustics, microstructural characterization, and model development. In order for this report to be complete and self-contained as well as direct and concise, where portions of the work have been described completely elsewhere they are included as appendices.

**Detailed Table of Contents**

**2.1 Material Microstructure Evolution**

Alloy 617 plate from Heat QA101053 was supplied by Laura Carroll (Idaho National Laboratory). All specimens were machined from these samples either at Penn State or by Westmoreland Mechanical Testing and Research. All mechanical testing was performed at Penn State.

*2.1.1 Thermal Aging*

Samples 10 mm x 13.5 mm x 38 mm were thermally aged in air at 950°C for times of 0, 312, 624, 936, and 1248 hours. These samples were evaluated with nonlinear acoustics and then sectioned for transmission electron microscopy.

*2.1.2 Creep*

*Introduction*

Inconel 617 is a candidate material for at least the Intermediate Heat Exchanger of the Very-High Temperature Reactor, which is one of the pending Generation IV Nuclear Reactor designs. The components would involve operating temperatures as high as 850°C to 1000°C, with the intention to increase the efficiency of energy production by increasing the input and output temperature difference. This solid-solution strengthened nickel-based superalloy has very good corrosion, oxidation and creep resistance due to the contributing alloying components as provided with Table 2.1.2.1. [1]. The first two properties mentioned are due to the presence of nickel and chromium. In addition, the supplements of cobalt and molybdenum allow the superalloy to retain high strength.

**Table 2.1.2.1.** *Limiting chemical composition of Alloy 617 in weight % [1].*

| Ni | Cr | Co | Mo | Al | C | Fe | Si | Ti | Mn |
|---|---|---|---|---|---|---|---|---|---|
| 44.5 (min) | 20.0-24.0 | 10.0-15.0 | 8.0-10.0 | 0.8-1.5 | 0.05-0.15 | 3.0 (Max) | 1.0 (Max) | 0.6 (Max) | 1.0 (Max) |

There have been other studies regarding the creep behavior of Alloy 617 and other potential alloys of similar composition for this application, with analysis regarding the mechanical strength and the microstructural evolution. The main objective of this study is to produce samples of sufficiently varying creep mechanisms and degradation level to correlate measured second harmonics from nonlinear ultrasonics with the microstructure observed through optical and transmission electron microscopy. The samples were conducted for two test sets, either at 950°C or 850°C, and both at an initial nominal stress of approximately 35% of the yield strength at the corresponding temperature. This report will focus on the mechanical testing and results of these two creep test sets.

ASTM E139, the standard test methods for conducting creep, creep-rupture, and stress-rupture tests of metallic materials was followed when possible. Unfortunately, we had to load the specimens before heating, which is not standard practice. This was due to the fixture type used to load the specimens. Addition of the weights typically jars the load train and can cause the LVDT (linear variable differential transducer) supports to slip off the specimen tabs.

*Literature Review and Background*

Uniaxial creep tests involve applying a constant load, where the resulting stress is lower than the yield strength. The plot of the measured engineering strain as a function of time can usually be divided into three states: primary (transient), secondary (steady state), and tertiary stages, based on the strain rate trends as seen in Figure 2.1.2.1. Within each stage, certain deformation mechanisms typically occur and eventually lead to void formation, necking and rupture.
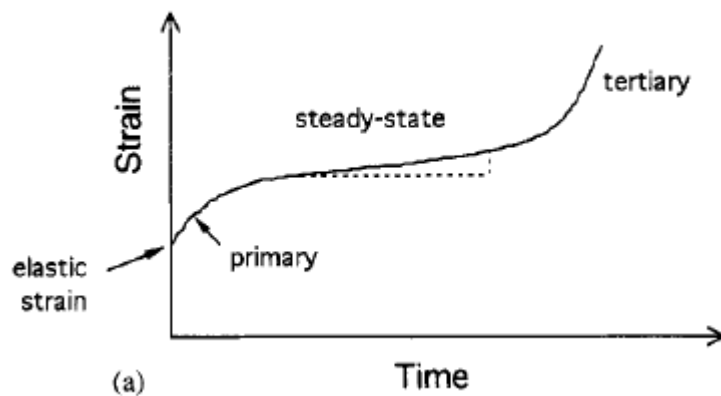


**Figure 2.1.2.1.** *Typical creep curve, with three stages characterized by strain rate, taken from [2].*

Since the steady-state regime usually occurs over most of the curve, the minimum strain rate during this stage is usually recorded and compared for experiments conducted over a range of stresses for one temperature, to determine the stress exponent "n". This exponent is typically taken to be the slope of the minimum strain rate versus the applied stress log-log plot. The following is a general relation between the minimum strain and the following parameters: applied stress σ, stress exponent n, activation energy for creep mechanism Q, the universal gas constant R, absolute temperature T, and a constant A.

$$\dot{\varepsilon} = A\sigma^n \exp\left(\frac{-Q}{RT}\right)$$

Analyzing the microstructure from creep experiments that have identical test parameters (temperature and stress) but are interrupted at different times enables study of the progression of deformation mechanisms and correlation with the generation of second harmonics from nonlinear acoustics tests. Nonlinear acoustics tests are conducted on the crept samples and then the microscopy can be conducted to correlate the second harmonic with the microstructural features observed. Features such

as grain size (grain boundary density) and the relative location and size of precipitates have been noted in other studies to influence dislocation climb and diffusion mechanisms.

The microstructures obtained in the experiments conducted for this report could also be compared to previous literature sources. Chomette et al [3] have conducted creep tests at stresses of 70 MPa at 850°C and 30MPa at 950°C, and analyzed the influence between aging, cold working of 20% and as received conditions provided by Special Metals, Inc. They have tested on cylindrical specimens with the gage length and gage diameter of 30 mm and 5 mm respectively for testing in air, while 25 mm and 6 mm were used in vacuum. They had gradually applied weights with a mean loading rate of approximately 1.4-2 Ns$^{-1}$, at test temperatures of 850°C and 950°C. With those experiments, they have observed some boundary migrations, recrystallization, and specific growth and location of carbides such as $M_6C$, Ti(C,N), and $M_{23}C_6$ carbides depending on the specimen treatment and creep test temperature. In addition, Chomette et al [3] also compared the microstructure at two different locations relative to the rupture zone as shown in Figure 2.1.1.2. Thus, observed features depend on the selection of the sample area for optical microscopy or transmission electron microscopy (TEM).
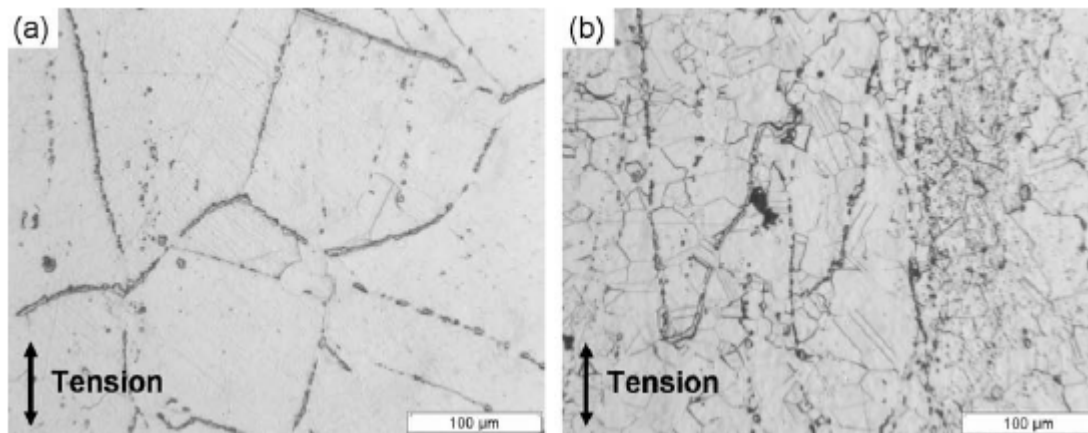


*Figure 2.1.2.2. Crept sample of as received Alloy 617 after rupture at 950°C at test stress of MPa from Chomette et al [3]. Microstructure of sample taken: (a) far from rupture zone, which had low reduction in area, (b) near the rupture zone, which had high reduction in area.*

*Experimentation*

  *Specimen and Fixture*

For the creep tests, dog-bone-shaped specimens were machined out of a 38 mm thick annealed and hot rolled plate, which was supplied by the Idaho National Laboratory (heat QA101053) The chemical composition was determined by Carroll et al [4] and is shown in Table 2.1.2.2. Specimens were machined to have the tensile loading axis along the rolling direction. The original creep sample design had to be altered because the original loading pin was undersized.

**Table 2.1.2.2.** *Composition in weight % for Alloy 617 [4].*

| Ni | Cr | Co | Mo | C | Fe | Al | Ti | Si | Mn | Cu |
|---|---|---|---|---|---|---|---|---|---|---|
| Balance | 21.9 | 11.4 | 9.3 | 0.08 | 1.7 | 1.0 | 0.3 | 0.1 | 0.1 | 0.04 |

The altered creep sample is shown in Figure 2.1.2.3. The modifications include horizontal bearing surfaces and a reduced gage section that is 6 mm x 10 mm instead of 10 mm x 10 mm. The end fixtures for the creep samples have horizontal bearing surfaces as shown in Figure 2.1.2.4 and are machined from Alloy 617. The fixtures are drilled and tapped for threaded rods that protrude out of the furnace.
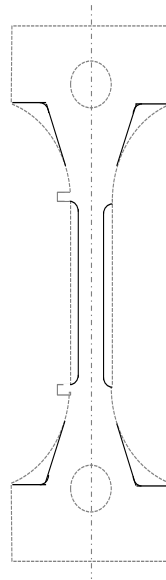


**Figure 2.1.2.3.** *Schematic of creep samples. The gage section is 6 mm by 10 mm by 38 mm long. Tabs are provided for mounting the LVDT cage.*
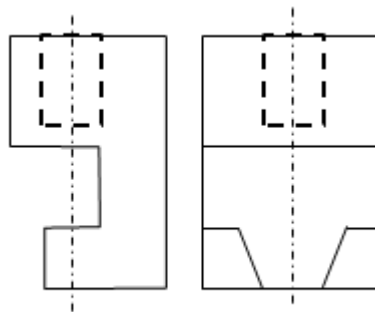


**Figure 2.1.2.4.** *Side and front views of the fixture having horizontal bearing surfaces. The top of the fixture is drilled and tapped for a threaded rod.*

The fixture shown in Figure 2.1.2.4 was used for creep tests until specimen C03 ruptured at a lower strain value than specimen C02 under the same temperature and load conditions. The setup was examined, a slight bend with the top fixture was noticed, which introduced a bending component to the

loading, which most likely would have been more than 10% of the axial load. Additional experiments were conducted with a stiffened version of the fixture as shown in Figure 2.1.2.5. All experiments starting with specimen C04 used this fixture design.
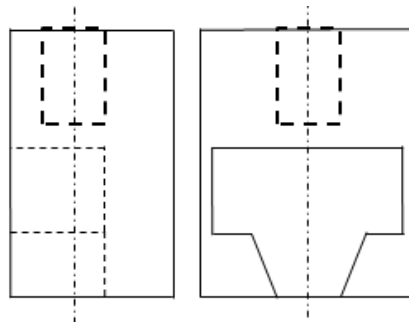


**Figure 2.1.2.5.** *Stiffened top fixture design prevented bending.*

Hexagonal Boron Nitride (hBN) Aerosol Spray, manufactured by M. K. Impex Corp, was applied on all essential contact surfaces to prevent mating surfaces from fusing together. It is a high temperature anti-stick release agent and lubricant, noted to have good chemical inertness, which is stable up to temperatures as high as 1000°C in air.

*Heating Apparatus and Loading Rig*

An Arcweld creep loading rig, model f-6: serial je-1883-j, with a 20:1 amplification of dead weight to applied force was employed and equipped with a furnace with a control panel, with a dial meter that allows the input of the set temperature and the monitoring of the furnace temperature. The cylindrical furnace is capable of heating to 2200°F and has a through-hole channel that allows the load train and specimen to slide through. This type of furnace exposes the specimen to air, and solid insulation tiles were used to cover both top and bottom gaps around the loading train.

*LVDT and Data Acquisition*

The two tabs located on one side of each creep sample provide the means for attachment of the LVDT frame. The hardware involved in the data acquisition is the following: an omega LDX-3A LVDT signal conditioner, NI SCB-68 connector block, and an NI data acquisition card. A custom written Labview program was used to record the voltage output once every ten minutes after averaging 50 readings.

*Temperature*

For these experiments, thermocouple type K (manufactured by Omega Engineering, Inc) with original glass braid insulation was used. The special limits of error for thermocouple accuracy is +/- 1.1°C or 0.4%, and has a temperature range of 0 – 1250°C (32 to 2282°F). The original thermocouple insulation was replaced by ceramic thermocouple insulators, a thin extruded Omegatite 200 rod with two holes and manufactured by Omega Engineering, Inc. The rod secured the thermocouples to the LVDT frame and prevented short circuit. It is operational at high temperatures up to 1650°C ( 3000°F). The insulator

has an outside diameter of 1/8" and each hole with a diameter of 0.040". Composition of the ceramic tubing is approximately 80% Mullite and 20% Glass, and exact chemical constitution is provided in [5].

Various devices were used to monitor the specimen temperature during the experiment. Initially, either the Micromega external temperature controller or the Mastech MS8264 Digital Multimeter was used, however the temperature reading was less than optimal. For most and the later experiments starting with specimen C08, the HH506RA Multilogger thermometer was used to monitor the temperature at two locations, with one thermocouple attached to the center of the specimen and another used to measure the ambient furnace temperature within ¾" of the specimen. Through these devices, the specimen temperature was monitored, which enabled adjustments to the furnace set temperature to be made.

*Experimental Procedure*

1.  Dimensions of the specimen are measured.

2.  A thermocouple wire is spot-welded to the center of the gage section

3.  Contact surfaces are sprayed with the boron nitride aerospray

4.  The load train was assembled by attaching the Nicrotung bars to the Alloy 617 fixtures with the specimen in place. A crescent-shaped Alloy 617 disk with a groove slides onto each of the tabs located at the end of the gage section of the specimen. The LVDT frame is secured onto these disks with set screws. Thus, the metal components that are in immediate contact with the specimen are all Alloy 617.

5.  The specimen is first loaded with the appropriate amount of dead weight on the creep rig, to ensure that the specimen does not slip out of disks that mount the LVDT. The Labview data acquisition program is activated, then heating the specimen is started.

6.  The furnace portion of the rig is adjusted so that the center approximately coincides with the center of the specimen gage section. Initially the set temperature for the furnace is fixed at about 20% greater than the intended test temperature. Approximately an hour and a half later, when the specimen temperature reading would be about 100°C lower than the intended test, the furnace temperature is set to a temperature about 7% higher than the intended test temperature. For the rest of the duration of the experiment, the furnace set temperature sometimes requires minor adjustment to ensure the specimen temperature remains at the intended test temperature.

7.  Typically, the heating is ceased and load is removed once the specimen has ruptured (automatically due to machine interlock) or once the specimen has accumulated the intended/desired strain (manually by operator). Once the specimen has cooled to room temperature or approximately 50°F, the load train can be removed from the rig and be disassembled. The sooner it is disassembled, the easier it is to get pieces apart.

*Test Matrix*

There were two sets of test types conducted for Alloy 617, with temperature being the main test parameter. Our partner from North Carolina State University, Dr. Hassan, analyzed monotonic tension data and determined the yield strength to be 120 and 200 MPa at 950°C and 850°C respectively. Experiments with initial nominal stresses of 44MPa and 69 MPa, equivalent to approximately 35% of the yield strengths at 950°C and 850°C respectively, are conducted. These values are comparable to Roy et al [6], who reported yield strengths of 184 and 236 MPa for 950°C and 850°C respectively. The test matrix for the completed experiments is given in Table 2.1.2.3. Predetermined nominal stress values were used to determine the required dead load to apply to the creep rig, which has a 20:1 lever arm.

**Table 2.1.2.3.** *Creep test parameters.*

| Temperature (°C) | Yield Strength (MPa) | % of Yield Strength | Nominal Stress (MPa) | Area (mm$^2$) | Applied Force (N) | Dead Load (N) |
|---|---|---|---|---|---|---|
| 950 | 120 | 36.6 | 44 | 60 | 2640 | 132 |
| 850 | 200 | 34.7 | 69 | 60 | 4140 | 207 |

* indicated cross-sectional area is the average value for the corresponding set of experiments.

The test plan was to conduct the initial creep tests to rupture, a strain of 50%, or for 1200 hours (50 days), whichever came first. After that, replicate tests were conducted, but these were interrupted at 60% and 30% of the strain obtained in the initial test. Results from the mechanical testing are presented in the next section, while results from the microstructural investigation and the nonlinear acoustics experiments will be presented in a subsequent report.

*Results and Discussion*

*Creep at ~44 MPa at 950°C*

For the test set at 950°C, the initial nominal stress was 44 MPa, about 35% of the assumed yield strength at 950°C (120 MPa). An anomalous strain behavior occurs during the initial heating phase. With the first experiment of this set on specimen C02, the axial strain increased to 0.05%, decreased, and then increased again as shown in Figure 2.1.2.6.
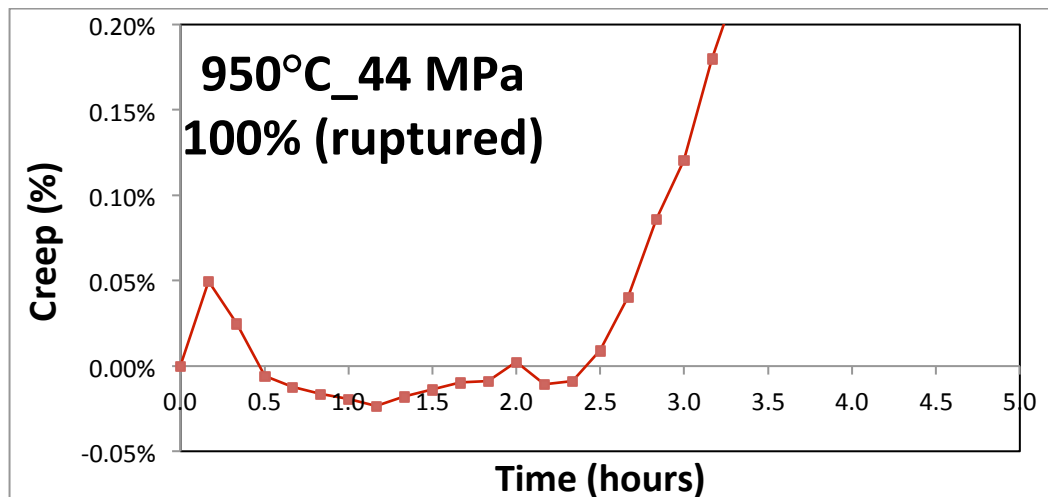
**Figure 2.1.2.6.** *Initial strain during the heating (under load) from room temperature to about 950°C.*

The steady accumulation of strain did not occur until approximately 2.5 hours after the furnace was turned on. This initial strain response is typical of all tests to a reasonable degree and is likely associated with seating of the LVDT and thermal stabilization of the load train and LVDT cage.

There are two notable constant strain rates before tertiary creep occurred with Figure 2.1.2.7; a slightly faster creep rate starts after ~20 hours. Comparison with the temperature log and creep trends shows that the change in creep rate was due to a slightly higher temperature, and will be discussed in a latter section. After 66.2 hours the specimen ruptured at an elongation of 24.40% and true strain of 21.83%, computed by ln(1+e).
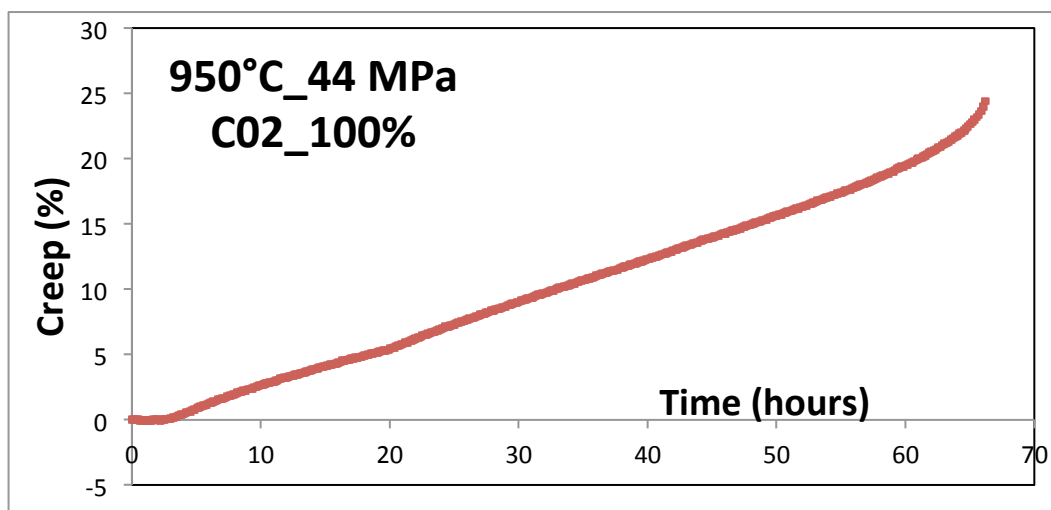


**Figure 2.1.2.7.** *Engineering creep strain as a function of time for specimen C02 at 950°C under 44 MPa. The test ended in rupture at 24.4% strain.*

Other experiments were conducted at 950°C and with the same stress of 44 MPa, with some deviation from the creep curve. These additional tests were interrupted at strains of 7.32, 14.64, and 18.06% (i.e., 30, 60, and 74% of the rupture strain). The specimens interrupted at 30% and 74% of the rupture strain, have very similar creep rates and are slightly different from the other two specimens, which have slower creep rates as shown in Figure 2.1.2.8. It is likely that the different creep rates, which are computed in Table 2.1.2.4, are associated with presence of slightly different temperatures during the experiments.
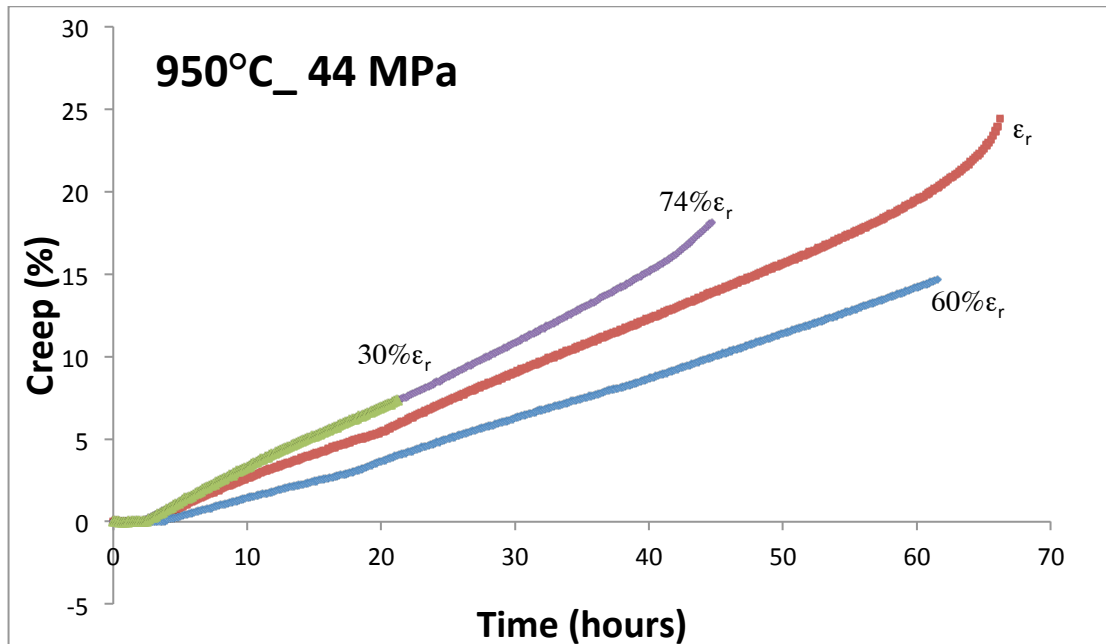


*Figure 2.1.2.8. Engineering strain of the test set at 950°C and 44 MPa. Specimen C02 is the ruptured test, and the others are interrupted.*

*Table 2.1.2.4.* *Notable creep rates present within Test Set 1: 950°C and 44 MPa.*

| % of rupture stain | specimen | Creep rate computation times (hrs) | | | creep rate (s$^{-1}$) | Intercept of tangent line w/strain axis@ zero time |
|---|---|---|---|---|---|---|
| | | Start | End | Duration | | |
| 100 | C02 | 2.8 | 15.7 | 12.8 | 8.6E-07 | 0.0052 |
| | | 19.0 | 52.8 | 33.8 | 9.4E-07 | 0.0109 |
| 60 | C04 | 30.0 | 105.0 | 75 | 5.8E-07 | 0.0069 |
| | | 117.0 | 229.0 | 112 | 6.9E-07 | 0.0136 |
| | | 253 | 358 | 105 | 7.5E-07 | 0.0228 |
| 30 | C05 | 4 | 7 | 3 | 1.3E-06 | 0.0103 |
| | | 7.17 | 20.67 | 13.5 | 1.0E-06 | 0.0032 |
| 75 | C06 | 30 | 105 | 75 | 1.1E-06 | 0.0078 |
| | | 117 | 193 | 76 | 1.1E-06 | 0.0109 |

*Table 2.1.2.5.* *Experimental details for Test Set 1: 950°C and 44 MPa.*

| Specimen | % of Strain Rupture | Eng. Strain at Load Removal (%) | Eng. Strain after cooling (%) | Final true strain value (%) | Initial thermal strain + loading strain (%) | Time and Temp.at 0.05% strain [Hr] (°C) | Time to heat to 950°C [Hr] (°C)** | Test/ Load time (Hr) |
|---|---|---|---|---|---|---|---|---|
| C02 | 100% | 24.40* | ruptured | 21.83 | -0.02 to 0.05 | 2.7 (920) | 3.6 (948) | 66.2 |
| C04 | 60% | 14.66 | 14.68 | 13.68 | -0.04 to 0.02 | 3.9 (955) | 3.8 (948) | 61.5 |
| C05 | 30% | 7.34 | 7.26 | 7.08 | -0.02 to 0.04 | 2.4 (950) | 2.5-2.8*** | 21.2 |
| C06 | 74% | 18.15 | 18.19 | 16.68 | -0.03 to 0.04 | 2.3 (890) | 3.5 (954) | 44.7 |

*last recorded elongation value before rupture

\*\*the specimen temperature at the time indicated

\*\*\*temperature log during this duration is unavailable

As shown in Table 2.1.2.5, the time required for the specimen to heat to approximately 950°C is variable. Figure 2.1.2.9 shows the initial strain versus time for the first 4.5 hrs of testing. There is a variability of up to 2 hrs in terms of when creep strain began to accumulate at a significant rate.
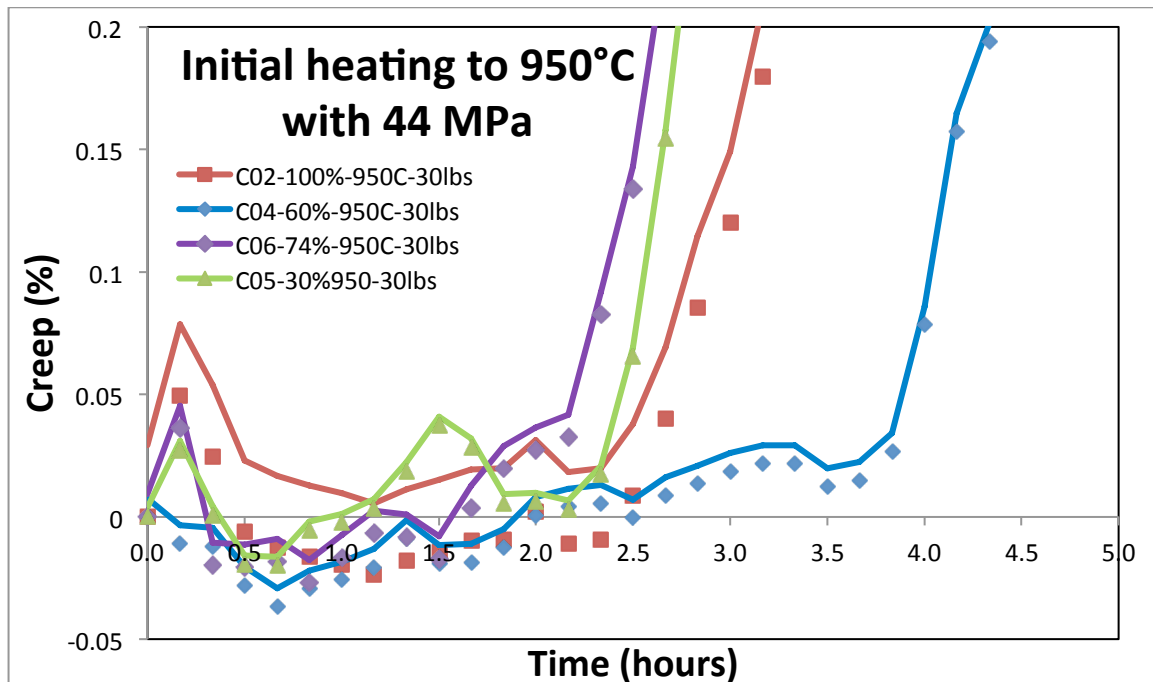


**Figure 2.1.2.9.** *Initial strain during the heating from room temperature to about 950°C.*

Specimen dimensions are provided in Table 2.1.2.6. Typically there is a small necked (localized deformation) region within a distance of 20 mm from the upper tab of the gage section for the specimens that reached at least 60% of the ruptured strain value. An approximate true stress at rupture was estimated based on the dimensions measured after the specimen cooled to room temperature. The smallest cross-sectional area for the ruptured specimen was 4 mm by 8 mm, which results in a true stress of ~ 79.2 MPa.

**Table 2.1.2.6.** *Specimen dimensions before and after creep experiment. All measurements were made at room temperature.*

| | | Initial cross-section | | Final minimum cross-section | | | |
|---|---|---|---|---|---|---|---|
| Strain % | Specimen | Dimensions (inches) | Area (in²) | Dimensions (inches) | Area (in²) | True Stress (MPa) | Area reduct %* |
| 100 | C02 | 0.238x0.394 | 0.0938 | 0.175 x 0.296 | 0.0518 | 79.2 | 44.8 |
| 60 | C04 | 0.238x0.394 | 0.0938 | 0.205 x 0.357 | 0.0732 | 56.0 | 21.9 |
| 30 | C05 | 0.238x0.391 | 0.0931 | 0.226 x 0.372 | 0.0841 | 48.8 | 9.7 |
| 74.4 | C06 | 0.237x0.391 | 0.0927 | 0.2125 x 0.351 | 0.0746 | 55.0 | 19.5 |

*Typically area reduction is only reported for specimens with circular cross-sections, but could be used as general comparisons for these samples.

Deformation localization as measured by reduction in area (Table 2.1.2.6) follows the trend expected based upon amount of creep strain, except samples C04 and C06, to 60 and 74% of the creep rupture strain exhibited almost the same reduction in area.

The measured percent elongation after the specimen has cooled back to room temperature is slightly higher than the measured strain from the LVDT, as shown in Table 2.1.2.7. The LVDT strain value is measured after the load has been removed and when the sample is cooling. These measurements are deemed to be sufficiently accurate for our intended purpose.

**Table 2.1.2.7.** *Creep sample elongation.*

| Percent of strain to rupture in C02 | Specimen | Initial gage length (in) | Final gage length (in) | $100(L_f - L_i)/L_i$ (%) | LVDT strain (%) |
|---|---|---|---|---|---|
| 100 | C02 | 1.580 | 2.042 | 29.24 | 24.40 |
| 60 | C04 | 1.578 | 1.842 | 16.73 | 14.66 |
| 30 | C05 | 1.578 | 1.757 | 11.34 | 7.34 |
| 74 | C06 | 1.575 | 1.871 | 18.79 | 18.15 |

Test Set 2: ~69 MPa at 850°C

For test set 2 the test temperature as 850**°C** and the nominal stress is 69 MPa, about 34.7% of the yield strength (200 MPa). During the initial heating phase to 850**°C** given in Figure 2.1.2.10, there was also variation in strain accumulation akin to that shown in Figure 2.1.2.9. After 164.2 hours, specimen C08 ruptured at a nominal strain of 23.97 % (true strain of 21.49%).
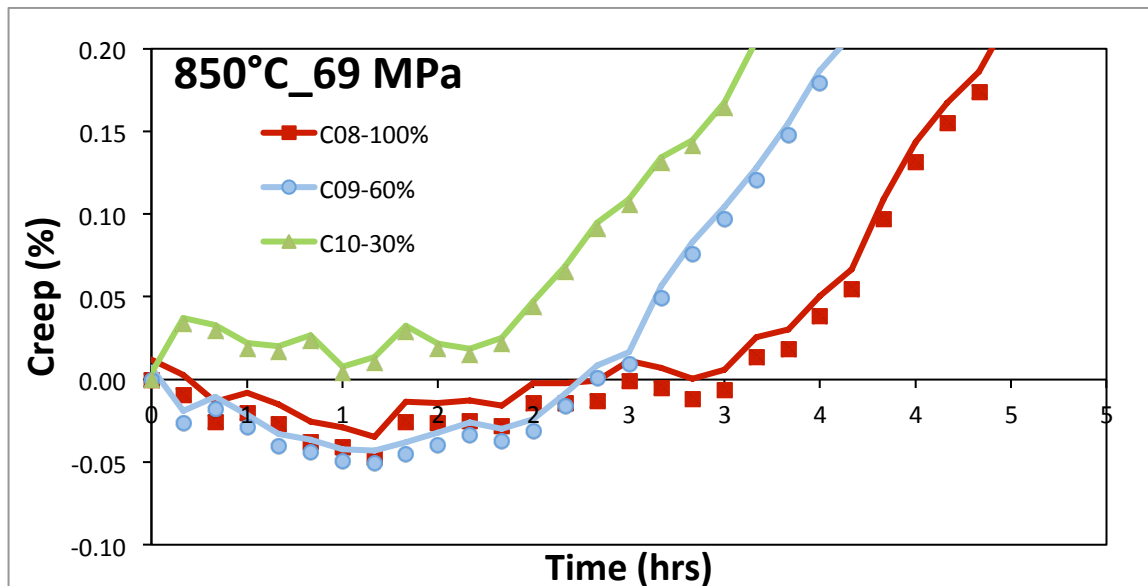


**Figure 2.1.2.10.** *Strain during the initial heating from room temperature to approximately 850°C.*

The creep curves within this test set of 850**°C** and 69 MPa shown in Figure 2.1.2.11 are more consistent than those of the test set at 950**°C** and 44 MPa (Figure 2.1.2.8). For this test set, specimen C08 was crept until rupture. For this set of experiments, 850**°C** and 69 MPa, the HH506RA Multilogger thermometer was used to record the temperature reading from two locations. One thermocouple was spot welded to the center of the specimen's gage length (T1), and another connection was used to measure the ambient temperature of the furnace with its initial position about 10 mm from the specimen and slightly higher than the center of the specimen's gage length (T2).
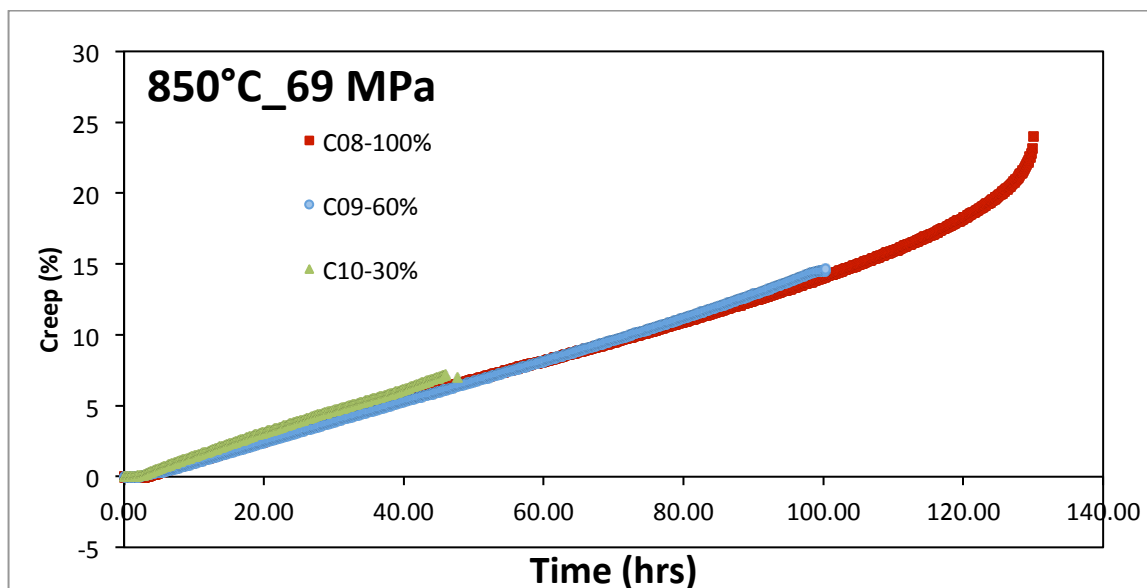
**Figure 2.1.2.11.** *Creep strain as a function of time for test set 2, at 850°C and ~69MPa. Specimen C08 crept to rupture, while Specimens C09 and C10 were interrupted.*

The durations of constant creep during each experiment of test set 2 (850°C and 69 MPa) are provided in Table 2.1.2.8. The constant creep rates of these experiments are fairly close, compared to those of test set 1 (950°C at 44 MPa), and thus could perhaps be more representative of the development of creep damage as there is less variability. In addition, for each experiment of test set 2, the time required to reach 0.05% strain varied between 2-3.5 hours, as seen in Table 2.1.2.9.

**Table 2.1.2.8.** *Creep rates for Test Set 2, 850°C at ~69 MPa.*

| % of rupture stain | specimen | Creep rate computation times (hrs) | | | creep rate ($s^{-1}$) | Intercept of tangent line w/strain axis@ zero time |
|---|---|---|---|---|---|---|
| | | Start | End | Duration | | |
| 100 | C08 | 4.5 | 32.8 | 28.3 | 4.2E-07 | 0.0044 |
| | | 38.2 | 92.8 | 54.6 | 3.9E-07 | 0.0015 |
| 60 | C09 | 4.8 | 65.7 | 60.9 | 3.9E-07 | 0.0046 |
| | | 69.3 | 93.7 | 24.4 | 4.4E-07 | 0.0182 |
| 30 | C10 | 2.8 | 24.5 | 21.7 | 4.7E-07 | 0.0027 |
| | | 27.0 | 36.2 | 9.2 | 3.9E-07 | 0.0040 |
| | | 39.5 | 44.7 | 5.2 | 5.0E-07 | 0.0088 |

**Table 2.1.2.9.** *Experimental details for Test Set 2 at 850°C and ~69 MPa.*

| Specimen | % of Strain Rupture | Eng. Strain at Load Removal (%) | Eng. Strain after cooling (%) | Final true strain value (%) | Initial thermal strain + loading strain (%) | Time and Temp.at 0.05% strain [Hr] (°C) | Time to heat to 850°C [Hr] (°C) | Test/ Load time (Hr) |
|---|---|---|---|---|---|---|---|---|
| C08 | 100% | 23.97 | n/a | 21.49 | -0.05 to 0.00 | 3.5 (849) | 3.4 (849) | 164.2 |
| C09 | 60% | 14.42 | 14.64 | 13.47 | -0.05 to -0.02 | 2.6 (842) | 2-3.4 (846) | 98.5 |
| C10 | 30% | 7.19 | 7.01 | 6.95 | 0.00 to 0.03 | 2.0 (847) | 2.1 (860) | 46.0 |

The dimensions and area of the minimum cross section of the specimens were measured at room temperature as before and the results are given in Table 2.1.2.10. The ruptured specimen C08 and C09 had a small region of necking near the top edge of the gage section. As expected the reduction of area is significantly larger for sample C08 than for C09 and C10 (since these two tests were interrupted). The true stress is estimated from the measured dimensions at room temperature.

**Table 2.1.2.10.** *Specimen dimensions before and after creep experiment. All measurements were made at room temperature.*

| Strain % | Specimen | initial cross sectional | | final minimum cross-sectional | | | |
|---|---|---|---|---|---|---|---|
| | | Dimensions (in) | Area (in²) | Dimensions (in) | Area (in²) | True Stress (MPa) | Area reduction % |
| 100 | C08 | 0.236 x0.391 | 0.09228 | 0.153 x 0.290 | 0.04437 | 144.5 | 51.9 |
| 60 | C09 | 0.236 x0.391 | 0.09228 | 0.212 x 0.351 | 0.07441 | 86.2 | 19.4 |
| 30 | C10 | 0.237 x0.391 | 0.09267 | 0.225 x 0.371 | 0.08348 | 76.8 | 9.9 |

The corresponding elongation (%) from the dimensions measured after cooling are slightly higher than the LVDT measured strain as shown in Table 2.1.2.11, which were recorded when the specimen was still just beginning to cool.

***Table 2.1.2.11.*** *Creep sample elongation.*

| Percent of strain to rupture in C08 | Specimen | Initial gage length (in) | Final gage length (in) | $100(L_f - L_i)/L_i$ (%) | LVDT strain (%) |
|---|---|---|---|---|---|
| 100 | C08 | 1.577 | 2.011 | 27.521 | 23.9724 |
| 60 | C09 | 1.578 | 1.8245 | 15.621 | 14.417 |
| 30 | C10 | 1.578 | 1.703 | 7.921 | 7.193 |

*Comparison of Constant Creep Rates with Minimum Creep Rates from the Literature*

Within the last five years, there has been research on creep behavior of Alloy 617. Roy et al 2009 [6] used cylindrical specimens with a 37.59 mm gage length, while our test sets 1 and 2 involved rectangular gage sections. They reported testing at initial stresses of 24, 59, and 83 MPa at 850°C, and 18, 46, and 64 MPa at 950°C. Possible deviations from Roy et al's creep rate may also be due to the influence of when load was applied, since their creep experiments involved applying load after heating to the test temperature. The literature does not state the rate of which the load was applied. However, their results can be compared with our test sets in Figure 2.1.2.12, since the stresses are within the same range.

The constant creep rates determined from our testing appears to be a little lower than the data presented by Roy et al [6], but fits reasonably well within the scatter bands for both temperatures.

The experiments of both test sets ruptured within a shorter time than those noted in the literature. For test set 1: specimen C02 had ruptured at 24.4% strain after 2.5 hours of heating to 950°C and an additional 63.7 hours with constant load. However, Roy et al reported reaching 1.0% strain after approximately after 1000 hours under 950°C and 18 MPa, and about 3.7% strain after 200 hours at 950°C with 46 MPa. As for test set 2, specimen C08 ruptured at 23.97% strain after 3 hours heating to 850°C and an additional 161.2 hours of constant load. However, Roy et al reported reaching 1.5% strain after approximately 1100 hours at 850°C and 59 MPa, and about 10% strain after 200 hours at 850°C with an initial stress of 83 MPa. An explanation for why these differences are present is best left for the microstructural evaluation.
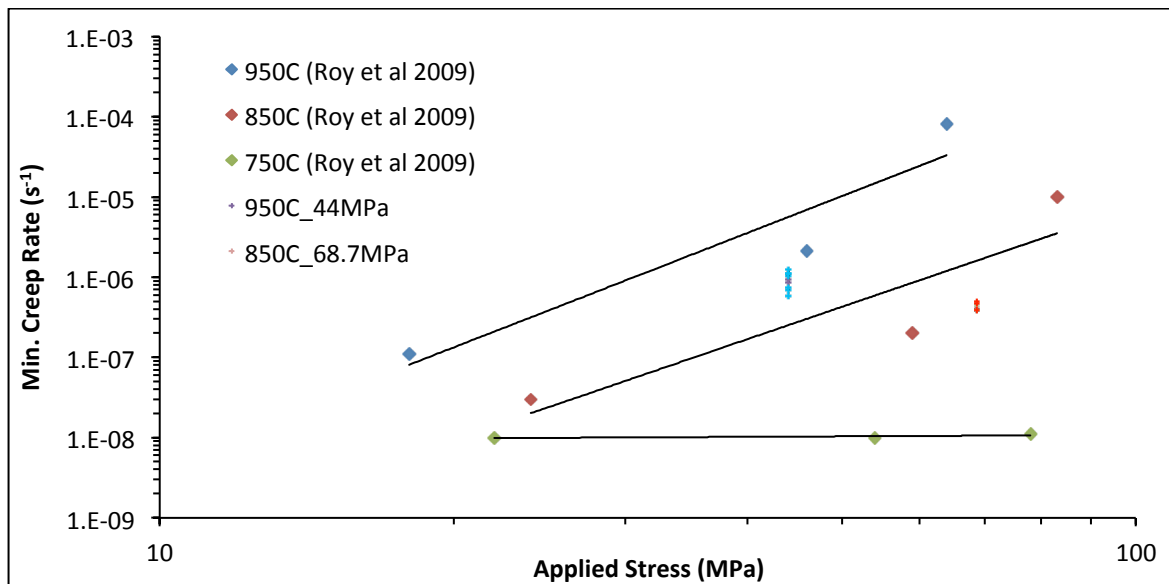
**Figure 2.1.2.12.** *Constant creep rates compared with results from Roy et al 2009 [6]. All tests were conducted in an air environment.*

*Closure*

Alloy 617 specimens were crept until rupture with the test temperature at approximately 850°C at an initial stress of 69 MPa, and at 950°C with initial stress as 44 MPa. Additional experiments were conducted for each temperature and stress, and then interrupted at 30% and 60% of the rupture strain. For 950°C, an additional test was conducted to 74% of the rupture strain. These samples will be tested using nonlinear acoustics to investigate second harmonic generation and then characterized by optical microscopy to determine the correlation between features of the second harmonic and features of the microstructure as creep damage progresses.

*References*

[1] Inconel alloy 617, Publication Number SMC-029, Special Metals Corporation, 2005.

[2] Bhadeshia, H.K.D.H. Mechanisms and Models for Creep Deformation and Rupture. University of Cambridge, UK; Elsevier 2003.

[3] S. Chomette, J.M. Gentzbittel, and B. Viguier. Creep behaviour of as received, aged and cold worked Inconel 617 at 850°C and 950°C. *Journal of Nuclear Materials* 399 (2010) 266–274.

[4] L. Carroll, C. Cabet, R. Wright The Role of Environment on High Temperature Creep-Fatigue Behavior of Alloy 617, *ASME PVP 2010*, July 2010.

[5] Ceramic Thermocouple Insulators, Omega Engineering, Inc., April 2012.

<http://www.omega.com/pptst/ORX_INSULATORS.html>

[6] A. K. Roy et al.  Creep Deformation of Alloys 617 and 276 at 750-950°C. *Materials Science and Engineering* A 520 (2009) 184-188.

*2.1.3 Biaxial*

The results of the biaxial loading (axial-torsion) tests on tubular specimens are summarized in this section, while the full results and analysis are provided in Appendix A.

Materials play an important role in society and find uses in diverse areas like load bearing structures, semiconductors and biological applications. High-temperature nuclear power reactors are one of these applications that require novel materials for extreme environments. High-temperature nuclear reactors are predicted to provide higher efficiency and cleaner power for society.  Alloy 617 is a candidate material for components of high-temperature reactors, e.g., intermediate heat exchangers. Considerable time and effort must be spent in order to understand the viscoplastic behavior of the material before it can be put into use because the material behavior depends on temperature, loading rate, loading paths and other factors.

This report presents multiaxial experimental results for Alloy 617 specimens tested in axial-torsion. These results are intended to be used in the development of unified constitutive models so that nuclear components can be designed for longer operational lives. Multiaxial experiments were conducted on Alloy 617 tubular specimens for three loading paths (MR1, MR2, and MOP), with brief loading path details and features of interest listed in Table 2.1.3.1. In addition, the creep-fatigue damage and degradation within these tubular specimens can be investigated via nonlinear ultrasonics and compared with observed microstructure changes.

MR1 and MR2 tests simulated creep-fatigue-ratcheting behavior in Alloy 617. The MR1 experiment was controlled in steady axial stress ($\sigma_{xm}$=12 MPa) and cyclic shear strain ($\Delta\gamma_c$). The MR2 experiment was a bow-tie path controlled in cyclic axial stress with holds at maximum and minimum stress and cyclic shear strain ($\Delta\gamma_c$), such that the applied axial stress mean ($\sigma_{xm}$) and amplitude ($\sigma_a$) were equal to 12 MPa.

The MOP experiment has three parts, the first and third part are axial strain cycles ($\Delta\varepsilon_a$), while the second portion is cycling of axial ($\Delta\varepsilon_a$) and shear strain ($\Delta\gamma_c$) 90° out-of-phase. Features of interest from MOP responses include the cyclic hardening/softening behavior under the highest degree of loading proportionality and the influence of stress relaxation on nonproportional cyclic hardening/softening.

Each test conducted for the MR1, MR2, and MOP paths is listed in Table 2.1.3.2, where test number, shear strain amplitudes, strain rate, and temperature are included.

***Table 2.1.3.1.*** *Multiaxial experiments on Alloy 617.*

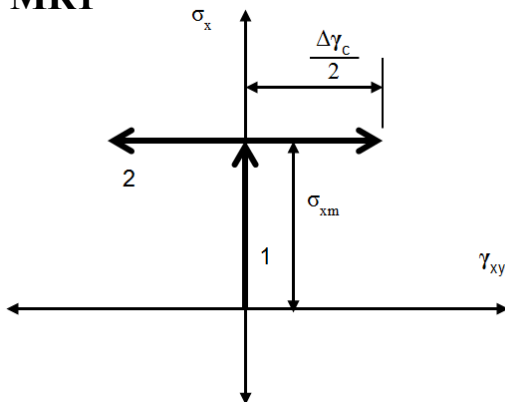| Loading Path | Experimental designation and features | Deliverables for the ASME-NH Code and UCM |
|---|---|---|
|  | **MR1:** Ratcheting-creep-fatigue under symmetric shear-strain cycle at steady axial stress.<br><br>Total 12 tests include 3 strain amplitudes, 4 temp levels, 2 strain rates and 5 repeats. | Multiaxial ratcheting-creep-fatigue life, ratcheting strain limits, mean-stress effect, stress-controlled shear hysteresis curves, and cyclic hardening-softening strain response under small degree of loading nonproportionality. |
|  | **MR2:** Multiaxial ratcheting-creep-fatigue under a bow-tie history mimicking structural stress history.<br><br>Total 10 tests include 2 strain amplitudes, 4 temp levels, 4 strain rates and 1 repeat. | Multiaxial ratcheting-creep-fatigue representing localized structural fatigue crack initiation; axial and shear stress-strain hysteresis curves and cyclic hardening-softening under intermediate degree of loading nonproportionality. |
|  | **MOP:** 100 axial strain cycles (I), followed by 100, 90° out-of-phase cycles (II), followed by 100 axial cycles (I).<br><br>Total 10 tests with 2 strain amplitudes, 2 temp levels, and 2 strain rates. | Cyclic hardening-softening under highest degree of loading nonproportionality; influence of stress relaxation on nonprop. cyclic hardening-softening; These experimental data are needed for the unified constit. model parameter identification. |
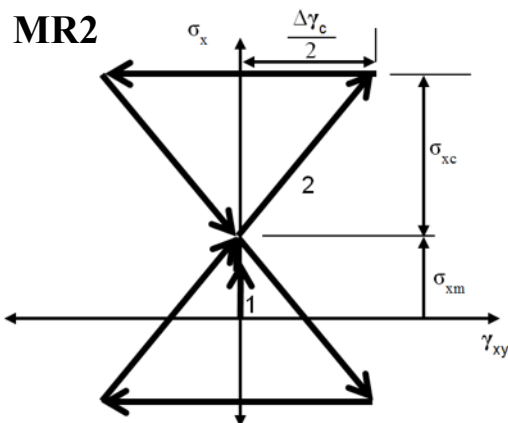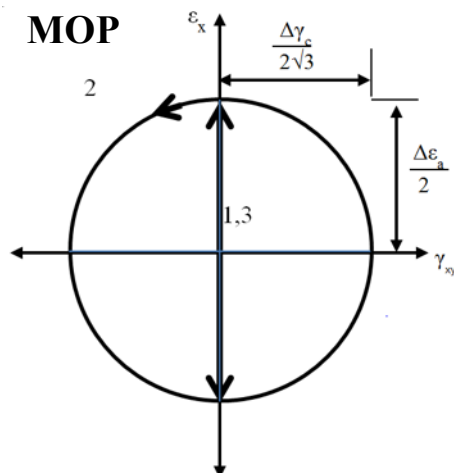
***Table 2.1.3.2:*** *Test matrix for MR1, MR2, and MOP tests with test numbers and corresponding shear strain amplitudes (Δγ$_c$/{2√3}) and rates (Δγ$_c$/{2√3s}).*

**MR1**

**± 0.002 rad**
- 950°C
  - 0.1%/s (Test 1)
    - Repeat
  - 0.04%/s (Test 2)
- 850°C
  - 0.1%/s (Test 3)
  - 0.04%/s (Test 4)
    - Repeat
- 650°C; 0.1%/s (Test 5)
- 25°C; 0.1%/s (Test 6)

**± 0.003 rad**
- 950°C; 0.1%/s (Test 7)
- 850°C; 0.1%/s (Test 8)

**± 0.004 rad**
- 950°C
  - 0.1%/s (Test 9)
  - 0.04%/s (Test 10)
- 850°C
  - 0.1%/s (Test 11)
    - Repeat
  - 0.04%/s (Test 12)

**MR2**

**± 0.0018 rad**
- 950°C
  - 0.1%/s (Test 13)
    - Repeat
  - 0.04%/s (Test 14)
- 850°C
  - 0.1%/s (Test 15)
  - 0.04%/s (Test 16)
- 650°C; 0.1%/s (Test 17)
- 25°C; 0.1%/s (Test 18)

**± 0.004 rad**
- 950°C
  - 0.2%/s (Test 19)
  - 0.08%/s (Test 20)
- 850°C
  - 0.2%/s (Test 21)
  - 0.08%/s (Test 22)

**MOP**

**± 0.002 rad**
- 950°C
  - 0.1%/s (Test 23)
  - 0.04%/s (Test 24)
- 850°C
  - 0.1%/s (Test 25)
  - 0.04%/s (Test 26)

**± 0.003 rad**
- 950°C
  - 0.1%/s (Test 27)
  - 0.04%/s (Test 28)
- 850°C
  - 0.1%/s (Test 29)
  - 0.04%/s (Test 30)
- 650°C; 0.1%/s (Test 31)
- 25C; 0.1%/s (Test 32)

**Interrupted**

Interrupted versions of test 12
- 850°C; 0.04%/s @ ± 0.004 rad
  - 90%
  - 70%

Shear strain amplitudes (Δ**γ**$_c$/2) were selected such that (Δ**γ**$_c$/(2/√3)) were equivalent to the values listed in Table 2.1.3.2.

The effect of temperature (950°C, 850°C, 650°C, and 25°C), shear strain rate (Δγ$_c$/{2√3s}= 0.1%/s, 0.04%/s), and shear strain amplitudes (Δγ$_c$/{2√3}= 0.0018, 0.002, 0.003, and 0.004 rad) on the mechanical behavior of the material has been investigated. While details on individual tests were presented within this research report, notable conclusions from MR1, MR2, and MOP tests are presented in the following.

For the figures presenting MR1 tests of the same amplitude or same shear strain rate, legends shown in Table 2.1.3.3 (a) and (b) were used respectively. The axial strain ratcheting behavior as a function of cycles were presented for MR1 shear strain amplitudes Δγ$_c$/(2√3) equal to 0.002 and 0.004 rad. The cycles to failure for higher shear strain amplitude MR1 tests (Δγ$_c$/(2√3) =0.004 rad) were 15-40% of the life for lower shear strain amplitude tests (Δγ$_c$/(2√3) =0.002 rad). Sudden changes in axial strain rates indicate the transition between the test interruption and restarting the loading path after reheating to the test temperature. Most of these tests showed nearly linear axial strain ratcheting rate, except for (1) 850°C_0.04%/s_0.002 rad. and (2) 850°C_0.10%/s_0.004 rad tests, where the gradual decreases in axial strain rate were more pronounced. Axial strains for test temperatures 25 and 650°C remained below

0.001 m/m after 10,000 cycles, since the temperatures were below the creep regime. The peak values for the cyclic shear stress response shown in Figure 2.1.3.2 correspond to the same tests in Figure 2.1.3.1. These plots demonstrate dominant cyclic softening in all cases but two.

**Table 2.1.3.3.** *Color schemes for figures that compare MR1 tests with either (a) same amplitude or (b) same rate (0.10%/s).*

| Constant Variables: | Same Amplitude | Same Rate (0.10%/s) |
|---|---|---|
| Color Legends | ■ 950°C, fast rate<br>■ 950°C, slow rate<br>■ 850°C, fast rate<br>■ 850°C, slow rate<br>■ 650°C, fast rate<br>■ 25°C, fast rate | ■ 950°C, 0.002 rad.<br>■ 950°C, 0.003 rad.<br>■ 950°C, 0.004 rad.<br>■ 850°C, 0.002 rad.<br>■ 850°C, 0.003 rad.<br>■ 850°C, 0.004 rad. |
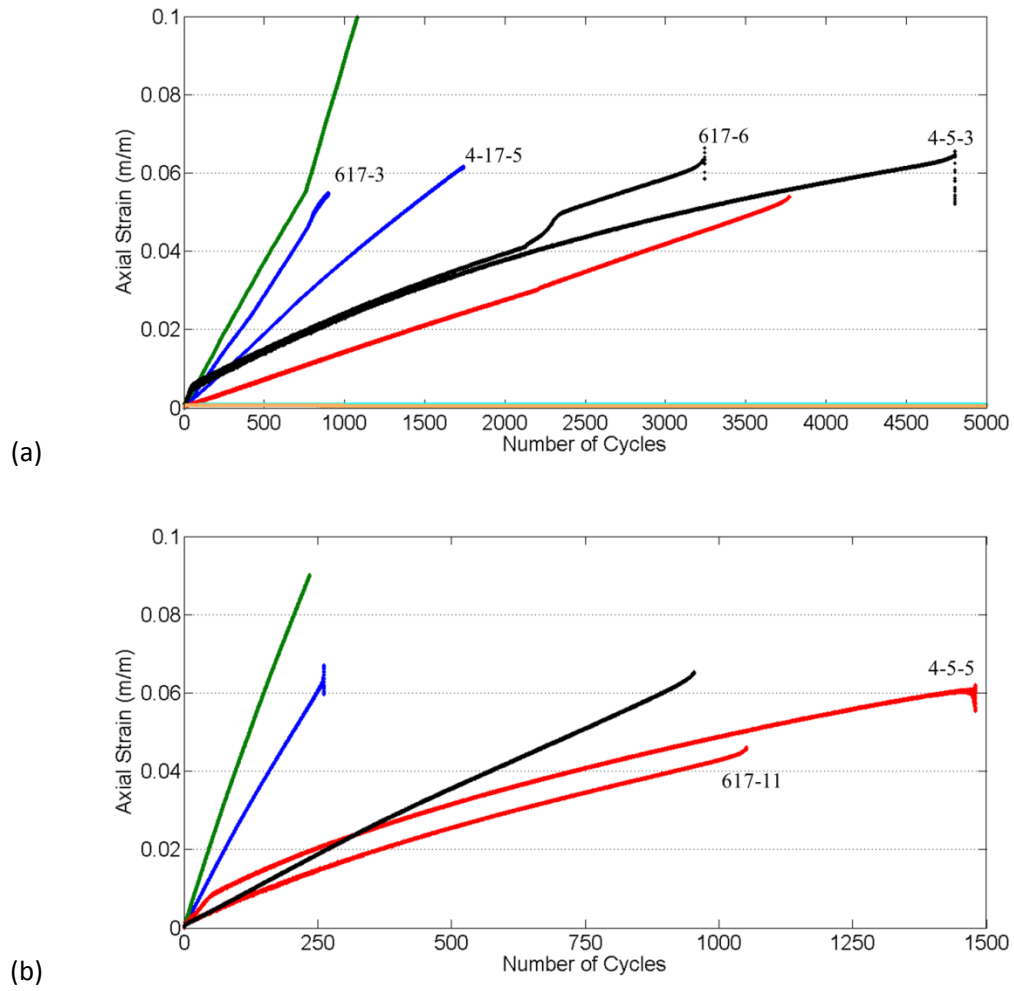
**Figure 2.1.3.1.** *Effect of shear strain amplitude Δɣ$_c$/(2√3); (a) 0.002 rad and (b) 0.004 rad on axial strain accumulation for MR1.*
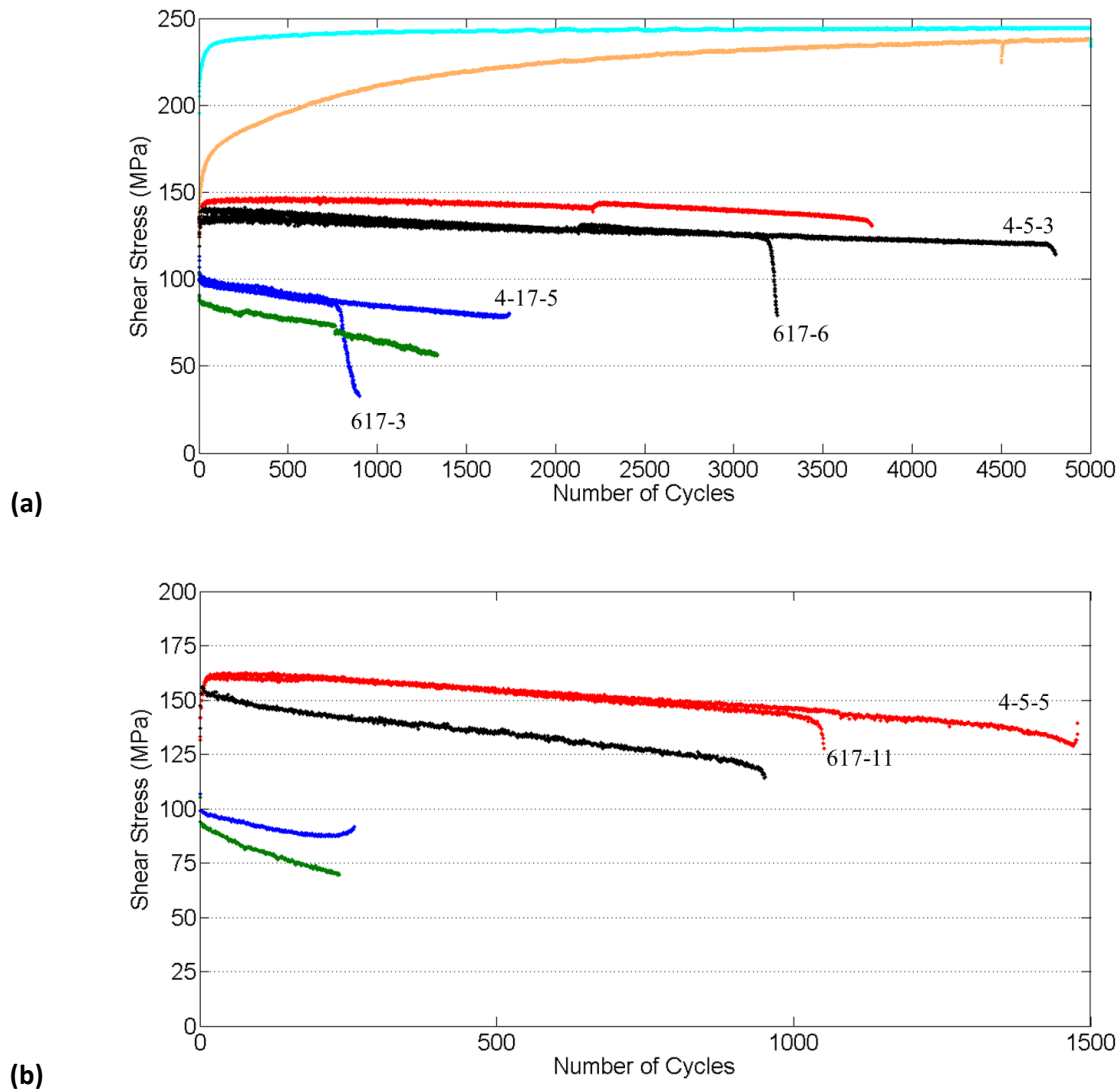
**Figure 2.1.3.2.** *Effect of shear strain amplitude Δɣ$_c$/(2√3); (a) 0.002 rad and (b) 0.004 rad on cyclic shear stress peaks for MR1.*

Regardless of amplitude, 850°C tests exhibited initial cyclic shear stress hardening within the first 20 cycles before proceeding with cyclic shear stress softening for the rest of the test. In contrast, the tests conducted at 950°C exhibited cyclic shear stress softening throughout the tests. Both 25 and 650°C tests exhibited initial cyclic shear stress hardening for longer durations than 850°C before eventually stabilizing. All MR1 tests conducted at 850°C and one 950°C test (specimen 617-3) exhibited a sudden drop in shear stress peak before fracture.

Figures 2.1.3.3 (a) and (b) are plots of axial strain and shear stress peak values versus number of cycles for MR1 tests with fast strain rate of Δɣ$_c$/(s2√3) 0.10%/s, using legend from Table 2.1.3.3 (b). These plots include results for two temperatures (950 and 850°C) and three strain amplitudes (Δɣ$_c$/(2√3)= 0.002,

0.003, and 0.004 rad). Higher strain amplitudes resulted in faster axial strain ratcheting rates for each test temperature. For each of these test amplitudes, tests conducted at 950°C resulted in faster ratcheting rates than at 850°C.  Most ratcheting rates were reasonably linear, except for when the strain amplitude $\Delta\gamma_c/(2\sqrt{3})$ was equal to 0.003 and 0.004 radian at test temperature 850°C. The cyclic shear stress softening rates were faster for higher strain amplitudes for 850°C tests. However, cyclic softening rates for 950°C tests with strain amplitudes $\Delta\gamma_c/(2\sqrt{3})$ equal to 0.002 and 0.003 rad. were similar, while the strain amplitude of 0.004 rad. displayed a slightly faster cyclic softening rate than the lower amplitudes.

Final cycle number ($c_f$) and averaged axial strain values are provided in Table 2.1.3.4 for MR1 tests.



(a)



(b)
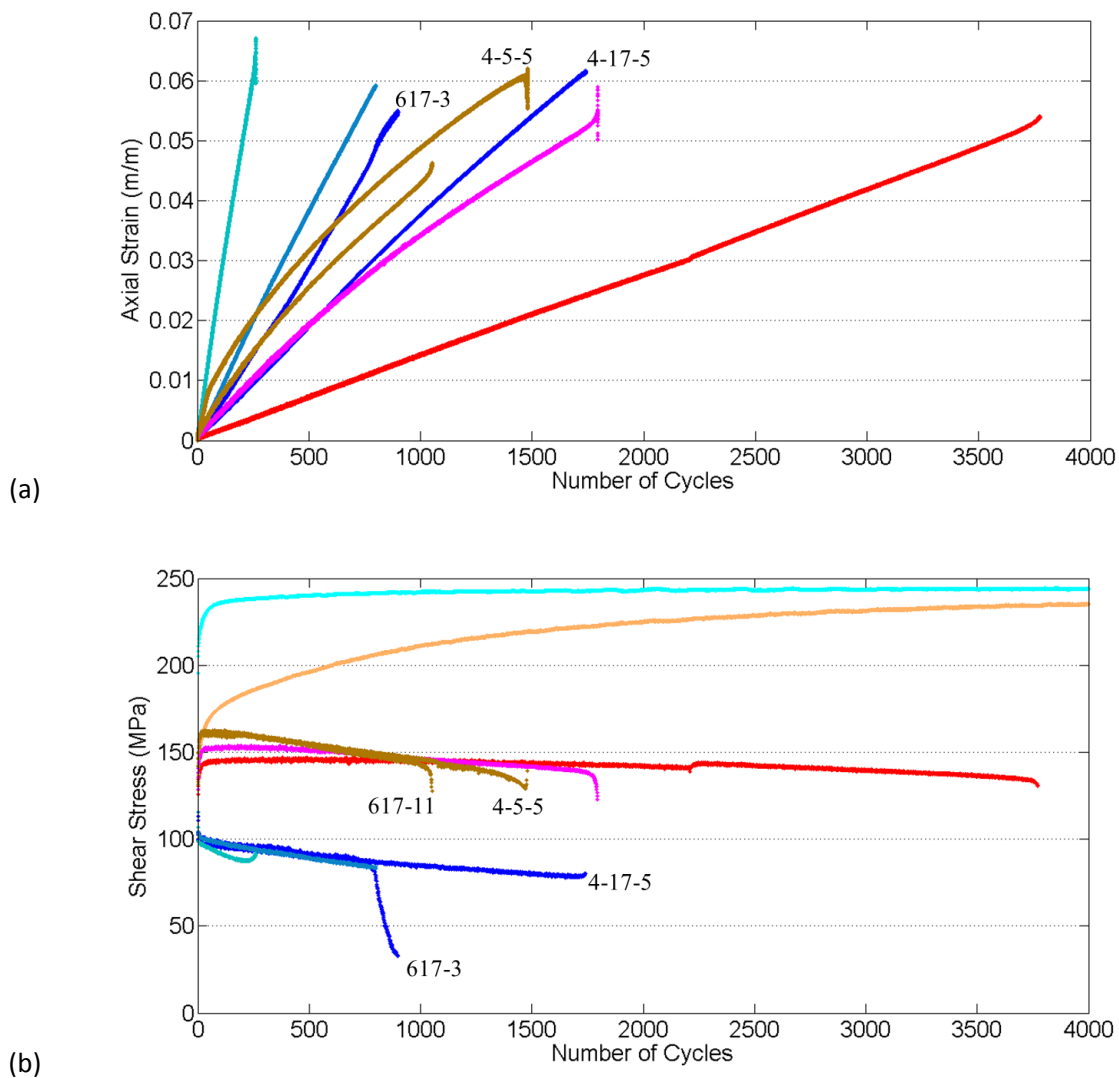
***Figure 2.1.3.3.*** *(a) Axial strain and (b) shear stress peaks for MR1 tests with fast loading rate of 0.10%/s. See Table 2.1.3.3 (b) for color legend.*

**Table 2.1.3.4.** *Final axial strain and cycles to failure for MR1 Tests.*

| Strain amplitude | Test Number | Temp and loading rate | Specimen | Final axial strain Average (mm/mm) | $c_f$ |
|---|---|---|---|---|---|
| 0.002 | 1 | 950°C fast | 617-3 | 0.05467 | 900 |
| | 1 repeat | 950°C fast | 4-17-5 | 0.06144 | 1740 |
| | 2 | 950°C slow | 617-5 | 0.1377 | 1302 |
| | 3 | 850°C fast | 617-4 | 0.05398 | 3770 |
| | 4 | 850°C slow | 617-6 | 0.06332 | 3230 |
| | 4 repeat | 850°C slow | 4-5 3 | 0.06447 | 4798 |
| | 5 | 650°C fast | 4-17-2 | 0.0004439 | 10010 |
| | 6 | 25°C fast | 4-17-3 | 0.0008785 | 10049 |
| 0.003 | 7 | 950°C fast | 4-5-2 | 0.05915 | 795 |
| | 8 | 850°C fast | 4-14-0 | 0.05456 | 1785 |
| 0.004 | 9 | 950°C fast | 617-12 | 0.06265 | 261 |
| | 10 | 950°C slow | 4-14-5 | 0.08991 | 230 |
| | 11 | 850°C fast | 4-5-5 | 0.06048 | 1478 |
| | 11 repeat | 850°C fast | 617-11 | 0.04584 | 1050 |
| | 12 | 850°C slow | 4-5-1 | 0.06507 | 950 |

$c_f$ corresponds to cycle number at failure or last cycle of test

Fast rate **Δγ$_c$/(2√3)/s=0.10%/s**; Slow Rate **Δγ$_c$/(2√3)/s=0.04%/s**

For the figures presenting MR2 tests of the same amplitude or same shear strain rate, legends shown in Table 2.1.3.5 (a) and (b) were used respectively.

*Table 2.1.3.5.* *Color schemes for figures that compare MR2 tests with either (a) same amplitude or (b) same temperature.*

| Constant Variables: | (a) Same Amplitude | (b) Same Temperature |
|---|---|---|
| Color Legends | ■ 950°C, fast rate<br>■ 950°C, slow rate<br>■ 850°C, fast rate<br>■ 850°C, slow rate<br>■ 650°C, fast rate<br>■ 25°C,  fast rate | ■ 0.0018 rad.; 0.10%/s<br>■ 0.0018 rad.; 0.04%/s<br>■ 0.0040 rad.; 0.20%/s<br>■ 0.0040 rad.; 0.08%/s |

Similar with MR1 tests, the slow rate 950°C tests resulted in higher axial strain ratcheting per cycle than the fast rate tests, since a longer cycle period allowed for more damage accumulation as shown in Figure 2.1.3.4. While most ratcheting rates were nearly linear, the 850°C_0.0018 rad._0.04%/s and 850°C_0.004 rad._0.20%/s exhibited a gradually decreasing ratcheting rate. The higher strain amplitude ($\Delta\gamma_c/(2\sqrt{3})$=0.004 rad.) and doubled strain rates resulted in shorter cycle lives than the lower strain amplitude tests ($\Delta\gamma_c/(2\sqrt{3})$ =0.0018 rad). Also similar to MR1 tests, for test temperatures 25 and 650°C the axial strain remained below 0.001 m/m, since creep mechanisms were not significantly activated.
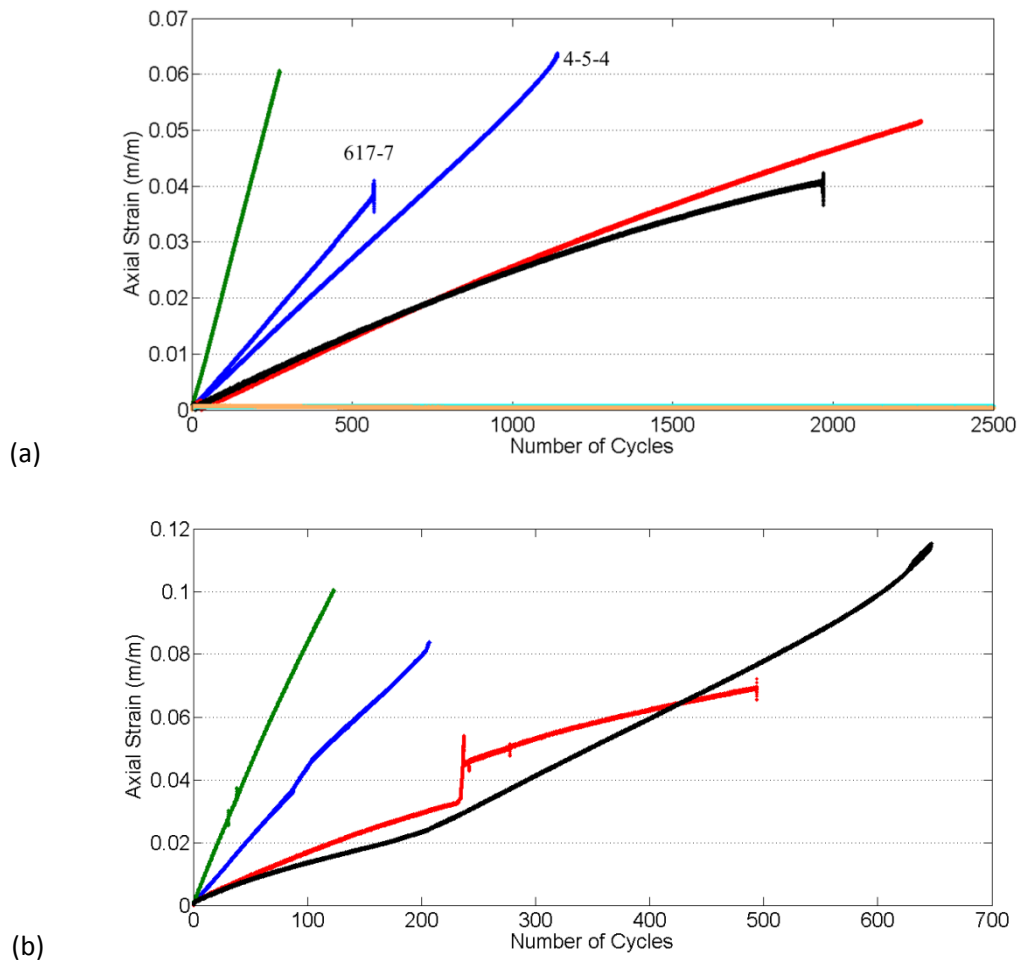
**Figure 2.1.3.4.** *Axial strain for MR2 tests, where shear strain amplitude Δɣ$_c$/(2√3) was equivalent to (a) 0.0018 rad and (b) 0.004 rad.*

Peak values of the cyclic shear stress response of these tests are shown in Figure 2.1.3.5. As with MR1 tests, higher applied shear stress is required for tests conducted at lower test temperatures to reach the same shear strain amplitude. In addition, lower shear stress results for slower strain rates (0.04%/s or 0.08%/s) than faster strain rates (0.1%/s or 0.20%/s) for tests with the same temperature. The cyclic shear stress softening rates were similar for tests of the same temperature and amplitude, except for when Δɣ$_c$/(2√3) was 0.004 rad at test temperature 850°C. At Δɣ$_c$/(2√3) equal to 0.004 rad, the cyclic softening rate was faster for the slow strain rate (0.08%/s) test than the fast strain rate (0.20%/s) test at 850°C. In addition, the general trends with the cyclic shear stress response were similar between MR1 and MR2 tests, where all tests except at 950°C began with initial cyclic hardening. MR2 tests conducted at 850°C, began with initial cyclic hardening and eventually exhibited cyclic softening after ~500 cycles. Tests conducted at 950°C exhibited cyclic softening only, while tests at 25 and 650°C showed significantly longer durations of cyclic hardening before stabilizing.

**(a)**



**(b)**
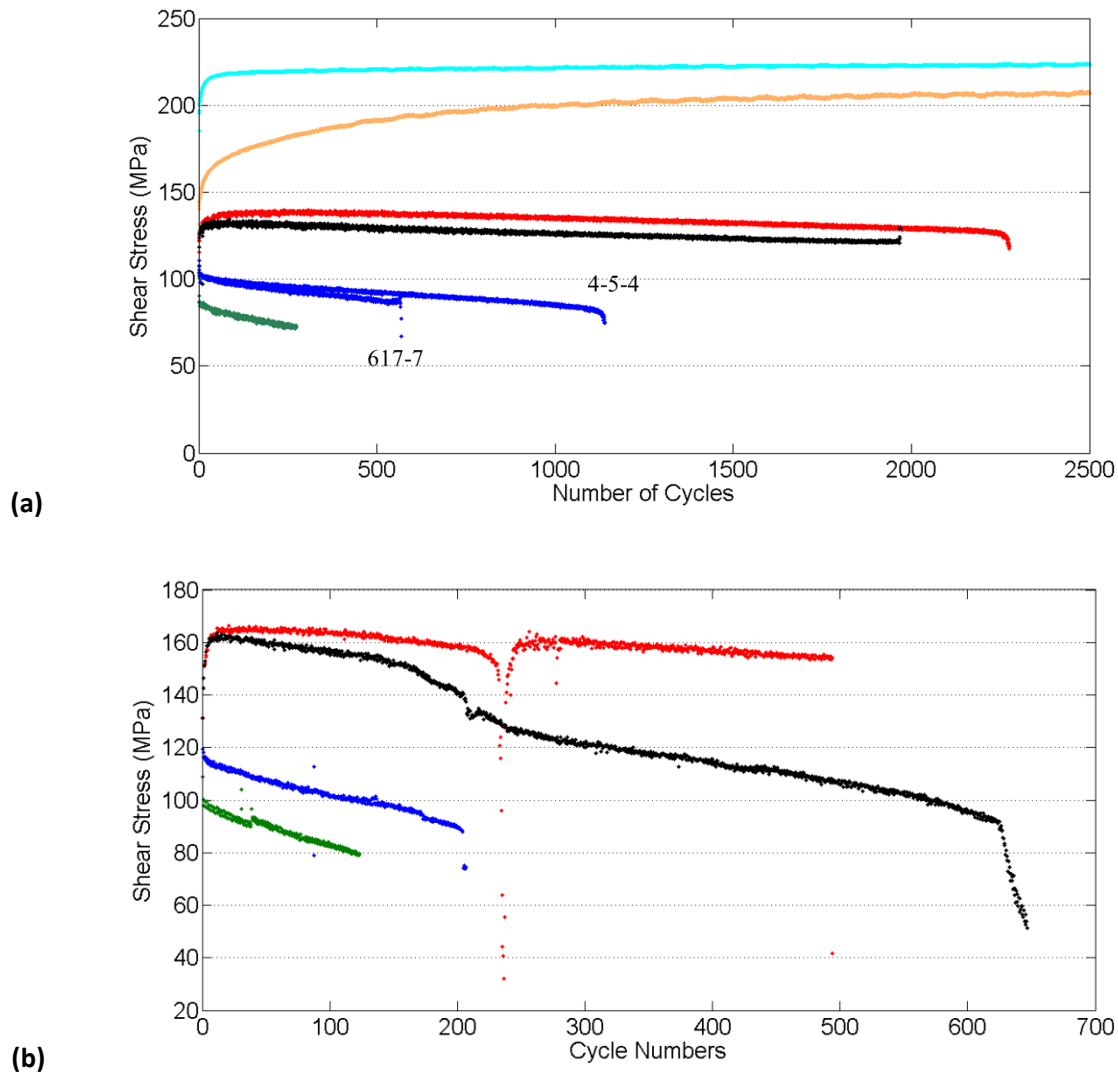
***Figure 2.1.3.5.*** *Peak values of cyclic shear stress for MR2 tests, where $\Delta\gamma_c/(2\sqrt{3})$ was equivalent to (a) 0.0018 rad and (b) 0.004 rad.*

The axial strain plots as a function of number of cycles are shown in Figures 2.1.3.6 (a) and (b), for MR1 tests conducted at 850 and 950°C respectively. For both temperatures, results for test strain strain amplitude $\Delta\gamma_c/(2\sqrt{3})$ equal to 0.0018 rad., shear strain rates $\Delta\gamma_c/(2\sqrt{3})/s$ of 0.04%/s and 0.10%/s were included. While strain amplitudes $\Delta\gamma_c/(2\sqrt{3})$ equal to 0.004 rad were shown with strain rates of 0.08%/s and 0.20%/s. For each test temperature (850 and 950°C) Figure 2.1.3.6 indicated that slow and fast shear strain rate tests for the same amplitude resulted in similar axial strain ratcheting trends for tests conducted at 850°C. However, 950°C resulted in more distinct axial strain rates from the different shear strain rates. For each shear strain amplitude, $\Delta\gamma_c/(2\sqrt{3})$ =0.0018 and 0.004 rad, the slower strain rate resulted in larger ratcheting per cycle. The peak values of the cyclic shear stress response for these MR2 tests for 850°C and 950°C are shown in Figures 2.1.3.7 (a) and (b) respectively. As expected, the higher strain amplitude $\Delta\gamma_c/(2\sqrt{3})$ of 0.004 rad resulted in faster cyclic shear stress softening than the lower strain amplitude of 0.0018 rad, which were also tested at half the strain rates of the higher strain

amplitude tests. Once again these figures show cyclic softening; only at 850°C is there initial cyclic hardening.



(a)

(b)
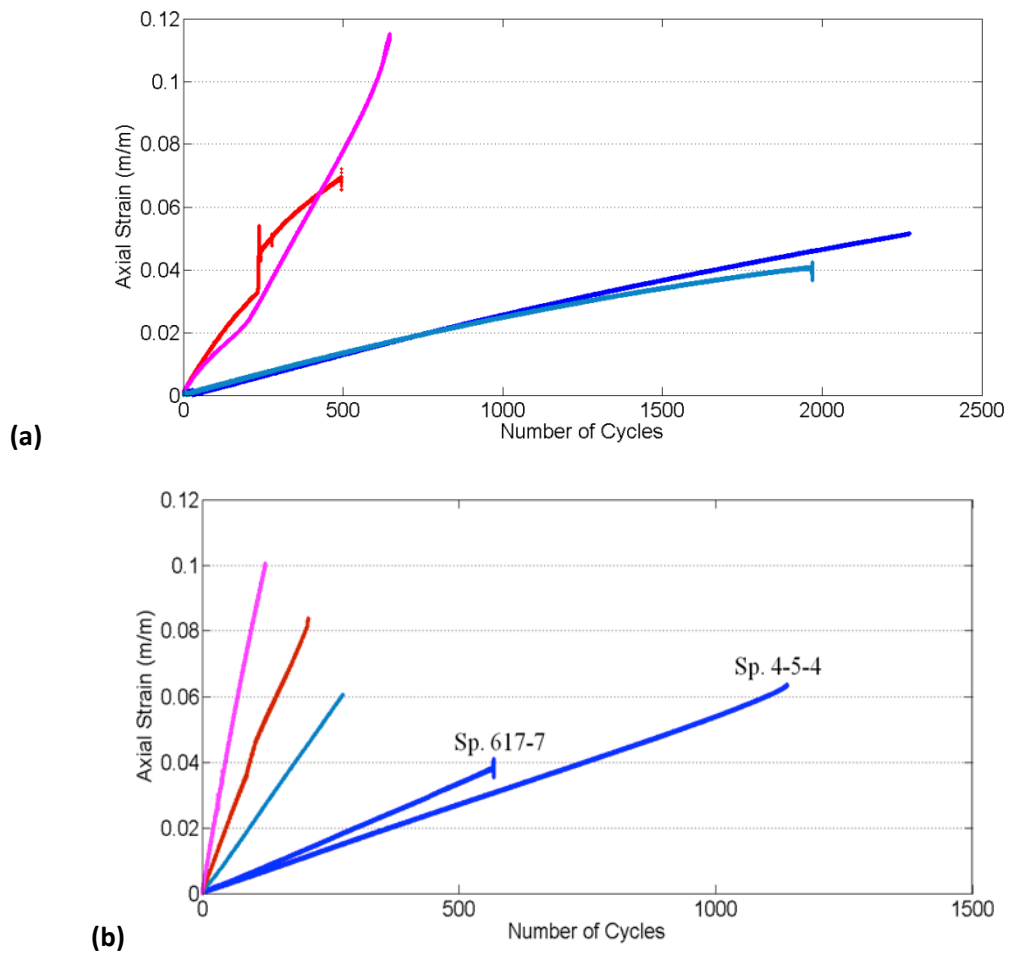
**Figure 2.1.3.6.** Axial strain for MR2 tests, (a) 850C and (b) 950C. See Table 2.1.3.5 (b) for color legend.
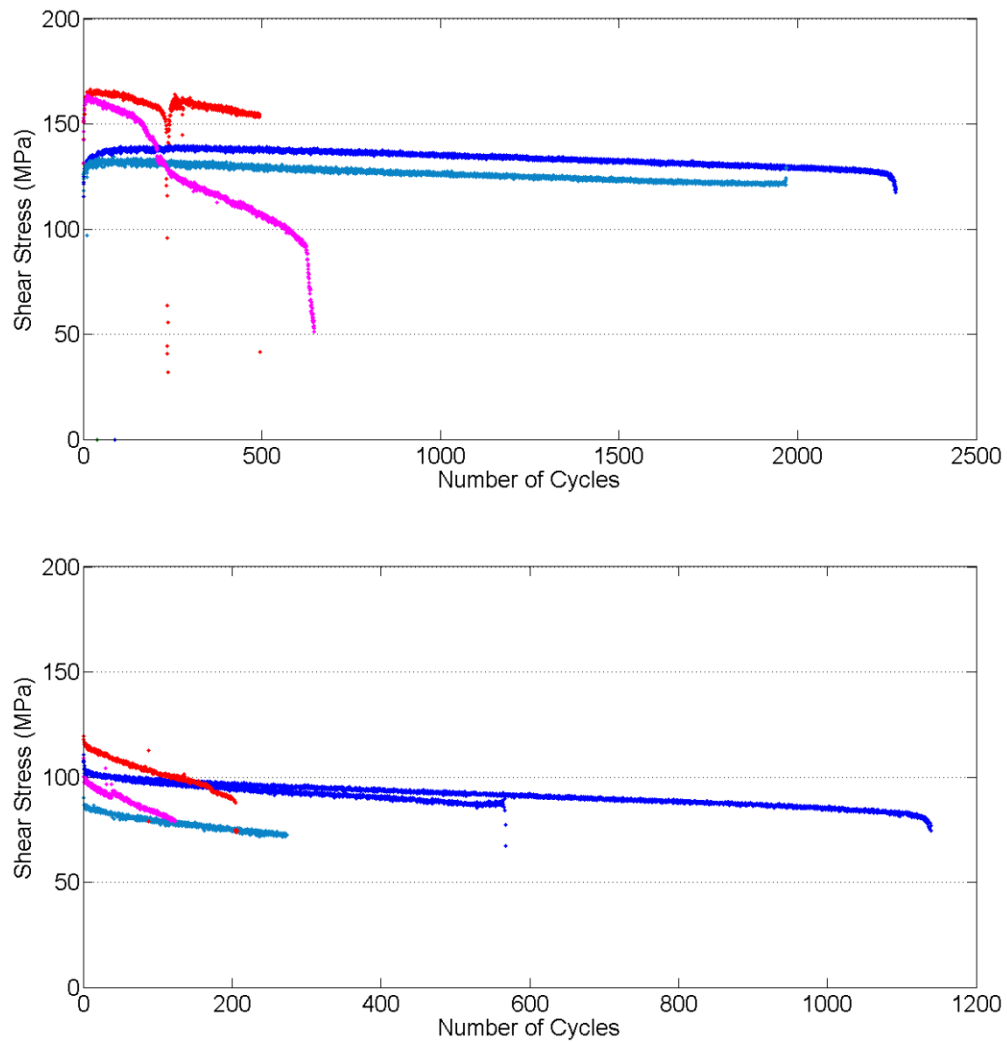
**Figure 2.1.3.7.** *Peak values of the cyclic shear stress for MR2 tests (a) 850C and (b) 950C. See Table 2.1.3.5 (b) for color legend.*

Table 2.1.3.6 contains final axial strain values averaged over the last cycle, and the number of cycles to failure for MR2 tests.

***Table 2.1.3.6.*** *Final axial strain and number of cycles to failure for MR2 Tests.*

| Strain amplitude ($\Delta\gamma_c/(2\sqrt{3})$) | Test Number | Temp and rate | Specimen | Final axial strain (mm/mm) | $c_f$ |
|---|---|---|---|---|---|
| 0.0018 rad. | 13 | 950°C fast | 617-7 | 0.03926 | 567 |
|  | 13 Repeat | 950°C fast | 4-5-4 | 0.06339 | 1138 |
|  | 14 | 950°C slow | 617-9 | 0.06055 | 273 |
|  | 15 | 850°C fast | 617-8 | 0.05153 | 2247 |
|  | 16 | 850°C slow | 617-10 | 0.04055 | 1964 |
|  | 17 | 650°C fast | 4-14-7 | 0.0002339 | 10025 |
|  | 18 | 25°C fast | 4-17-4 | 0.0007340 | 11274 |
| 0.0040 rad. | 19 | 950°C fast [Δ] | 4-11-7 | 0.08373 | 204 |
|  | 20 | 950°C slow [Δ] | 4-11-5 | 0.1003 | 122 |
|  | 21 | 850°C fast [Δ] | 4-11-4 | 0.06925 | 493 |
|  | 22 | 850°C slow [Δ] | 4-11-3 | 0.1144 | 632 |

[Δ] Fast and slow strain rates were 0.08%/s and 0.20%, which were double the rate of others

$C_f$ corresponds to cycle number at failure or last cycle of test

For figures comparing MOP test results of the same amplitude or same rate (0.10%/s) for segment (1), legends shown in Table 2.1.3.7 (a) and (b) were used respectively. The axial strain amplitude for all three segments of the MOP loading path was selected such that it was equivalent to the shear strain amplitude $\Delta\gamma_c/(2\sqrt{3})$ of segment (2) in radians.

For each MOP test, segment (1) and segment (3) involved 100 axial strain cycles, while segment (2) was the 90° out-of-phase loading of the axial and shear strain. Only the two slow rate tests (0.04%/s) with shear strain amplitude ($\Delta\gamma_c/(2\sqrt{3})$) equal to 0.002 rad, at 950 and 850°C were tested with 200 cycles for segment (2). Since the axial and shear stress trend for the latter 100 cycles of segment (2) exhibited a stabilized response, all other MOP tests were conducted with only 100 cycles for segment (2).

***Table 2.1.3.7.*** *Color schemes for figures that compare MOP tests with either (a) same amplitude or (b) fast rate (0.10%/s).*

| Constant Variables: | (a) Same Amplitude | (b) Fast Rate |
|---|---|---|
| Color Legends | ■ 950°C, fast rate<br>■ 950°C, slow rate<br>■ 850°C, fast rate<br>■ 850°C, slow rate<br>■ 650°C, fast rate<br>■ 25°C, fast rate | ■ 950°C, 0.003 rad.<br>■ 950°C, 0.002 rad.<br>■ 850°C, 0.003 rad.<br>■ 850°C, 0.002 rad.<br>■ 650°C, 0.003 rad.<br>■ 25°C, 0.003 rad. |

(a)



(b)



***Figure 2.1.3.8.*** *Peak values of (a) axial stress and (b) shear stress for MOP tests with shear strain amplitude Δγ_c/(2√3) of 0.002 rad [Tests 23-26]. See Table 2.1.3.7 (a) for color legend.*

The peak values for the cyclic response of the axial stress and shear stress are shown in Figures 2.1.3.8 (a) and (b), respectively. In these tests the shear strain amplitude $\Delta\gamma_c/(2\sqrt{3})$ was equal to 0.002 rad and similar results are shown in Figure 2.1.3.9 for a shear strain amplitude of 0.003 rad.



(a)



(b)
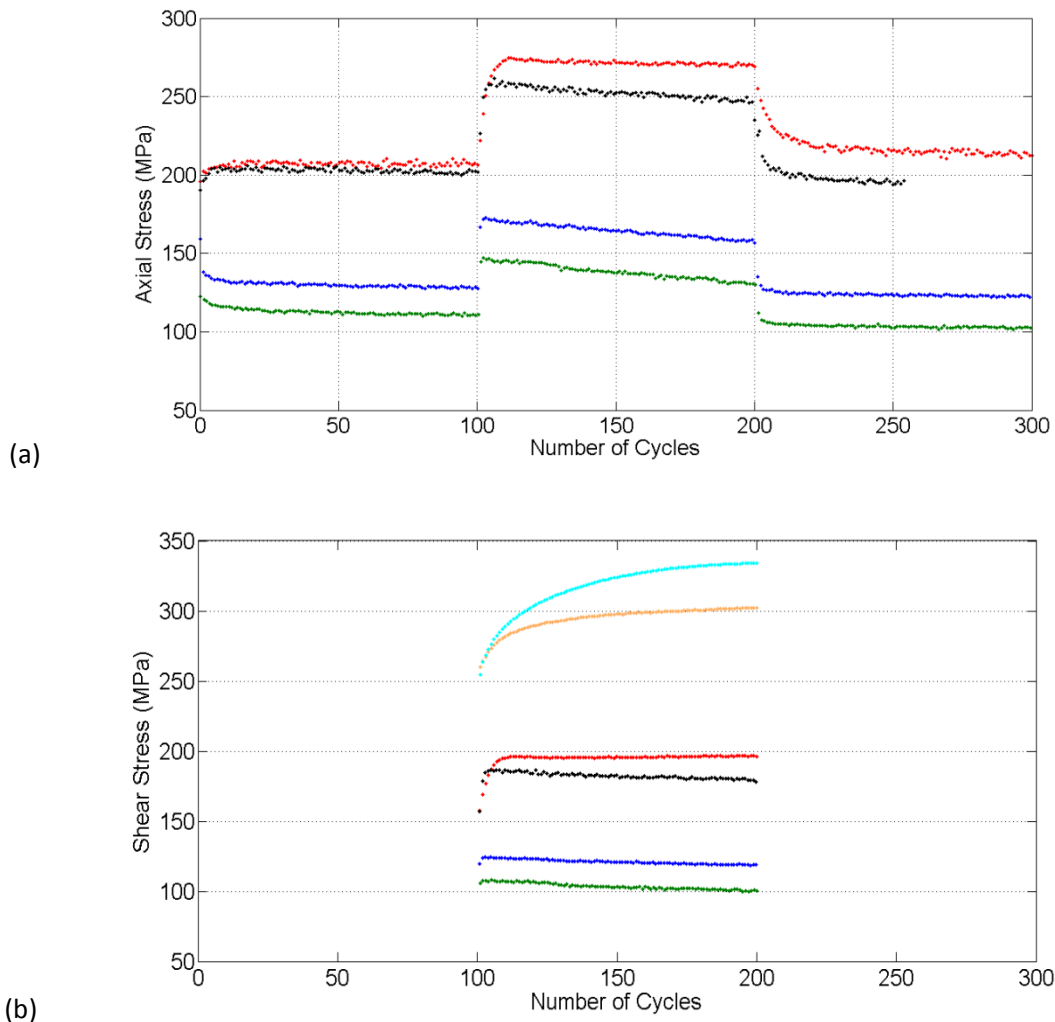
**Figure 2.1.3.9.** *Peak values of (a) axial stress and (b) shear stress for MOP tests with shear strain amplitude $\Delta\gamma_c/(2\sqrt{3})$ of 0.003 rad [Tests 27-32]. See Table 2.1.3.7 (a). for color legend.*

As observed with other tests, lower temperatures generally resulted in higher peak stress values. All four 850°C tests exhibited initial cyclic axial stress hardening for segment (1), while all four 950°C tests showed initial cyclic axial stress softening. While the cyclic axial stress values were generally stable/consistent for the rest of segment (1), both 950°C tests at higher strain amplitudes continued to exhibit slight cyclic axial stress softening. For both test amplitudes, the axial stress cyclic behavior exhibits the most significant changes within the first 20 cycles of each MOP loading path segment. All 950 and 850°C tests exhibited a sharp cyclic axial stress hardening immediately at the start of the 90°

out of phase loading of segment (2). After the initial cyclic axial stress hardening in segment (2), with one exception, all 850 and 950°C tests continued with some degree of cyclic softening.

In addition, for the 950°C MOP tests, the faster loading rate (0.10%/s) tests resulted in higher cyclic axial and shear stress peaks than the slower loading rate (0.04%/s). This also occurs at 850°C with $\Delta \gamma_c/(2\sqrt{3})$ equal to 0.003 radian, but the different rates resulted in similar axial stress peaks for the two tests at the same temperature when $\Delta \gamma_c/(2\sqrt{3})$ was equal to 0.002 rad.

Figure 2.1.3.10 provides similar data as Figures 2.1.3.8 and 2.1.3.9 except that only data from fast strain rate (0.10%/s) tests are shown. The two MOP tests that were conducted at 650°C and 25°C were the only tests to exhibit cyclic axial stress hardening for all three segments.



(a)



(b)
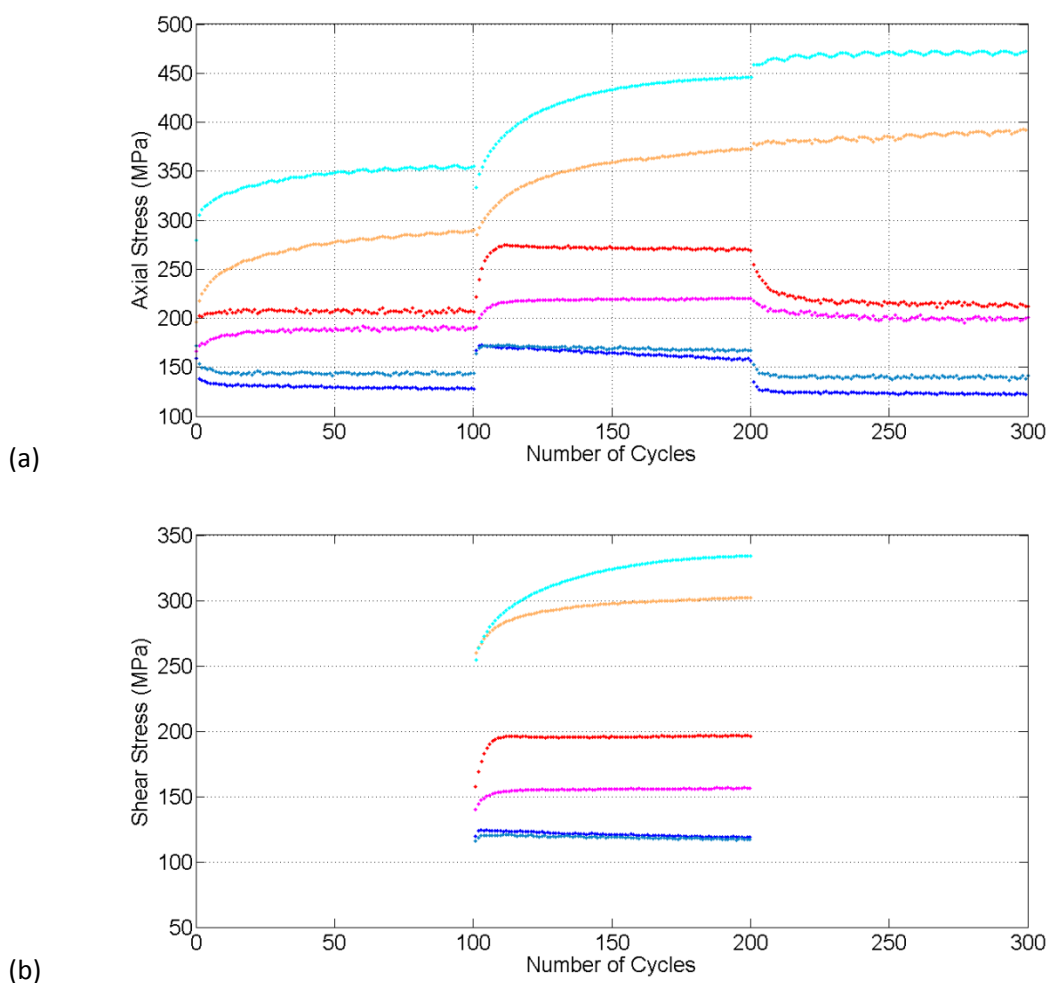
***Figure 2.1.3.10.*** *(a) Axial stress and (b) shear stress peaks for MOP tests with fast strain rate during Segments (1) and (3) [Tests 23, 25, 27, 29, 31, and 32]. See Table 2.1.3.7 (b) for color legend.*

These multiaxial experiments enable the characterization and validation of unified constitutive models so that nuclear components can be designed for longer operational lives with confidence. The results provide insight into loading path, temperature, amplitude, and rate effects on cyclic softening/hardening behavior and ratcheting of Alloy 617. In addition, the creep-fatigue degradation from these non-proportional loadings of tubular specimens can be investigated with nonlinear ultrasonics and compared with observed microstructure changes.

**2.2 Nonlinear Acoustics Methodology, Experimental Procedures, and Results**

Nonlinear acoustics, through the generation of higher harmonics, is well known to provide a nondestructive means to detect and possibly characterize microstructural changes. This section describes research into both bulk waves and guided waves for higher harmonic generation. The major contribution is the development of nonlinear ultrasonic guided waves for nondestructive characterization of microstructure evolution in hollow cylinders.

*2.2.1 Bulk Waves*

Bulk waves were employed to evaluate the effects of thermal aging, fatigue, and tensile creep on Alloy 617.

*2.2.1.1 Thermally Aged Samples*

The sample dimensions are 10, 13.5, and 38 mm in the x, y, and z directions. The samples were thermally aged in air at 950°C for times of 0, 312, 624, 936, and 1248 hours.

Figure 2.2.1.1 shows the qualitative results for Alloy 617 second harmonic generation versus the square of fundamental generation in X axis. By fitting the results in Figure 2.2.1.1, we got the qualitative nonlinear properties ($A_2/A_1^2$) for aged Alloy 617 samples in the X direction shown in Figure 2.2.1.2. The green line in the figure is the polynomial fit of all three measurements. Figure 2.2.1.3 shows the results for Alloy 617 second harmonic generation versus the square of fundamental generation in the Y direction. By fitting the results in Figure 2.2.1.4, we got the qualitative nonlinear properties ($A_2/A_1^2$) of aged alloy 617 samples in the Y direction shown in Figure 2.2.1.4. The green line in the figure is the polynomial fit of the two measurements. Figure 2.2.1.5 shows the results for Alloy 617 second harmonic generation versus the square of fundamental generation in the Z direction. By fitting the results in Figure 2.2.1.6, we got the qualitative nonlinear properties ($A_2/A_1^2$) of aged Alloy 617 samples in the Z direction shown in Figure 2.2.1.6. The green line in the figure is the polynomial fitting of all the two measurements. By comparing Figures 2.2.1.2, 2.2.1.4, and 2.2.1.6 we see that the polynomial fit lines in the X, Y, and Z directions are in good agreement.
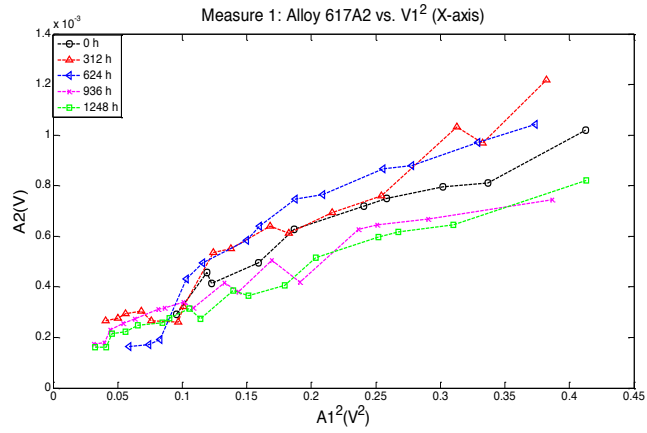
(a)
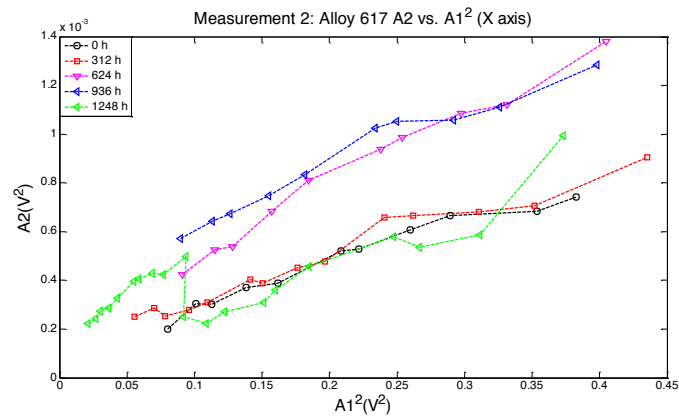


(b)
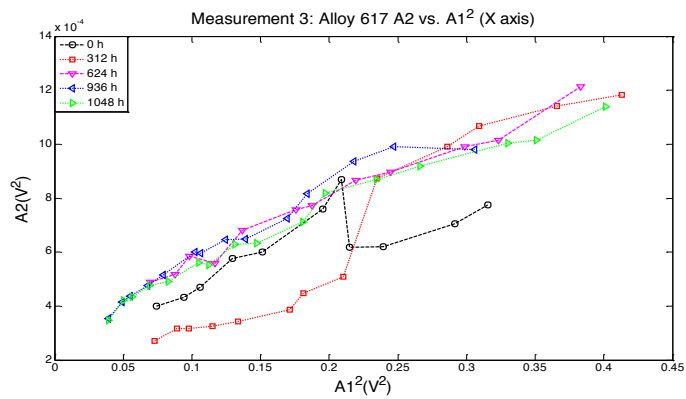


(c)

**Figure 2.2.1.1.** *Alloy 617 second harmonic as a function of the square of fundamental generation in X direction.*
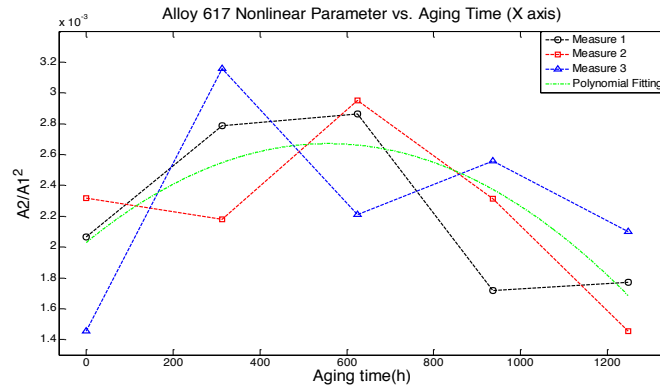
**Figure 2.2.1.2.** *Alloy 617 nonlinear parameter versus exposure time in X direction.*
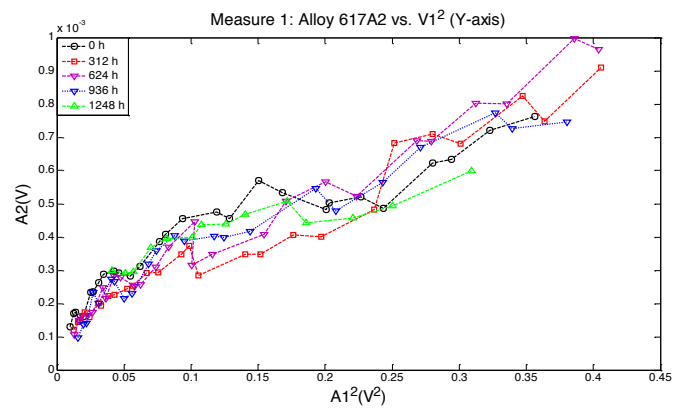


(a)
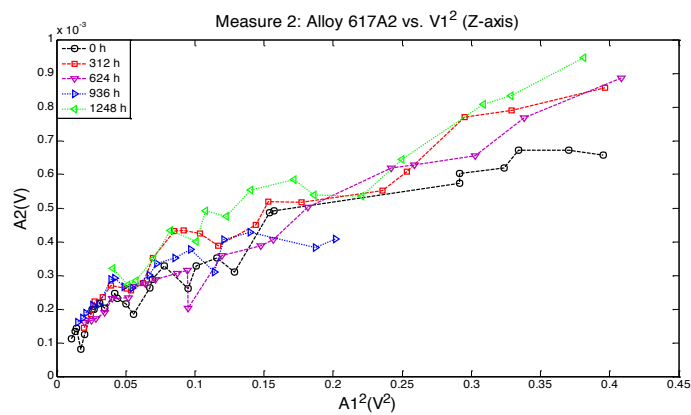


(b)

**Figure 2.2.1.3.** *Alloy 617 second harmonic as a function of the square of fundamental generation in Y direction.*

**Figure 2.2.1.4.** *Alloy 617 nonlinear parameter versus exposure time in Y direction.*
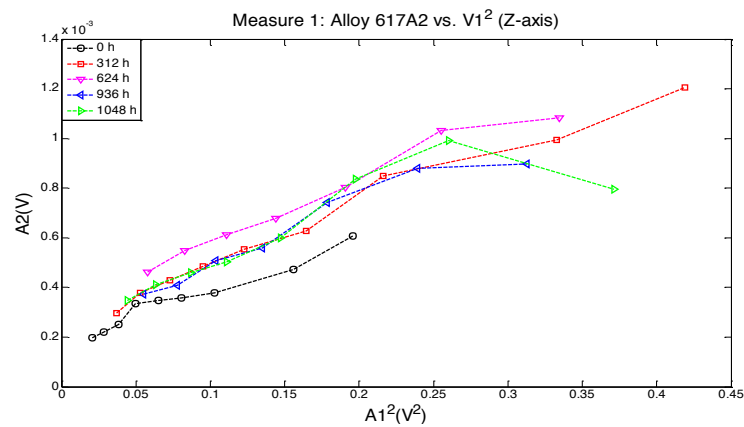


(a)
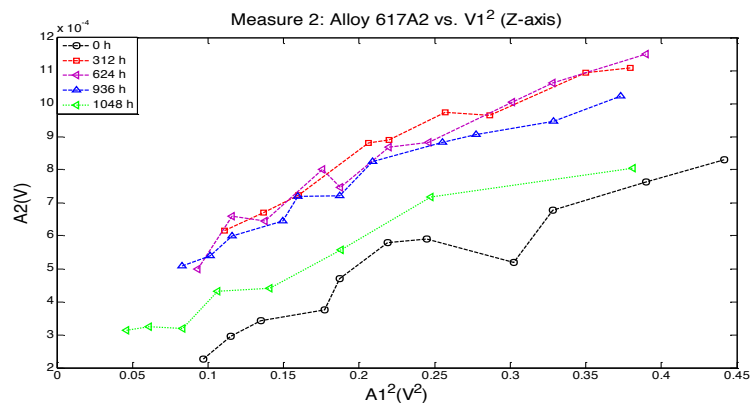


(b)

**Figure 2.2.1.5.** *Alloy 617 second harmonic as a function of the square of fundamental generation in Z direction.*
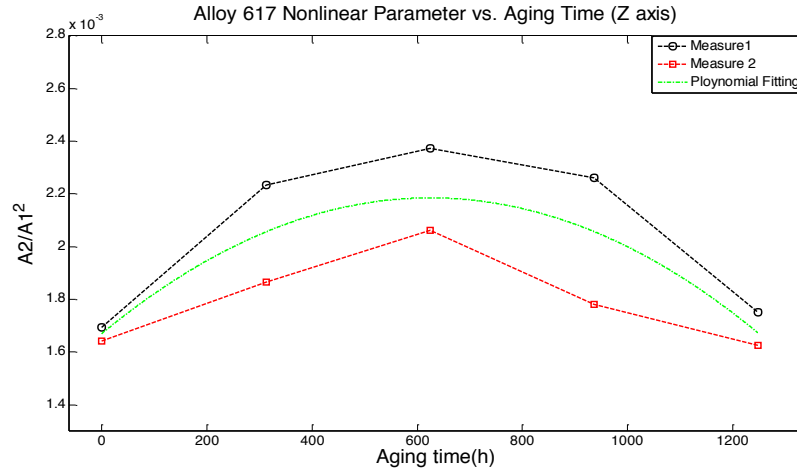
**Figure 2.2.1.6.** *Alloy 617 nonlinear parameter versus exposure time in Z direction.*

*Discussion of the Experimental Results*

One phenomenon often observed when alloys are exposed to elevated temperature involves the precipitation of secondary phases from a solid solution. Cantrell [1] pointed out that the presence of secondary phases alters the nonlinear properties of the material in a manner that depends on the volume fraction of secondary phases precipitated in the alloy material. Cantrell studied the effect of second-phase precipitates on nonlinearity generation and found that the material nonlinear parameter increases linearly with the volume fraction of precipitates $f_p$.

$$\beta \propto f_p \tag{1}$$

Yost et al. [2] gave the equation of nonlinearity generation by precipitate-dislocation monopole interaction to be:

$$\beta \propto \rho_{mp} L_0 |\delta| r_1^3 \tag{2}$$

where $L_0$ is the pinned dislocation segment length, $\delta$ is the precipitate matrix misfit parameter, $r_1$ is the diameter of precipitate.

The evolution of secondary phases in Alloy 617 due to aging at 950 °C is shown in Figure 2.2.1.7 from Chomette et al. [3]. After one hour aging treatment at 950 °C, few $M_{23}C_6$ precipitates are observed on slip lines. The number and size of these carbides do not seem to change up to 100 hours aging. After even longer exposure at 950°C, only a few $M_{23}C_6$ are still present in the grains.

45
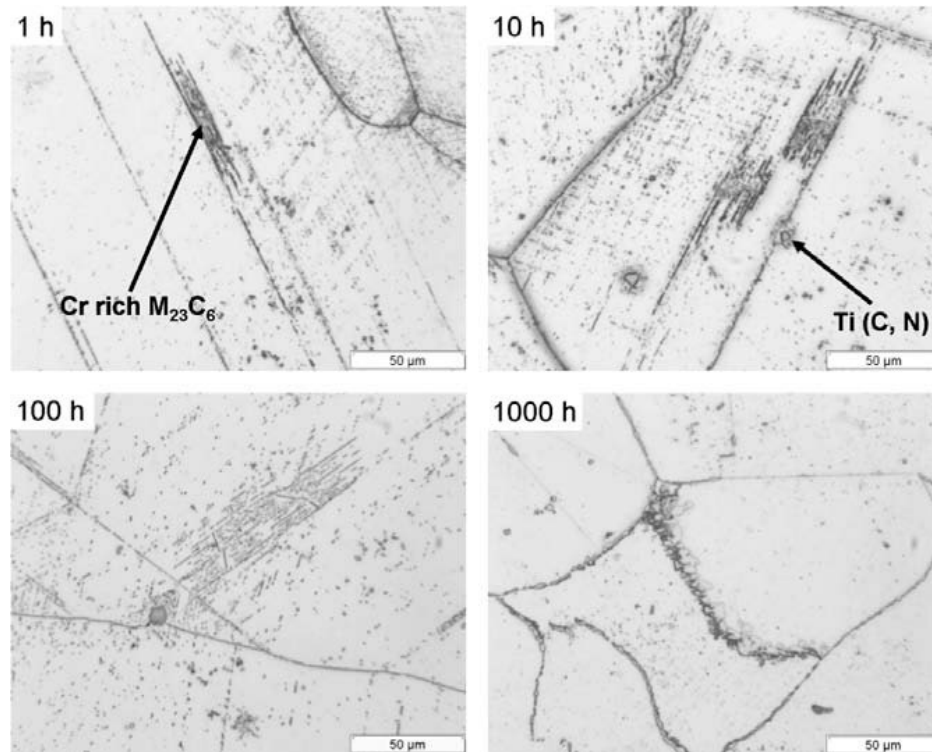
**Figure 2.2.1.7.** *Alloy 617 microstructure evolution for thermal aging taken by Chomette et al. [3].*

Our nonlinearity measurements are in good agreement with the microscopy observations of Chomette et al. [3] for precipitate evolution of alloy 617 at 950°C. This provides strong evidence that the nonlinear parameter can indicate second phase changes.

*Absolute Nonlinear Parameter Measurements*

To measure the absolute nonlinear parameter of alloy 617 samples, the fundamental and second harmonic displacements are needed. However, measuring the nonlinear parameter using contact transducers is not straight forward. A calibration procedure needs to be conducted for every single nonlinear measurement to convert voltage to displacement and also to account for couplant effects. Details about the calibration can be found in our progress report for Year 1 Quarter 4.

Figures 2.2.1.8 and 2.2.1.9 show the fundamental and second harmonic displacements when we use a 15 cycle toneburst. Figure 2.2.1.10 shows the nonlinear parameter for the aged Alloy 617 samples measured for all samples. The results are widely spread and inconsistent. So we decided to investigate the influence of different excitation cycles on harmonic generation. Up to 20 cycles were applied to the samples in an attempt to excite the narrowest frequency bandwidth. For 10 cycles the second harmonic generation is buried under noise. From Figures 2.2.1.11 and 2.2.1.12 we find that the second harmonic for 15 cycles is even larger than that of 20 cycles. A possible explanation is that there is spurious noise generation superimposed on the second harmonics for the 15 cycle measurement. This point could also account for the anomaly in the nonlinear parameter shown in Figure 2.2.1.10.
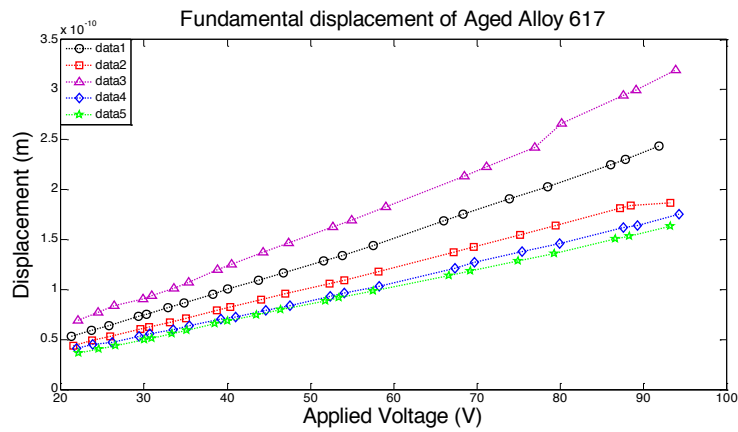
*Figure 2.2.1.8.* *Fundamental displacements of aged Alloy 617 samples (15 cycles).*
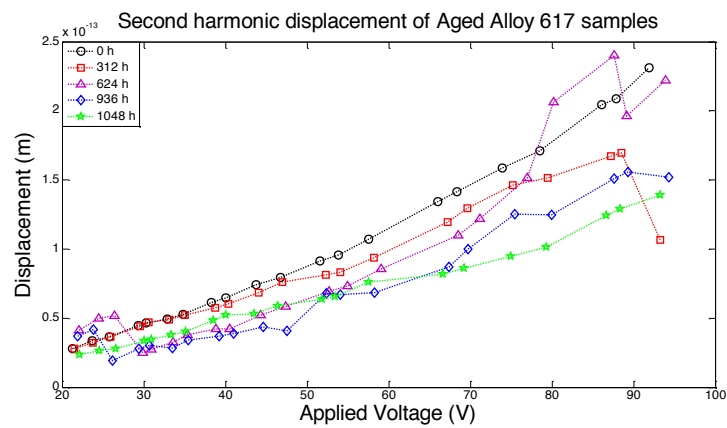


*Figure 2.2.1.9.* *Second harmonic displacements of aged Alloy 617 samples (15 cycles).*
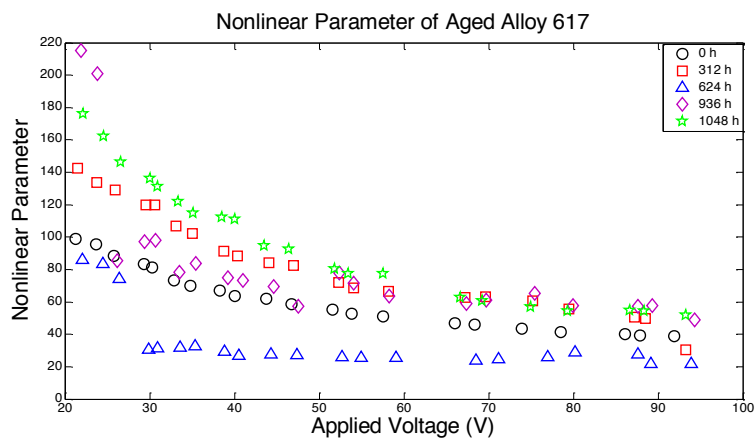


*Figure 2.2.1.10.* *Nonlinear parameter for aged Alloy 617 samples (15 cycles).*
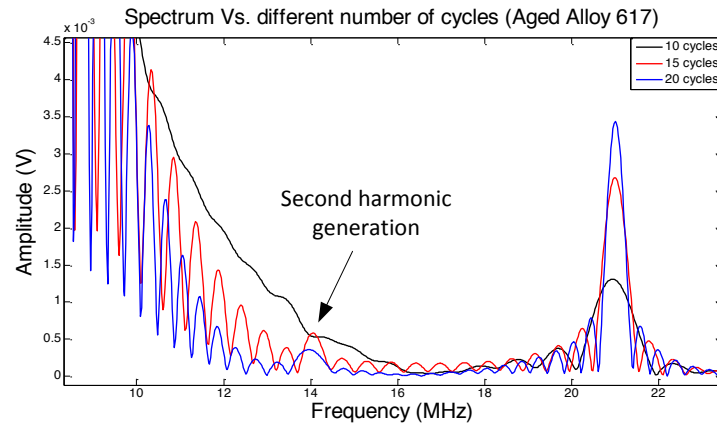
***Figure 2.2.1.11.*** *Harmonic generation for different number of cycles in the toneburst.*
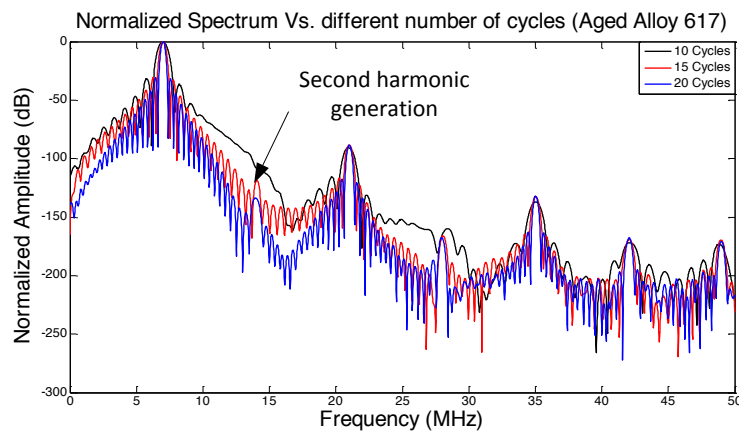


***Figure 2.2.1.12.*** *Normalized harmonic generation for different number of cycles in the toneburst.*

Figure 2.2.1.13 shows the nonlinear parameter for the aged alloy 617 samples measured by 20 cycles. The results roughly agree with the tendency of the qualitative nonlinear parameter ($A_2/A_1^2$) that we obtained in previous experiments. The result shows that the absolute nonlinear parameter of aged Alloy 617 corresponds well with the evolution of secondary phases.
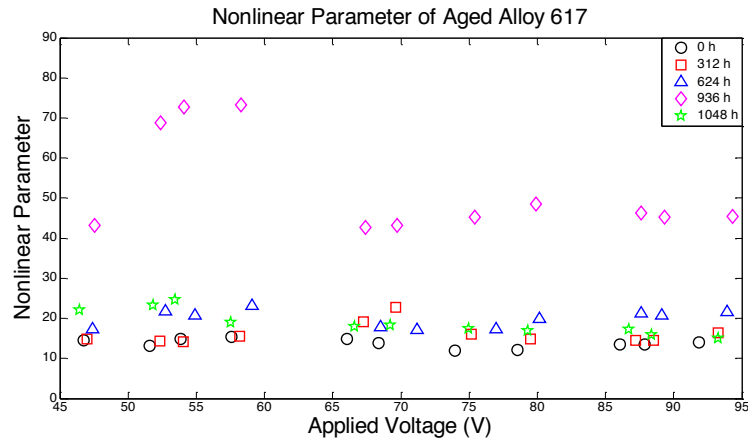
**Figure 2.2.1.13.** *Nonlinear parameter for aged Alloy 617 samples (20 cycles).*

*Measurements on Aged Alloy 617 Samples by Modified method*

    *Mathematical description of the measurement methods [4]*

For the 1-D problem of a longitudinal wave propagating from a source transducer (T1), couplant (C1), and then through a distance *L* as shown in Figure 2.2.1.14 we have:

$$A_1(L) = A_1(0) f_1(\alpha_1, L)$$

                                                      (3)

where $A_1(0)$ is the fundamental amplitude at the source and $f_1(\alpha_1, L)$ is a function of the attenuation coefficient $\alpha_1$ at the fundamental frequency and the propagation distance *L*. For longitudinal waves at a fixed distance from the source, the amplitude of the second harmonic is proportional to the square of the fundamental, and third harmonic is proportional to the cube of the fundamental:

$$A_n(L) = \beta_n (A_1(0))^n f_n(\alpha_1, \alpha_2 ... \alpha_n, L)$$

                                                      (4)

where $\beta_n$ is the nonlinear parameter and $f_n(\alpha_1, \alpha_2, ..., \alpha_n, L)$ is the factor that accounts for the attenuation at different harmonics.



**Figure 2.2.1.14.** *Schematic of nonlinearity measurement.*

49

The following notation will be used in the following derivation:

$D_i(w)-$ Amplitude of the input voltage to $T_i$ with respect to frequency

$G_i(w)-$ Response function of $T_i$ when it is used as a transmitter

$R_i(w)-$ Response function of $T_i$ when it is used as a receiver

$C_i(w)-$ Couplant response function at position i

$P_{ij}(w)-$ Function accounting for the attenuation of the signal received by $T_j$ at frequency $w$ when the input signal at $w$ is given by $T_i$

$P_{ij}(w_1,w_2)-$ Function accounting for the attenuation of the signal received by $T_j$ at frequency $w_j$ when the input signal at $w_j$ is given by $T_i$

$V_{[j](w_2)}^{[i](w_1)}-$ Amplitude of the signal received by transducer $T_j$ at frequency $w_j$ when the input signal at $w_i$ is given by transducer $T_i$

*Conventional Method*

In the conventional method, we transmit a signal at frequency $w_0$ by $T_1$ and measure the amplitude of the signal at frequency $w_0$ at $T_2$. Then the fundamental voltage amplitude can be obtained by:

$$V_{[2](w_0)}^{[1](w_0)} = [D_1(w_0)G_1(w_0)C_1(w_0)]P_{12}(w_0)C_2(w_0)R_2(w_0) \qquad (5)$$

The terms in the bracket can be identified as $A_1(0)$, and the attenuation term corresponds to $f_1(\alpha_1, L)$. The higher harmonic voltage amplitude is given by:

$$V_{[2](nw_0)}^{[1](w_0)} = \tilde{\beta}_n[D_1(w_0)G_1(w_0)C_1(w_0)]^n P_{12}(w_0,nw_0)C_2(nw_0)R_2(nw_0) \qquad (6)$$

where $\tilde{\beta}_n$ is the nonlinear parameter for second and third harmonic generation. Then we can derive the expression for the nonlinear parameter from the above equations:

$$\beta_n' = T_R \frac{C_2^n(w_0)}{C_2(nw_0)} \frac{V_{[2](nw_0)}^{[1](w_0)}}{(V_{[2](w_0)}^{[1](w_0)})^n} \qquad (7)$$

where

$$\beta'_n = \frac{\tilde{\beta}_n P_{12}(w_0, nw_0)}{P_{12}^n(w_0)}, \qquad T_R = \frac{R_2^n(w_0)}{R_2(nw_0)}$$

(8)

The following equation is often used to compute the conventional nonlinear parameter directly from the measurements:

$$\beta_n^{con} = \frac{V_{[2](nw_0)}^{[1](w_0)}}{(V_{[2](w_0)}^{[1](w_0)})^n}$$

(9)

where $n = 2,3$ represent the second and third harmonic generation.

### Modified Method

In the conventional measurement method, the measurement result is sensitive to coupling pressure, couplant layer thickness, and viscosity. Thus, couplant responses need to be calibrated. Here we give a new measurement method based on [4] to minimize coupling effect:

a)  transmit a signal at frequency $w_0$ from $T_1$ and measure the amplitude of the signal at frequency $w_0$ and $nw_0$ at $T_2$.

b)  Transmit a signal at frequency $nw_0$ from $T_1$ and measure the amplitude of the signal at $nw_0$ at $T_2$.

$$V_{[2](nw_0)}^{[1](nw_0)} = [D_1(nw_0)G_1(nw_0)C_1(nw_0)]P_{12}(nw_0)C_2(nw_0)R_2(nw_0)$$

(10)

c)  Transmit a signal at frequency $w_0$ from $T_2$ and measure the amplitude of the signal at $nw_0$ at $T_1$.

$$V_{[1](nw_0)}^{[2](w_0)} = \tilde{\beta}_n[D_2(w_0)G_2(w_0)C_2(w_0)]^n P_{21}(w_0, nw_0)C_1(nw_0)R_1(nw_0)$$

(11)

Combining Equations 3, 4, 9, and 10, we can calculate the modified nonlinear parameter by:

$$\beta'_n = T_{GR}[\frac{V_{[2](nw_0)}^{[1](w_0)}V_{[1](nw_0)}^{[2](w_0)}}{(V_{[2](w_0)}^{[1](w_0)})^n V_{[2](nw_0)}^{[1](nw_0)}}]^{\frac{1}{2}}[\frac{D_1(nw_0)}{D_2(w_0)}]^{\frac{1}{2}}$$

(12)

where

$$\beta'_n = \frac{\tilde{\beta}_n P_{12}(w_0, nw_0)}{P_{12}^n(w_0)P_{12}(nw_0)}, \qquad T_{GR} = \frac{R_2^n(w_0)G_1(nw_0)}{G_2^n(w_0)R_1(nw_0)}$$

(13)

We can now use the following equation to compute the modified nonlinear parameter:

$$\beta_n^{mod} = [\frac{V_{[2](nw_0)}^{[1](w_0)} V_{[1](nw_0)}^{[2](w_0)}}{(V_{[2](w_0)}^{[1](w_0)})^n V_{[2](nw_0)}^{[1](nw_0)}}]^{\frac{1}{2}} [\frac{D_1(nw_0)}{D_2(w_0)}]^{\frac{1}{2}}$$

(14)

where *n* = 2, 3 represent the second and third harmonic generation. This equation enables us to avoid the influence of the couplant.

*Experimental Results and Discussion*

Here we present nonlinear measurements on aged Alloy 617 samples from the modified method and also by conventional qualitative method. This enables a comparison of the two methods based on the experimental results. Figures 2.2.1.15 and 2.2.1.16 show the second harmonic generation plotted versus the square of the fundamental generation in the X direction by the conventional and modified methods, respectively. The slopes in Figures 2.2.1.15 and 2.2.1.16 give us the qualitative nonlinear parameter.
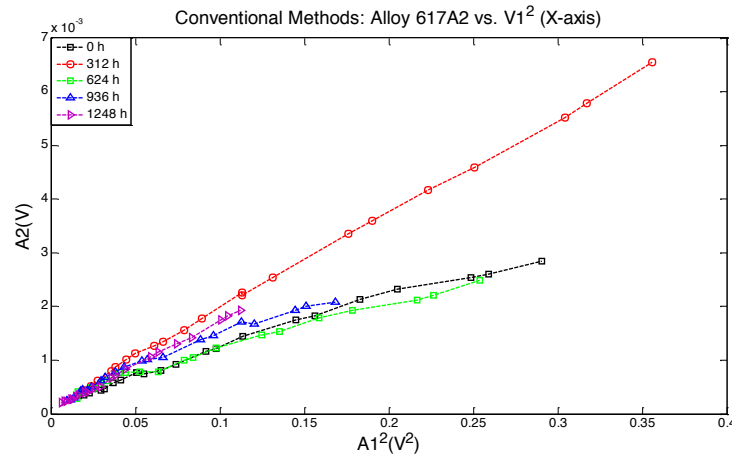


**Figure 2.2.1.15.** *Second harmonic generation versus the square of fundamental generation in X direction (by conventional method).*
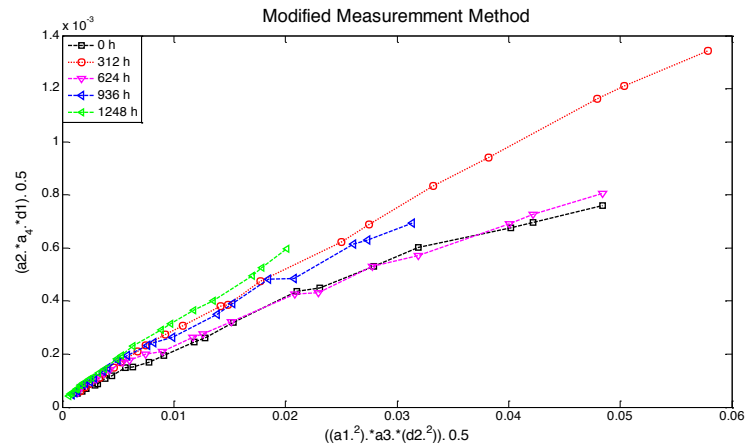
**Figure 2.2.1.16.** *Second harmonic generation versus the square of fundamental generation in X direction (by modified method).*

Figure 2.2.1.17 shows the qualitative nonlinear parameter of the aged samples by the conventional and modified methods. Experimental results from these two methods show good consistency. However, if we examine the standard error of the results for the two measurement methods shown in Table 2.2.1.2 we find that the standard error for the modified measurement method is much smaller than that from the conventional method. Which means the modified measurement can give us a more converged and accurate qualitative nonlinear parameter.



**Figure 2.2.1.17.** *Alloy 617 nonlinear parameter as a function of exposure time for X direction (comparison between conventional method and modified method).*

***Table 2.2.1.2.*** *Root mean squared error (standard error) for the measurements.*

|  | Control | #1 | #2 | #3 | #4 |
|---|---|---|---|---|---|
| Conventional | 6.0627*1e-5 | 4.9963*1e-5 | 5.2865*1e-5 | 4.9545*1e-5 | 6.4213*1e-5 |
| New Method | 2.6535*1e-5 | 1.5721*1e-5 | 1.6349*1e-5 | 1.6326*1e-5 | 0.80603*1e-5 |

*Summary Of Nonlinear Measurement on Aged Samples*

The research developed a reliable experimental procedure to monitor the microstructural evolution of in samples based on the acoustic nonlinear parameter. We demonstrated the effectiveness and reliability of this method by making repeatable measurements on thermally aged samples. The experimental results show that there is a good agreement between the nonlinear parameter and second phase evolution in Alloy 617 due to thermal exposure at 950°C.

*References*

[1] J.H. Cantrell, 2003, Fundamentals and Applications of Nonlinear Ultrasonic NDE, In: *Ultrasonic Nondestructive Evaluation: Engineering and Biological Material Characterization* (T. Kundu, Ed.), CRC Press, Boca Raton, FL, 2003.

[2] W.T. Yost, J.H. Cantrell, J. H., J.K. Na, 2001, "Nonlinear ultrasonic pulsed measurements and applications to metal processing and fatigue," In: *Review of Progress in Quantitative NDE*, 20, pp. 1268-1275.

[3] S. Chomette, J.M. Gentzbittel, B. Viguier. 2010, "Creep behavior of as received, aged and cold worked inconel 617 at 850 °C and 950 °C," *J. Nuclear Materials* 399, pp. 266-274.

[4] L. Sun, S. S. Kulkarni, J.D. Achenbach, and S. Krishnaswamy, 2006, "Technique to minimize couplant-effect in acoustic nonlinearity measurements," *J. Acoust. Soc. Am*. 120(5), pp. 2500-2505.

*2.2.1.2 Fatigue Samples*

The content in this section was adapted from X. Yao, Y. Liu, C.J. Lissenden, 2014, "Nonlinear acoustics experimental characterization of microstructure evolution in Inconel 617," In: *Review of Progress in Quantitative Nondestructive Evaluation*, Vol. 33, D.E. Chimenti, L.J. Bond, D.O. Thompson, Eds., American Institute of Physics Proc. 1581, pp. 733-738.

Six cylindrical Alloy 617 testing specimens with 7.5 *mm* in diameter are polished for both sides and cut in same length of 23.1 *mm*. These specimens undertook fatigue test under different temperature (850°C or 950°C), different strain rates and different cycles. After the tests, six specimens are classified into three groups by the severity of the surface damage, 'light', 'moderate' and  'heavy', each of which has two specimens in each category. Table 2.2.1.3 shows the test matrix of these specimens.

***Table 2.2.1.3.*** *Fatigue test matrix and categories.*

| Sample Number | Experiment Number | Δε (%) | T (°C) | $\dot{\varepsilon}$ (%/s) | Crack Initiation Cycle | Failure (25% Load Drop) |
|---|---|---|---|---|---|---|
| 'light' surface damage | | | | | | |
| N13846 | LCF-4 | 0.6 | 850 | 0.04 | 1369 | 1632 |
| N13858 | LCF-16 | 0.6 | 950 | 0.04 | 596 | 1054 |
| 'moderate' surface damage | | | | | | |
| N13853 | LCF-11 | 0.6 | 850 | 0.1 | 942 | 1280 |
| N13857 | LCF-15 | 0.6 | 950 | 0.1 | 535 | 904 |
| 'heavy' surface damage | | | | | | |
| N13860 | LCF-18 | 0.6 | 950 | 0.1 | 566 | 1048 |
| N13856 | LCF-14 | 0.6 | 950 | 0.1 | --- | --- |

The experiment chosen transmitter transducer is a 6.4 *mm* diameter, 5 *MHz* lithium niobate "disc transducer" fabricated by Boston Piezo-Optics. It was chosen to fit the small specimen in diameter. While a 10 *MHz* Ultran KC25-10 I40204 "commercial transducer" is used as receiver. This broadband commercial transducer is selected to receive both fundamental and second harmonic signal. Phenyl Salicylate (Salol) and traditional ultrasonic gel couplant are selected to be the couplant for the disc transducer and commercial transducer respectively. The special Salol couplant has its melting point at 41.5 °C, which can be easily melted by heat gun and will recrystallize in room temperature within several minutes. 40 cycles sinusoidal tone burst bulk wave is sent through the specimen by the transmitter transducer and distorted wave will be received by the receiver.  A special mounting fixture, shown in Figure 2.2.1.18, is designed to hold the specimen fixed in vertical direction. And a Teflon block is contoured to guide the soldered lead wires on the disc transducer, which is placed beneath the disc transducer. The commercial transducer is pressed down by constant pressure on the top of the specimen when bonding and testing.
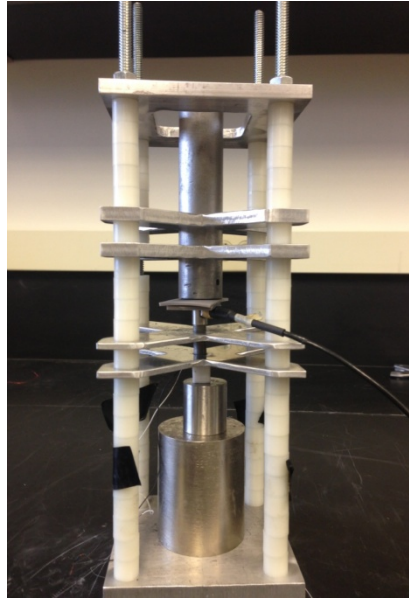
**Figure 2.2.1.18.** *Photograph of nonlinear acoustics experiment fixture.*

*Instrumentation*

Figure 2.2.1.19 shows a zoomed in picture of the specimen with two transducers attached. A tone burst signal of 40 cycles at 5 *MHz* is generated by a high-power gated amplifier (Ritec RAM-10000). The amplified high voltage signal, ranging from 110 *V* to 115 *V* passes through a diplexer to suppress the transient behavior due to the mismatch in electrical impedances between the amplifier and the transducer. Voltage signals of the receiving transducer are recorded and averaged 256 times with an oscilloscope, and then transferred to a computer for further signal processing.
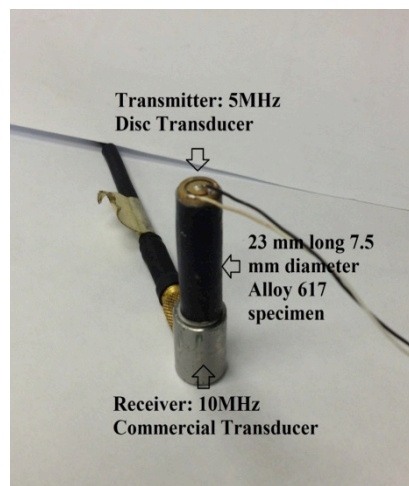


**Figure 2.2.1.19.** *Picture shows a zoomed in specimen (black cylinder) with disc transducer (gold one with two lead wires) on top and commercial transducer on the bottom.*

*Signal Processing*

Time domain signal acquired from the oscilloscope Figure 2.2.1.20 has a distinguishable first wave package, regarded as the mechanical signal from the transmitter after propagating through the specimen length direction. Material dislocations obviously distort the input pure sinusoidal signal. In order to maintain a consistent signal processing procedure, a uniform Tukey window of a constant length is used for all the signal processing procedures (shown as red square in Figure 2.2.1.20).
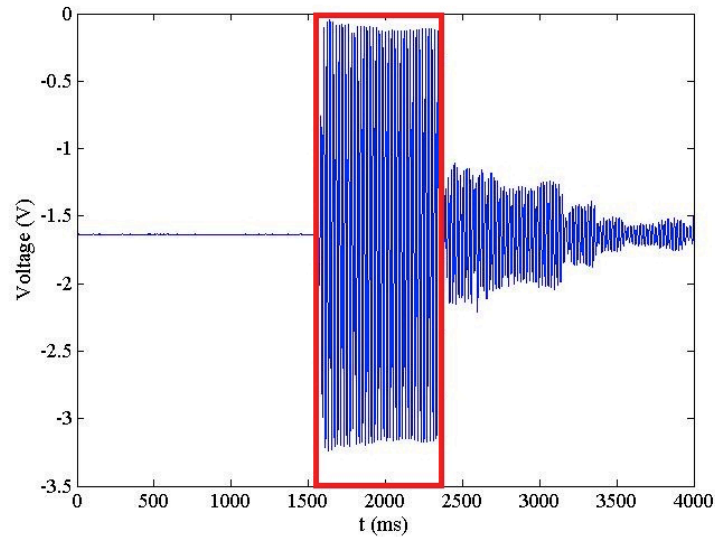


***Figure 2.2.1.20.*** *Time domain signal from oscilloscope with window for FFT denoted by red box.*

Figure 2.2.1.21 shows the frequency domain signal in log scale after normalization. The amplitude spike of fundamental frequency (5 *MHz*) and the second harmonic (10 *MHz*) can easily be distinguished above the noise. The amplitudes of fundamental frequency ($A_1$) and second harmonic ($A_2$) are the two parameters needed for the calculation of relative nonlinear parameter.
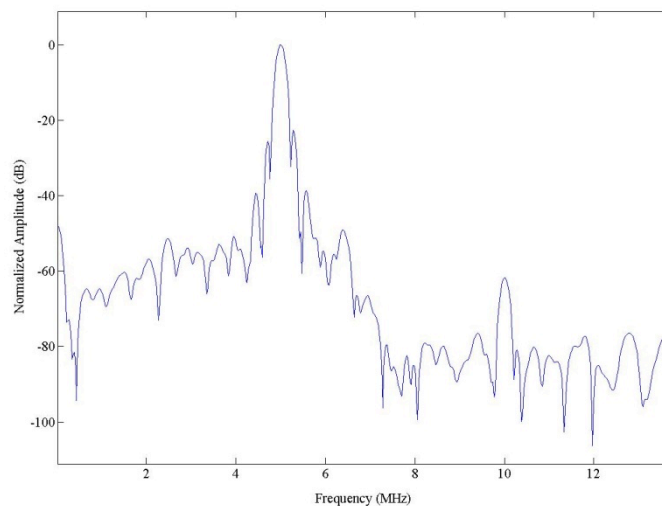
**Figure 2.2.1.21.** *Normalized frequency spectrum from FFT on a log scale.*

*Experimental Procedure*

1.  The disc transducer is bonded to the specimen by melting Salol with heat gun. It takes about 5 minutes to melt and then recrystallize.

2.  The specimen with the disc transducer in place is installed into the mounting fixture with the disc transducer placed onto the Teflon at the bottom.

3.  The commercial transducer is placed on top of the specimen with Ultra Gel couplant in between. A constant weight is used on top of the Ultra transducer to provide a stable experiment conditions for every single test.

4.  Heat the Salol with heat gun for a couple of seconds until it melts again and then recrystallization under the constant weight (for uniform bond thickness) takes about 15 minutes.

5.  A sinusoidal electronic tone burst signal of 5 MHz, 40 cycles is provided by RITEC RAM 10000 to the disc transducer with only the amplitude of the output signal being variable.

6.  Time domain signals from the receiving commercial transducer for 6 different voltages are saved from the oscilloscope.

7.  Specimen is taken out of the mounting fixture. Both transducers are removed from the specimen.

8.  Repeat steps 1 to 7 three times for one specimen to demonstrate repeatability.

*Results and Discussion*

The experiment results demonstrate a reliable consistency not only within every single test when varying only the voltages, but also show great repeatability for 3 individual tests, where couplant and transducers are removed and reinstalled for every single test. Figure 2.2.1.22 shows relative nonlinear parameter results for six specimens with different stage of damage. Generally, the monotonic increasing tendency of relative nonlinear parameter can be clearly observed. The high up relative nonlinear

parameter value for specimen N13846 can be explained by abnormal microstructure dislocation inside the material due to its greater cycles leading to failure (Table 2.2.1.3), which may not be detected or distinguished by surface damage.
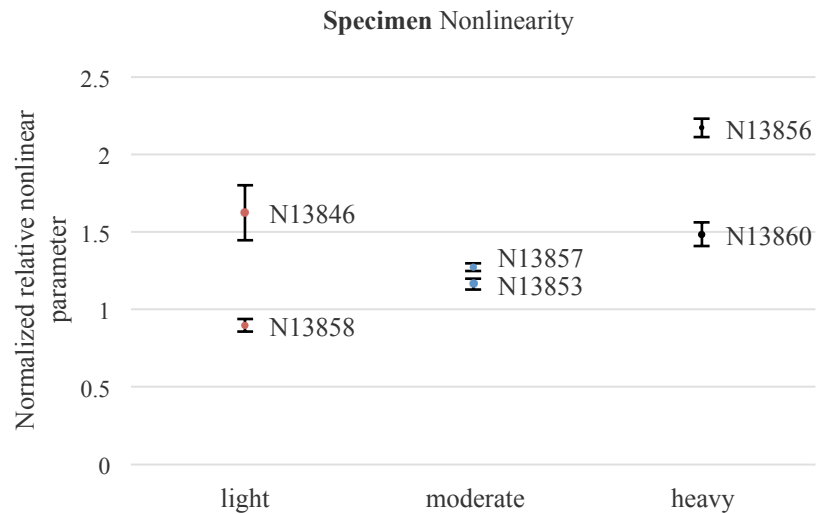


**Figure 2.2.1.22.**  *Normalized relative nonlinear parameter results for six different fatigued specimens, which sustained surface damage deemed to be: light (N13846, N13858), moderate (N13857, N13853), heavy (N13856, N13860). Error bars illustrate the standard deviation for three individual tests.*

When comparing the nonlinear acoustics results to the stereoscope images shown in Figure 2.2.1.23, we see that the nonlinearity parameter grows with surface damage severity, which agrees with the theoretical predictions that larger microstructural defects result in greater material nonlinearity. While some of the 'heavy' surface damage do not seem to be severe enough in the picture, but they really are worse compared to others when we have them in hand.
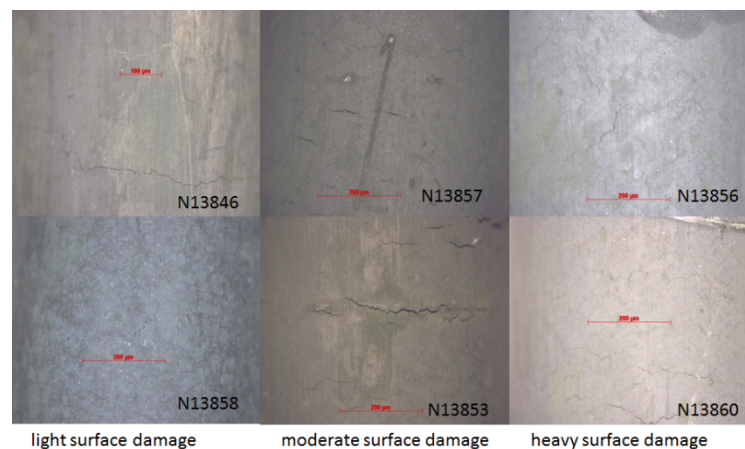


**Figure 2.2.1.23.** *Stereoscope images of six fatigued specimens showing surface damage (25X magnification).*

*Conclusion*

This research developed a robust and novel experimental procedure to measure the material relative nonlinear parameter using ultrasonic bulk waves. A fixture was constructed to minimize couplant variation in nonlinear ultrasonic testing. Additionally, the experimental results show reasonable repeatability and reliability, which also verified that the relative nonlinear parameter increases with the microstructure defect severity growth. Thus, fatigue failure of Alloy 617 should be predictable from nonlinear acoustics.

*2.2.1.3 Tensile Creep Samples*

Nonlinear acoustics measurements were made on a sequence of crept samples ($850^{\circ}$C and 69 MPa) having progressively higher creep strains (0.3, 0.4, 0.5, 0.6, 0.8, 0.9, 1.0 of the rupture strain).

Paste the abstract of Frank's thesis here. The full report on these bulk wave experiments are included as Appendix B, which is the M.S. thesis of Xiaochu Yao entitled, 'Bulk wave nonlinear acoustics evaluation of crept Inconel 617'.

*2.2.2 Guided Waves*

The development of nonlinear ultrasonic guided waves for nondestructive characterization of microstructural evolution is the heart of this project. We realized early in the project that mode selection was a key and that inspired theoretical analysis. Then numerical simulations and experiments could be founded on that analysis. In this section we provide a literature review of our research and related work of others as well as insight into how nonlinear ultrasonic guided waves can be employed. This section is adapted from an article that has been submitted for publication in an archival journal. While this section does not contain equations or many results, our research has generated a rich understanding of the subject through detailed analysis that is contained in our publications. Thus, our key publications in this area are included as Appendix C.

Elastic waves provide a number of methods to detect damage or material degradation. Ultrasonic guided waves are elastic waves that propagate in bounded geometries. The complex constructive and destructive interference patterns enable the waveguide cross-section to be fully energized and the waves to propagate long distances. Linear analysis of guided waves permits detection of changes in linear elastic constants and acoustic impedance changes that cause reflections and scattering. Nonlinear analysis of guided waves enables detection of small changes in the microstructure of the material that do not affect the linear elastic constants or result in detectable scattering. It is the distortion of the guided wave resulting from the microstructure changes that causes the generation of higher harmonics, which are then representative of the early stages of degradation. The ability of nonlinear ultrasonic guided waves to detect early degradation, sometimes referred to as damage precursors, is extremely attractive for structural health monitoring enabled condition based maintenance. The basis and methodology for utilizing guided waves for early damage detection is discussed. Then as an example,

the ability of the fundamental shear horizontal mode to characterize fatigue damage prior to the initiation of a macroscale crack is demonstrated on a set of 2024-T3 aluminum plates.

*The Shift to the Left*

Generally speaking, it is always better to detect accumulating damage sooner rather than later because that gives more time to take action. If the first indication of degradation is given right before the damage becomes critical it may be too late to avert failure, and certainly there is not time to plan maintenance actions and put in place the logistics necessary to have replacement parts, equipment, and manpower ready to go. Thus, fleet readiness is compromised. This is less of an issue in the schedule-based maintenance paradigm of today than it will be in the condition-based maintenance paradigm of tomorrow. The initial qualifier 'generally speaking' is used in recognition that false indications (either positive or negative) can become more prevalent as smaller defects are targeted.

An important objective of the non-destructive testing (NDT) and structural health monitoring (SHM) communities is a *shift to the left* along the service life axis for the earliest detection of damage [1] as shown in Figure 2.2.2.1. An example that shows the importance of non-destructive evaluation for fatigue life prediction is shown in Figure 2.2.2.2, where the number of cycles necessary for a fatigue crack to grow a unit amount, *dN/da* is plotted as a function of the number of cycles. Figure 2.2.2.2 not only shows that *dN/da* is monotonically decreasing, but that the remaining useful life is estimated by the area under the curve. This graph shows how important the current estimate of crack size is in fatigue life prediction because the area under the curve is so skewed to the left. These data are for growth of a single macroscale crack and do not address crack initiation. Clearly, *dN/da* must approach infinity prior to macroscale crack initiation, but that does not mean that degradation does not occur prior to macrocrack initiation. In fact, degradation such as short cracks, persistent slip bands, and dislocation substructures do occur in the microstructure of the material. Thus, an NDT or SHM method that is sensitive to the material microstructure could revolutionize life cycle management of structural systems.

One method to improve life prediction based on the shift to the left was proposed by Kulkarni and Achenbach [2]. It comprises a damage mechanics approach to account for microstructure evolution that leads to initiation of a macroscale fatigue crack, followed by a fracture mechanics based prediction of remaining useful life using a Paris-type power law relation for crack growth. Kulkarni and Achenbach suggested that nonlinear acoustics could be used to characterize the microstructure evolution portion of the multi-length scale model. It could be said that this is detection of damage before it occurs, if you consider the microstructure evolution that precedes initiation of a macroscale fatigue crack to be a precursor. This article describes how that might be accomplished.
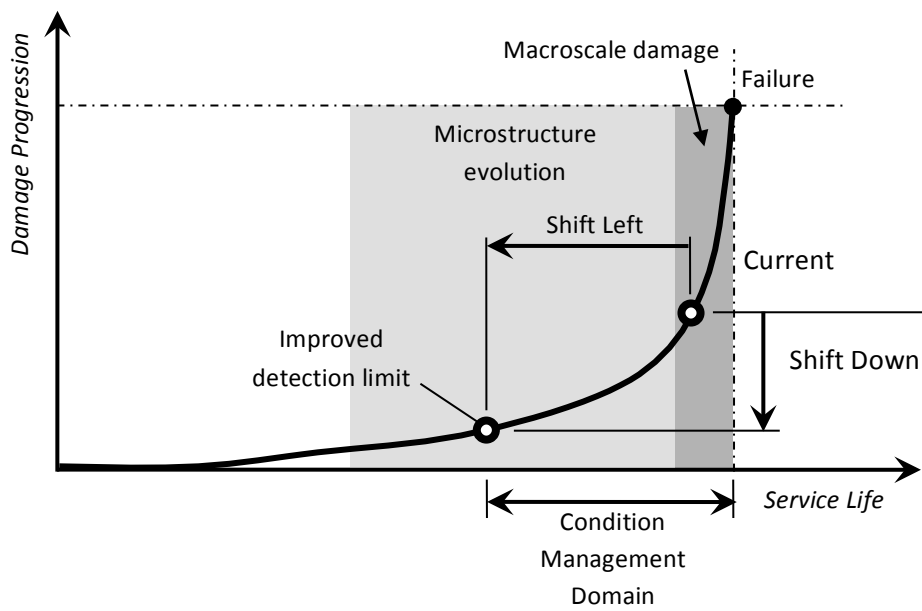
***Figure 2.2.2.1.*** *Shift to the left. As the minimum detectable damage shifts to the left relative to the service life the condition management domain increases.*
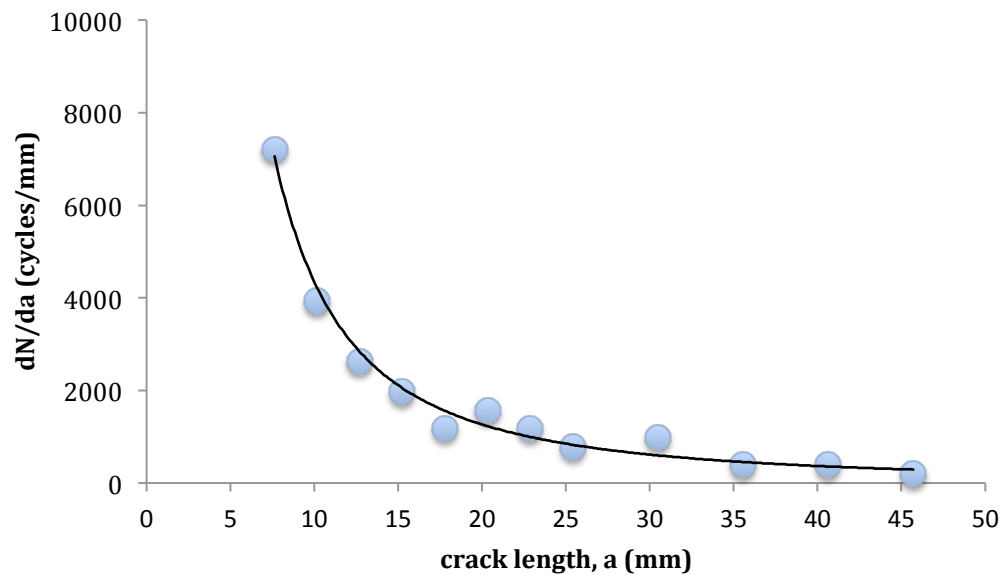


***Figure 2.2.2.2.*** *Cycles to grow crack a unit amount. Data for macrocrack growth in 7075-T6 aluminium for stress intensity ranges of 10-27 MPa-m$^{1/2}$.*

*Distortion of a Passing Wave*

In a linear elastic solid a monochromatic excitation results in simple harmonic motion since the restoring force is proportional to the displacement and the system oscillates at a monochromatic frequency. Hooke's law is a homogenized macroscale indication of what happens at the lower length scales, i.e., it is associated with the chemical bonds that bind solids. Interatomic forces of attraction and repulsion balance to create an equilibrium condition. When quadratic potentials are used to describe these forces the result is a linear relation between displacement and force, and subsequently simple harmonic motion. In terms of quantum mechanics, each atom/molecule is vibrating within the solid and monochromatic waves described by quadratic potentials do not interact. Within a solid continuum, when the vibration is small it can be described well by simple harmonic motion, but as it increases lattice anharmonicity becomes significant; i.e., the restoring force cannot keep up with the displacement. Thus, nonlinear vibration occurs that is described by non-quadratic potential functions that result in the existence of multiple frequencies of oscillation. Moreover from a continuum perspective, strain energy functions higher than order two result in self interactions and mutual interactions that distort the elastic wave. The distortion of elastic waves in real materials is small, but characterizable through the frequency spectrum.

In linear ultrasonics the interrogation signal is at the same frequency as the excitation such that there is sensitivity to discontinuities (on the order of the wavelength or larger) through acoustic impedance mismatch and degradation to the linear elastic properties through changes in velocity. However, linear elastic properties depend on material composition (chemical bonding) but not the microstructure. Thus, there is minimal sensitivity to microstructure. Nonlinear ultrasonics is based on interrogation signals at frequencies other than the excitation frequency. In this paper we consider higher harmonics associated with self interaction and combinational harmonics associated with mutual interaction, both of which result from distortion of passing elastic waves in nonlinear elastic media. Distortion of elastic waves is sensitive to microstructural changes such as creation of dislocation substructures, generation of persistent slip bands, and increase/decrease of precipitates because such changes affect the strain in the lattice and cause anharmonicity. In this way nonlinear ultrasonics is sensitive to the effects of microstructure changes at a scale much smaller than the wavelength. This sensitivity is due to the volume averaged effects of microstructure changes, not the microstructural feature itself.

*Why Nonlinear Guided Waves*

The fact that nonlinear elastic materials distort an elastic wave and generate higher harmonics was discovered by Breazeale and Thompson [3] and has been the subject of many laboratory experiments, e.g. [4-6] and much modelling, e.g. [7-8]. While a bit dated, reviews by Zheng et al. [9] and Jhang [10] are very thorough and informative. The overwhelming majority of the work has focused on bulk waves. However, despite the tremendous potential of nonlinear ultrasonics to detect very early indications of material degradation, the nonlinear bulk wave methods have not enjoyed industrial success. There may be numerous explanations for this, including: (1) the amplitude of the higher harmonic is miniscule relative to the primary wave; (2) the material nonlinearity must far exceed the measurement system nonlinearity to be successful; (3) the through-transmission mode is required, which means that access to

both sides of a component is necessary; (4) bulk waves propagate without interaction with boundaries, thus complex geometries of components will cause reflections that make measurements untenable; (5) transducer materials that exhibit strong piezoelectric coupling also exhibit material nonlinearity.

Guided waves, while complicated to represent mathematically, have certain advantages that could make nonlinear guided waves more successful than nonlinear bulk waves have been outside the laboratory. Guided wave propagation is multimodal and dispersive as determined by solving the dispersion relation, which includes satisfying boundary conditions in addition to the wave equation [11]. Guided waves can: energize all points within the cross-section of the waveguide, propagate long distances relative to bulk waves, interrogate hidden/inaccessible structures, be selected based on wavestructure at a certain mode-frequency combination to optimize defect sensitivity, and be focused at predetermined points by control of interference phenomena. Nonlinear guided wave propagation has been analysed and measured, e.g., [12-16]. In addition to the advantages of guided waves identified above, cumulative higher harmonics propagate longer distances meaning that the higher harmonics will grow more than those for bulk waves. Furthermore, because boundary conditions must be taken into account when developing the measurement setup, nonlinear guided waves may be more conducive to measurements on real components. However, much research and development remains to be done.

*Many Potential Applications*

Fatigue damage has been, by far, the most investigated application for nonlinear ultrasonics, e.g. [5-7], but it is just one of many. The progression of damage associated with fatigue follows a path very well suited for nonlinear ultrasonics – microstructure evolution followed by macroscale crack initiation and growth. Creep damage is another type of degradation investigated by nonlinear ultrasonics [17-18], as is plastic strain [19-20], thermal damage [21-22], radiation damage [23], and matrix cracking in a composite [24]. Other potential applications include stress corrosion cracking and creep-fatigue interaction in metal alloys, impact damage in composites, and microcracking in concrete. In each application the objective is a 'shift to the left' in detection as opposed to better sensitivity to macroscale damage. However, there are also many applications where the objective is to improve sensitivity to macroscale damage, e.g. [25]. It is well worth noting that damage progression is often localized rather than uniform, therefore the methods to detect it need to be amenable to heterogeneous materials.

*The Keys to Success*

The success of nonlinear ultrasonics to shift the earliest detection of damage to the left on the service life axis is reliant upon an understanding of the physics of the problem, a mathematical description of those physics, and hardware to physically generate weakly nonlinear ultrasonic waves. Lets start with the hardware necessary to actuate an elastic wave. A long toneburst pulse is used to obtain a narrow frequency bandwidth, and the number of cycles is often dictated by the geometry of the sample since reflections and scattering can make reception of a clean waveform problematic. The narrow bandwidth is desired in order to not mask the higher harmonics to be interrogated. As the higher harmonics are quite small relative to the primary wave the cleanest possible waveform is needed to minimize distortion and keep the noise floor as low as possible. Furthermore, the primary wave amplitude must

be high to generate measurable higher harmonics. Therefore, the electric signal generator, its amplifier, the transducer that converts the electric signal into mechanical energy, and the coupling of the transducer to the test material must all be carefully selected. After the wave has propagated through the test material it must be received by a transducer sensitive to the higher harmonic content, windowed, and then transformed into the frequency domain.

The importance of selection of a primary guided wave mode to generate a higher harmonic guided wave cannot be overstated because a mode might not exist at twice (or three times) the excitation frequency, and even if it does there may not be power flux between the primary mode and the secondary mode. De Lima and Hamilton [13] showed by reciprocity and the normal mode expansion that cumulative second harmonics only occur when the internal resonance condition is met: (1) primary and secondary wave modes are synchronized and (2) there is nonzero power flux from the primary to secondary wave modes. Cumulative second harmonics increase linearly with propagation distance when generated by a plane wave and attenuation is negligible. This is a very valuable feature, as it can be used in the laboratory to ensure the higher harmonic being generated is from the material and not the measurement system.

Analyses have been conducted to show when primary and secondary waves are synchronized as well as that there is zero power flux to many types of secondary wave modes [13-16, 26-28]. The results of these analyses indicate that the choices of primary wave modes and frequencies that generate cumulative higher harmonics is quite limited [29]. Considering cumulative second harmonic generation, the best mode pairs for plates and pipes are shown in Tables 2.2.2.1 and 2.2.2.2 for the phase velocity dispersion curves shown in Figures 2.2.2.3 and 2.2.2.4 respectively, with *fd* being the frequency-thickness product. Symmetric and antisymmetric Rayleigh-Lamb (RL) modes and shear horizontal (SH) modes are shown for plates in Figure 2.2.2.3. While axisymmetric longitudinal L(0,m) and axisymmetric torsional T(0,m) modes are shown in Figure 2.2.2.4. Points where the internal resonance criteria are satisfied are shown in the figures and the points with strongest power flux are labelled and tabulated. Notice that the group velocity of the second harmonic is significantly higher than the group velocity of the primary mode for internal resonance points 4-6 for both plates and pipes, meaning that the second harmonic will be received significantly before the primary wave arrives given a sufficient propagation distance [30]. For plates the second harmonic waves are always symmetric RL modes, while for pipes they are always axisymmetric longitudinal modes. Even though the pipe geometry results in a significantly different boundary value problem than the plate geometry the best internal resonance points are essentially the same [27-29]. Flat plate geometries are easier to analyse than hollow cylinders because a Cartesian coordinate system can be used rather than a curvilinear one. However, we are interested in both, and the analysis of Chillara and Lissenden [31] showed that axisymmetric waves in pipes approach their counterparts in plates in the asymptotic limit. As an extension of axisymmetric waves in pipes, the generation of nonlinear flexural modes has been fully analysed [32-33].

Due to the limited number of internal resonance points for second harmonics other options have been sought. Third harmonics in plates provide some attractive options based on the analysis [33] and experiments on aluminium plates [20]. The advantages specific to SH modes include: (1) the third harmonic is a SH mode, (2) all points on SH dispersion curves have internal resonance with third

harmonic modes, and (3) SH modes have good excitability with magnetostrictive transducers. Furthermore, since the fundamental SH mode is nondispersive the third harmonic is the same mode, which has a uniform displacement profile through the thickness of the plate. This simplicity is desirable and helpful for measurements. Mode mixing, whether collinear or oblique, requires analysis of combinational harmonics such as $f_1 + f_2$ and $f_1 - f_2$, but drastically widens the space from which internal resonance points can be selected. And while it requires two transmitters and a receiver, combinational harmonics can be selected to occur at frequencies other than higher harmonics of the transmitters, which is a distinct advantage for the measurement system.

Once the primary and secondary wave modes have been selected, transducers to send and receive must be chosen. As indicated earlier the amplitude of the primary needs to be as large as possible. In fact, choosing a mode with good excitability [11] is an integral part of the previously described mode selection. For example, the S1/S2 mode pair is desirable because it has strong power flux, but it has very low excitability with a gel-coupled angle beam transducer. However, replacing the gel couplant with adhesive improves the excitability because it facilitates in-plane displacement at the surface of the plate to match the S1 mode displacement profile. Another example already mentioned is that the SH0 mode has strong excitability with a magnetostrictive transducer.
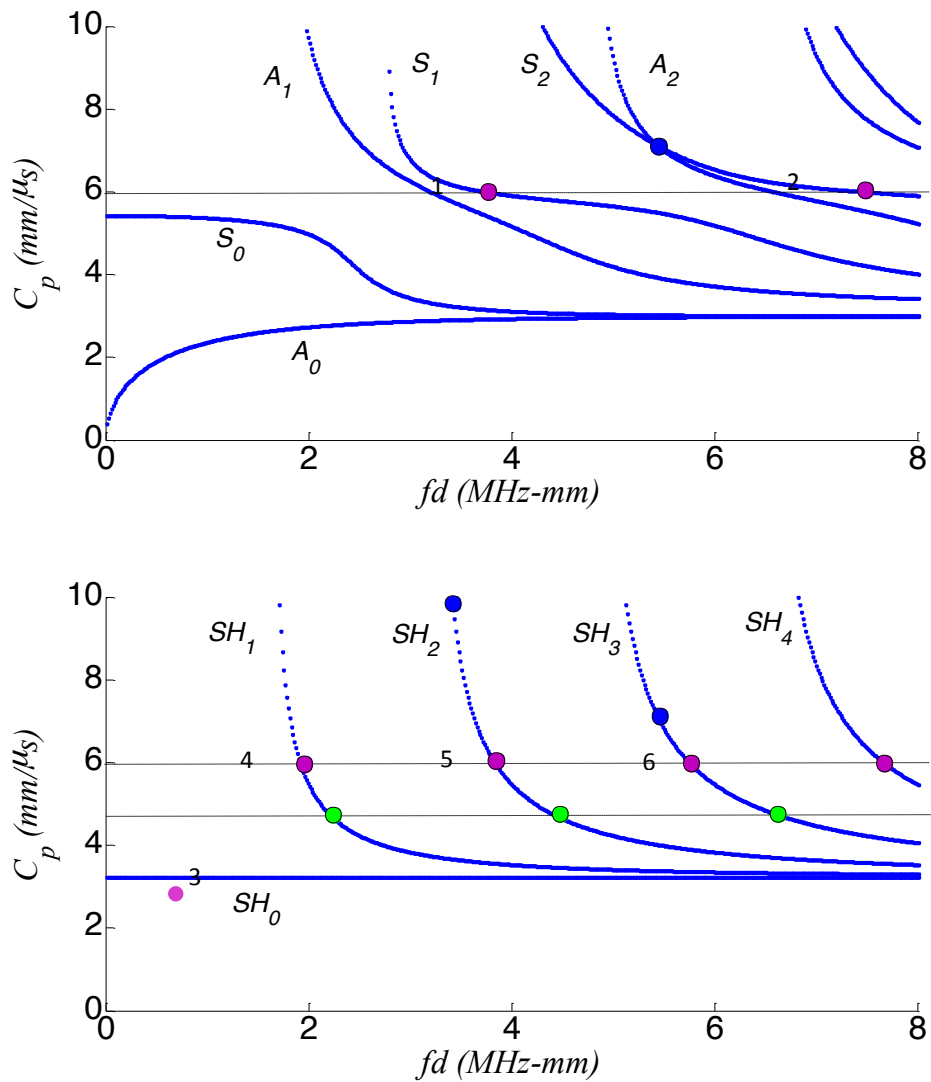
**Figure 2.2.2.3**. *Steel plate dispersion curves. RL modes (top) and SH modes (bottom) with second harmonic internal resonance points marked.*

**Table 2.2.2.1.** *Best internal resonance points for steel plates.*

| Internal Resonance Point | Mode Pair | Frequency-Thickness (MHz-mm) | Phase Velocity (mm/ms) | Group Velocity (mm/ms) |
|---|---|---|---|---|
| 1 | S1/S2 | 3.85 | 5.96 | 4.88/4.86 |
| 2 | S2/S4 | 7.70 | 5.96 | 4.86/4.98 |
| 3 | SH0/S0 | 1.72 | 3.23 | 3.23/4.43 |
| 4 | SH1/S1 | 1.92 | 5.96 | 1.74/4.86 |
| 5 | SH2/S2 | 3.85 | 5.96 | 1.75/4.92 |
| 6 | SH3/S3 | 5.78 | 5.96 | 1.74/5.09 |
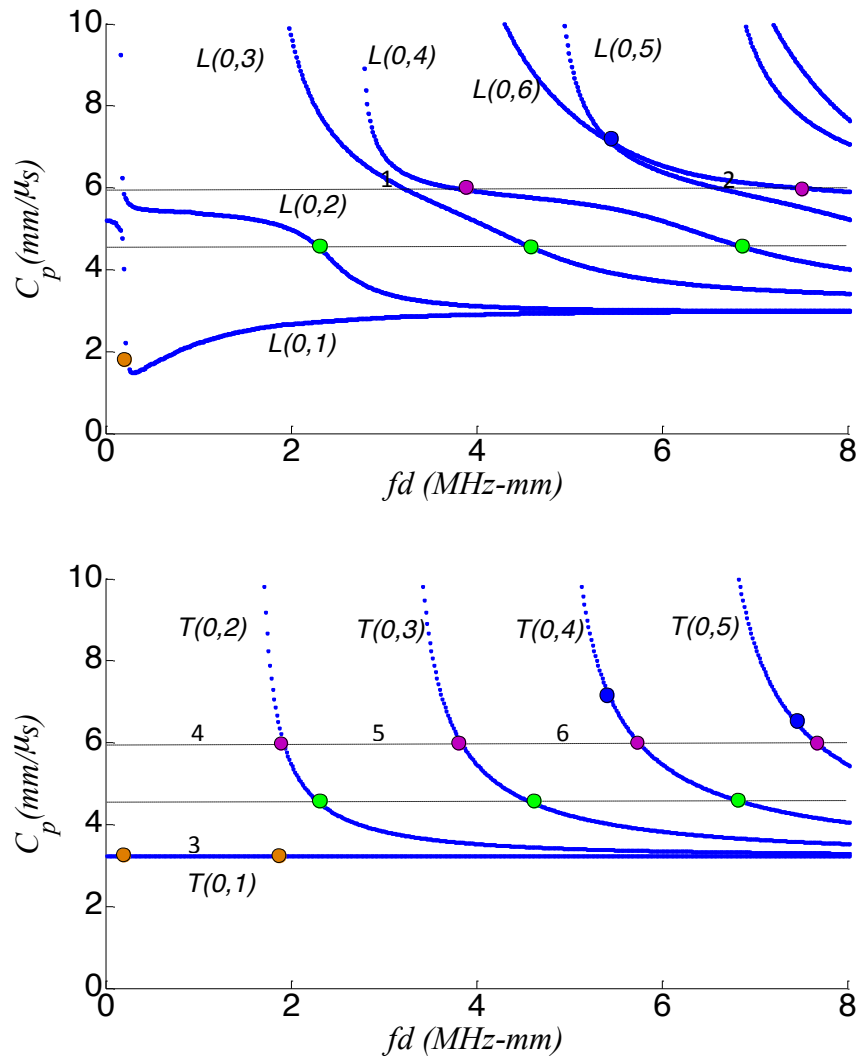
**Figure 2.2.2.4.** *Steel pipe dispersion curves. Axisymmetric longitudinal modes (top) and torsional modes (bottom) with second harmonic internal resonance points marked. Inner radius is 9 mm.*

**Table 2.2.2.2.** *Best internal resonance points for steel pipes.*

| Internal Resonance Point | Mode Pair | Frequency-Thickness (MHz-mm) | Phase Velocity (mm/ms) | Group Velocity (mm/ms) |
|---|---|---|---|---|
| 1 | L(0,4)/L(0,5) | 3.85 | 5.96 | 4.86/4.92 |
| 2 | L(0,5)/L(0,8) | 7.70 | 5.96 | 4.92/5.18 |
| 3 | T(0,1)/L(0,2) | 1.72 | 3.23 | 3.23/4.43 |
| 4 | T(0,2)/L(0,4) | 1.92 | 5.96 | 1.74/4.86 |
| 5 | T(0,3)/L(0,5) | 3.85 | 5.96 | 1.75/4.92 |
| 6 | T(0,4)/L(0,7) | 5.78 | 5.96 | 1.74/5.09 |

To wrap up this section, it is important to recognize that simply demonstrating that higher harmonics change as a function of microstructure evolution is a start, but insufficient to revolutionize life cycle management. The changes in higher harmonic content need to be quantitatively correlated with the actual microstructure evolution, which in turn must be related to the damage state and final failure. Very little progress has been made to positively correlate higher harmonic with well documented damage induced microstructural evolution although the work of Cantrell [7] and Cash and Cai [8] is a start.

*A Simple Sample Problem*

To demonstrate application of the aforementioned approach for using nonlinear ultrasonic guided waves for early damage detection we consider fatigue. Simple laboratory experiments were conducted on 2024-T3 aluminum plate samples. Six samples 1 mm thick by 64 mm wide by 605 mm long having a reduced gage section 38 mm wide by 229 mm long were cut. One sample was cycled to failure in $N_f$ = 4539 cycles with maximum and minimum stresses of 345 and 35 MPa respectively. Then four samples were cycled to 80, 60, 40, and 20% of $N_f$, while another sample was not loaded.

The third harmonic of the SH0 mode was selected as the higher harmonic to detect early fatigue damage because of the strong excitability of the SH0 mode with a magnetostrictive transducer, and because the nondispersive nature of the SH0 mode makes it internally resonant with high power flux. Generation of third harmonic guided waves in plates was fully analysed by Liu et al. [34]. The magnetostrictive transducers consist of an iron-cobalt foil bonded to the sample, a meandering electric coil, and a permanent magnet. The meander coil spacing sets the primary wavelength sent or received by the transducer. Thus, for optimal reception of the third harmonic the receiver coil spacing is 1/3 of the transmitter coil spacing. Coil spacings corresponding to wavelengths of 3.6 and 1.2 mm were used for the transmitter and receiver respectively. The wave propagation length was approximately 240 mm.

The RAM-5000 SNAP (Ritec, Inc., Warwick RI, USA) instrument was used to generate a 15-cycle toneburst with central frequency of $f_0$ = 0.83 MHz. A matching network with an integrated low pass filter suppresses instrument distortion of the signal sent to the transmitter. The receiving transducer also has a matching network and preamplifier that sends the output signal to an oscilloscope where it is digitized. Signal processing consists of zero padding the Tukey windowed waveform and fast Fourier transforming to the frequency domain. From the frequency spectrum the relative nonlinear parameter, $A_3/A_1^3$, is computed from the frequency peaks $A_1$ and $A_3$ at $f_0$ and $3f_0$ respectively. The A-scan signal and the frequency spectrum of the windowed waveform are shown in Figure 2.2.2.5.
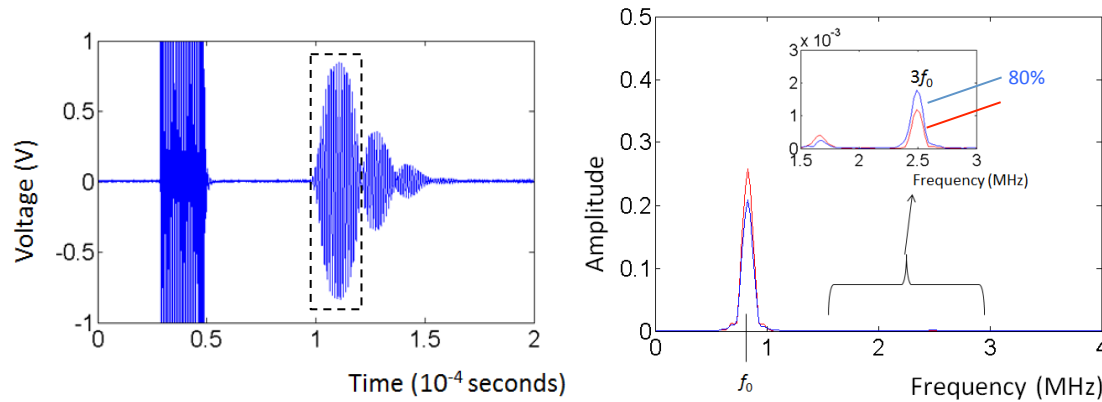
**Figure 2.2.2.5.** *Results for 2024-T3 aluminum; A-scan for 0% fatigue life (left), frequency spectra for 0% and 80% of the fatigue life (right).*

After bonding the iron-cobalt foils to a sample with cyanoacrylate, a sequence of 10 replicate measurements was made by placing and replacing the coils and magnets. The mean and standard error (a measure of the precision of the mean) were computed for each of the five samples. Note that the standard deviation is equal to the standard error times the square root of the population sample size. The relative nonlinearity parameter is normalized with respect to its value for the undamaged sample and then these values are plotted as a function of fatigue life in Figure 2.2.2.6. Both the mean and standard error are shown as well as a third order polynomial curve fit to the mean values. These data can be understood in terms of the expected fatigue damage. The maximum stress of 345 MPa is the yield strength of the alloy, thus there is no significant gross plastic deformation but there is surely localized plastic deformation and probably formation of persistent slip bands. Likewise, no macroscale fatigue cracks were observed in any of the samples. While no microstructural investigation was undertaken, it seems plausible that the dislocation substructures that were initially widely spaced became larger barriers that are more closely spaced together causing the volume average of the local lattice strain to increase exponentially. Thus it appears reasonable that the nonlinearity parameter also increases exponentially once the microstructure evolution becomes significant.
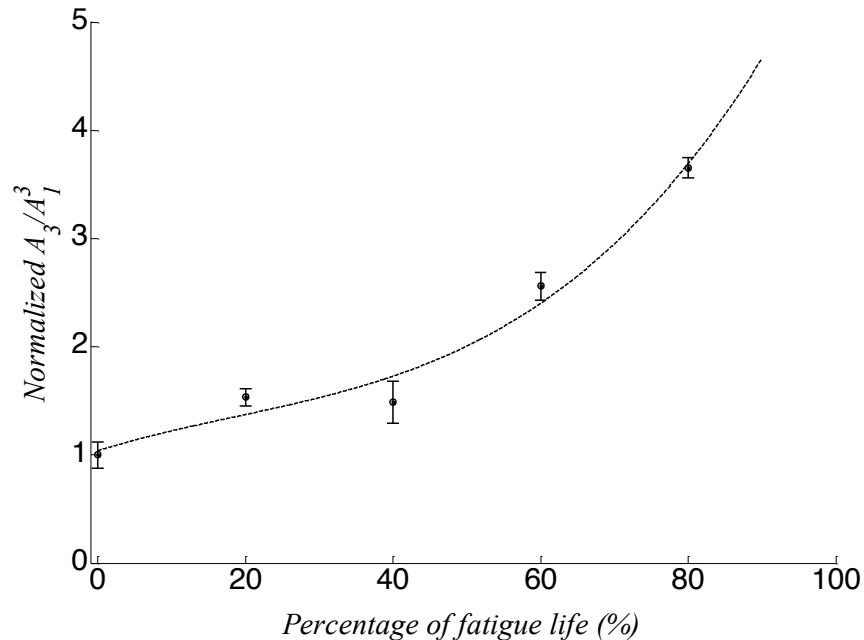
**Figure 2.2.2.6.** *Increasing third harmonic with fatigue life. The relative nonlinear parameter increases by a factor of almost 4 as cyclic loading continues to 80% of the fatigue life for 2024-T3 aluminum.*

*Conclusions*

The importance of early detection of damage in structural materials in terms of a condition based maintenance paradigm has been stressed. Nonlinear ultrasonic guided waves were described as having strong potential for early detection of damage in structural systems. Internally resonant guided wave mode pairs (primary mode/second harmonic) were identified for plates considering both Rayleigh Lamb and shear horizontal wave types and in pipes considering axisymmetric longitudinal and torsional wave types. As the number of options is limited, third harmonics and combination harmonics were discussed. A set of experiments showing the strong sensitivity of the third harmonic shear horizontal wave to fatigue degradation that occurs prior to the initiation of a macroscale crack demonstrates the potential of nonlinear ultrasonics for early damage detection.

*References*

1. L J Bond, 'Through the looking glass – the future for NDE?', Rev. Progress in Quant. Nondestruct. Eval., Vol 33 p 21, 2014.

2. S S Kulkarni and J D Achenbach, 'Structural health monitoring and damage prognostics in fatigue', Struct. Health Mon., Vol 7 pp 37-49, 2008.

3. M A Breazeale and D O Thompson, 'Finite-amplitude ultrasonic waves in aluminum', Appl. Phys. Lett., Vol 3, p 77-78, 1963.

4. A Hikata, B B Chick, and C Elbaum, 'Effect of dislocations on finite amplitude ultrasonic waves in aluminum', Appl. Phys. Lett., Vol 3, pp 195-197, 1963.

5. J H Cantrell and W T Yost, 'Nonlinear ultrasonic characterization of fatigue microstructures', Int. J. fatigue, Vol 23, pp 487-490, 2001.

6. J Y Kim, L J Jacobs, J Qu, J W Littles, 'Experimental characterization of fatigue damage in nickel-base superalloy using nonlinear ultrasonic waves', J. Acoust. Soc. Am., Vol 120, pp 1266-1273, 2006.

7. J H Cantrell, 'Substructural organization, dislocation plasticity and harmonic generation in cyclically stressed wavy metals', Proc. Roy. Soc. London, Vol A460, pp 757-780, 2004.

8. W D Cash and W Cai, 'Contribution of dislocation dipole structures to the acoustic nonlinearity', J. Appl. Phys., Vol 111, 074906, 2012.

9. Y Zheng, R G Maev, and I Y Solodov, 'Nonlinear acoustic applications for material characterization: a review', Can. J. Phys., Vol 77, pp 927-967, 1999.

10. K Y Jhang, 'Nonlinear ultrasonic techniques for nondestructive assessment of micro damage in material: a review', Int. J. Prec. Engng. Manuf., Vol 10, pp 123-135, 2009.

11. J L Rose, Ultrasonic Guided Waves in Solid Media, Cambridge, 2014.

12. M Deng, 'Cumulative second-harmonic generation of generalized Lamb-wave propagation in a solid waveguide', J. Phys. D, Vol 33, pp 207-215, 2000.

13. W J N de Lima and M F Hamilton, 'Finite-amplitude waves in isotropic elastic plates', J. Sound Vib., Vol 265, pp 819-839, 2003.

14. A Srivastava and F Lanza di Scalea, 'On the existence of antisymmetric or symmetric Lamb waves at nonlinear higher harmonics', J. Sound Vib., Vol 323, pp 932-943, 2009.

15. M F Muller, J Y Kim, J Qu, and L J Jacobs, 'Characteristics of second harmonic generation of Lamb waves in nonlinear elastic plates', J. Acoust. Soc. Am., Vol 127, pp 2141-2152, 2010.

16. V K Chillara and C J Lissenden, 'Interaction of guided wave modes in isotropic nonlinear elastic plates: higher harmonic generation', J. Appl. Phys., Vol 111, 124909, 2012.

17. S Baby, K B Nagaraja, C M Omprakash, D V V Satyanarayana, K Balasubramaniam, and V Kumar, 'Creep damage assessment in titanium alloy using a nonlinear ultrasonic technique', Scripta Mat., Vol 59, pp 818-821, 2008.

18. Y Xiang, M Deng, F Z Xuan, and C J Liu, 'Effect of precipitate-dislocation interactions on generation of nonlinear Lamb waves in creep-damaged metallic alloys', J. Appl. Phys., Vol 111, 104905, 2012.

19. C Pruell, J Y Kim, J Qu, and L J Jacobs, 'Evaluation of plasticity driven material damage using Lamb waves', Appl. Phys. Lett., Vol 91, 231911, 2007.

20. C J Lissenden, Y Liu, G W Choi, and X Yao, 'Effect of localized microstructure evolution on higher harmonic generation of guided waves', J. Nondestruct. Eval., Vol 33, pp 178-186, 2014.

21. C S Kim and C J Lissenden, 'Precipitate contribution to the acoustic nonlinearity in nickel-based superalloy', Chin. Phys. Lett., Vol 26, 086107, 2009.

22. C Nucera and F Lanza di Scalea, 'Nonlinear wave propagation in constrained solids subjected to thermal loads', J. Sound Vib., Vol 33, pp 541-554, 2014.

23. K H Matlack, J J Wall, J Y Kim, J Qu, L J Jacobs, and H W Viehrig, 'Evaluation of radiation damage using nonlinear ultrasound', J. Appl. Phys., Vol 111, 054911, 2012.

24. N Rauter and R Lammering, 'Experimental investigation of impact damages in composites by second harmonic Lamb waves', 6$^{th}$ ECCOMAS Conference on Smart Structures and Materials, Politecnico di Torino, 12 pages, 2013.

25. K E A Van Den Abeele, P A Johnson, and A Sutin, 'Nonlinear elastic wave spectroscopy (NEWS) techniques to discern material damage, part I: nonlinear wave modulation spectroscopy (NWMS)', Res. Nondestr. Eval., Vol 12, pp 17-30, 2000.

26. N Matsuda and S Biwa, 'Phase and group velocity matching for cumulative harmonic generation in Lamb waves', J. Appl. Phys., Vol 109, 094903, 2011.

27. Y Liu, V K Chillara, and C J Lissenden, 'On selection of primary modes for generation of strong internally resonant second harmonics in plate', J. Sound Vib., Vol 332, pp 4517-4528, 2013.

28. Y Liu, E Khajeh, C J Lissenden, and J L Rose, 'Interaction of torsional and longitudinal guided waves in weakly nonlinear circular cylinders', J. Acoust. Soc. Am., Vol 133, pp 2541-2553, 2013.

29. Y Liu, C J Lissenden, and J L Rose, 'Cumulative second harmonics in weakly nonlinear plates and shells', Health Monitoring of Structural and Biological Systems, Vol 8695, 896528, 2013.

30. V K Chillara and C J Lissenden, 'Nonlinear guided waves in plates: a numerical perspective', Ultrasonics, Vol 54, pp 1553-1558, 2014.

31. V K Chillara and C J Lissenden, 'Analysis of second harmonic guided waves in pipes using a large-radius asymptotic approximation for axis-symmetric longitudinal modes', Ultrasonics, Vol 53, pp 862-869, 2013.

32. Y Liu, C J Lissenden, J L Rose, 'Higher order interaction of elastic waves in weakly nonlinear circular cylinders. I. analytical foundation', J. Appl. Phys., Vol 115, 214901, 2014.

33. Y Liu, E Khajeh, C J Lissenden, J L Rose, 'Higher order interaction of elastic waves in weakly nonlinear circular cylinders. II. physical interpretation and numerical simulation', J. Appl. Phys. Vol 115, 214902, 2014.

34. Y Liu, V K Chillara, C J Lissenden, J L Rose, 'Third harmonic shear horizontal and Rayleigh Lamb waves in weakly nonlinear plates', J. Appl. Phys., Vol 114, 114908, 2013.

### *2.2.2.1 Nonlinear Ultrasonic Guided Waves for Nondestructive Characterization of Degradation in Alloy 617 Pipes*

*Multiaxial High Temperature Strain Ratcheting Test*

The aim of this study was to investigate whether the T(0,1) mode third harmonic is sensitive to ratcheting, a progressive accumulation of strain that occurs over a number of cycles. The T(0,1) mode is the fundamental torsional mode in a pipe, which is axisymmetric, nondispersive, and analogous to the SH0 mode in a plate. In this case ratcheting of the axial strain for constant axial stress is associated with symmetric shear strain cycling. Very large deformations are possible with ratcheting and can render components, such as intermediate heat exchangers for very high temperature reactors, nonfunctional before the intended service live is over. Alloy 617 is a candidate material for components of very high temperature reactors due to its high corrosion resistance, creep resistance and ability to retain its mechanical properties over a wide range of temperatures.

Three Alloy 617 thin wall tubular specimens, whose composition in weight % is listed in Table 2.2.2.3 and nominal pre-test dimensions are shown in Figure 2.2.2.7, were each tested on a MTS Axial-Torsional rig with the control modes of constant applied axial stress (12 MPa) and cyclic shear strain with amplitudes such that $\Delta\gamma/(2\sqrt{3})$ = +/-0.004 rad with a constant 0.04%/s strain rate. Induction heating provided the nominal test temperature of 850°C. Complete details of the mechanical testing are provided in Appendix A, key aspects of the results are summarized here. Specimen 4-5-1 was first tested until failure, after 955 shear strain cycles the upper limit of the axial force was triggered due to instability that occurred as a result of fracture. Recorded signals of the control modes are given in Figure 2.2.2.8, which shows constant applied axial stress and cyclic shear strain. The final axial strain value was 0.065 m/m for specimen 4-5-1. Two additional specimens, 4-17-7 and 4-17-8, were tested under the same loading path at 850°C, but were interrupted at axial strain accumulations to 58% (0.0376 m/m) and 71% (0.0465 m/m) of the final axial strain value (0.065m/m) of the failed specimen, respectively. The original intent was to have interruptions at 70% and 90%. However, these two specimens exhibited a slightly slower axial strain ratcheting rate than specimen 4-5-1, and was an indicator for possible specimen variability in the accumulated ratcheted axial strain value at failure. Prior tests at 850°C with lower cyclic shear strain amplitudes failed with accumulated axial strain ranges of 0.054 m/m to 0.0645 m/m.

*__Table 2.2.2.3.__ Composition in weight % for Alloy 617 used in this research.*

| Ni | Cr | Co | Mo | C | Fe | Al | Ti | Si | Mn | Cu |
|---|---|---|---|---|---|---|---|---|---|---|
| Balance | 21.9 | 11.4 | 9.3 | 0.08 | 1.7 | 1.0 | 0.3 | 0.1 | 0.1 | 0.04 |
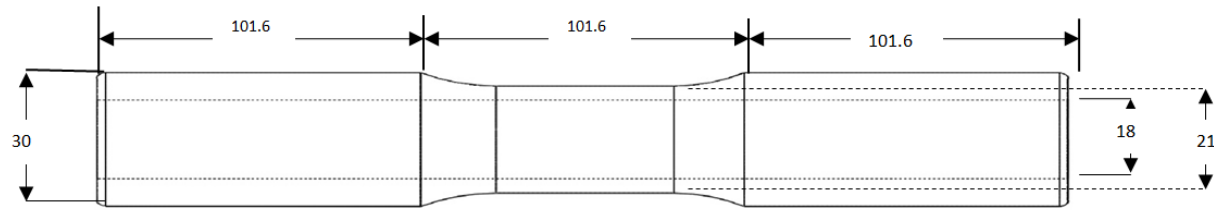
*Figure 2.2.2.7. Tubular specimen with dimensions in mm.*

The control path is shown in Figure 2.2.2.8, where the dots following a vertical projection correspond to the initial ramp up to the constant axial stress at zero shear strain. The resulting strain accumulation curve as a function of time is shown in Figure 2.2.2.9. Ratcheting for the interrupted tests on specimens 4-17-7 and 4-17-8 followed the same strain accumulation path, which was below that of specimen 4-5-1. Table 2.2.2.4 provides test details for the four experiments.
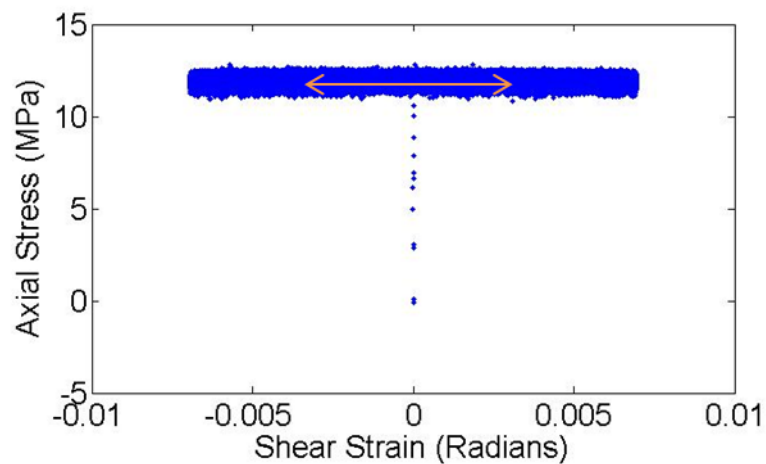


***Figure 2.2.2.8***. *Control signals of 850C biaxial experiments (constant applied axial stress and cyclic shear strain) to induce axial strain ratcheting.*

**Table 2.2.2.4**. Test details

| Specimen Name | Interrupted axial strain | Final strain (m/m) | Run Time (min) | Outer diameter between Fe-Co foils (mm) |
|---|---|---|---|---|
| 4-5-1 | 100% | 0.0654 | 635.2 | N.A. |
| 4-17-8 | 71% | 0.0465 | 575.9 | 20.42-20.81 |
| 4-17-7 | 58% | 0.0376 | 448.6 | 20.5-21.24 |
| 4-17-1 | 0% | 0 | 0 | 20.88-21.09 |
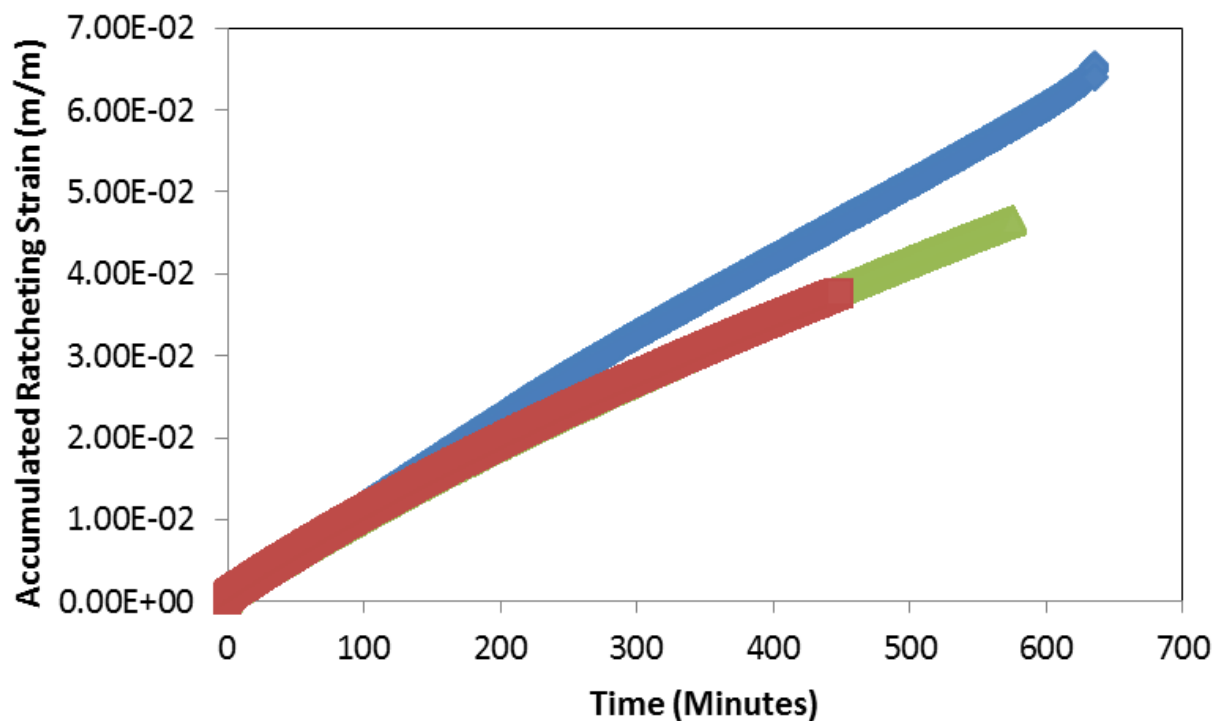


**Figure 2.2.2.9**. Accumulated axial ratcheting strain as a function of time for specimen 4-5-1 (Blue) and following tests interrupted at 71% and 58% of the accumulated (ratcheted) axial strain to failure.

*Nonlinear Ultrasonic Characterization Using the Axisymmetric Mode T(0,1)*

After high temperature mechanical testing, the grip ends were turned down on a lathe to the outer diameter dimension of the gage section (~21 mm) to make them into pipe sections. The nonlinear ultrasonic experiment setup involved two magnetostrictive transducers used in through-transmission mode. The transducers were designed for torsional waves with particle displacement in the

circumferential direction and wave propagation direction along the length of the pipe. The torsional T(0,1) mode in pipes is analogous to the fundamental shear horizontal (SH0) within plates. The dispersion curves are shown in Figure 2.2.2.4. Each magnetostrictive transducer includes an iron cobalt foil, a meander electric coil, and a permanent magnet. Two iron cobalt foils 50.8 mm x 72 mm were bonded to the lathed ends of the specimen surface with cyanoacrylate 77 mm apart. To prevent debonding of the iron cobalt from the curved surface of the specimen, it was bonded with a slight overlap of about 5 mm in the circumferential direction. The meander electric coils were wrapped around the iron cobalt and designed to have wavelengths of 3.6 and 1.2 mm corresponding to transmitter and receiver with 5 turns each. Two 6.35 mm diameter by 25.4 mm long cylindrical magnets were wrapped in 2 layers of 2 mm thick flexible rubber and placed within the pipe such that each was placed generally concentric to the meander electric coils, where the cross section of the pipe with the schematic of the magnetostrictive transducer is shown in Figure 2.2.2.10. For further clarification, the general design of each meander coil can be shown by unwrapping the pipe into a rectangular sheet as shown in Figure 2.2.2.11, where the same design could be used to generate a shear horizontal mode. Half yellow arrows indicate the magnetic field direction, half red arrows indicate alternating current direction, red arrows at both ends indicate particle motion, which is perpendicular to the wave propagation direction. The center-to-center distance of the transmitter and receiver coils was 89 mm. This setup includes a Ritec SNAP RAM 5000 system (with internal high power gated amplifiers) to excite a 10 cycle tone burst at $f_0$=0.85 MHz from the magnetostrictive transmitter, with additional components including the 50 Ohm transmitter/receiver impedance matching network, oscilloscope for recording the time domain signal, as shown schematically in Figure 2.2.2.11 and in the photographs of Figures 2.2.2.12 and 2.2.2.13. The receiver senses the wave that has propagated through the deformed region and sends the signal to the oscilloscope for time domain signal acquisition. Matlab was used for signal processing.

Just as the SH0 mode generates an internally resonant third harmonic of the same mode, the T(0,1) mode generates an internally resonant third harmonic T(0,1) mode. Thus, our expectation is that this T(0,1) third harmonic will be sensitive to microstructure evolution. Laboratory experiments on the three samples with different amounts of ratcheting strain will be used as a demonstration.
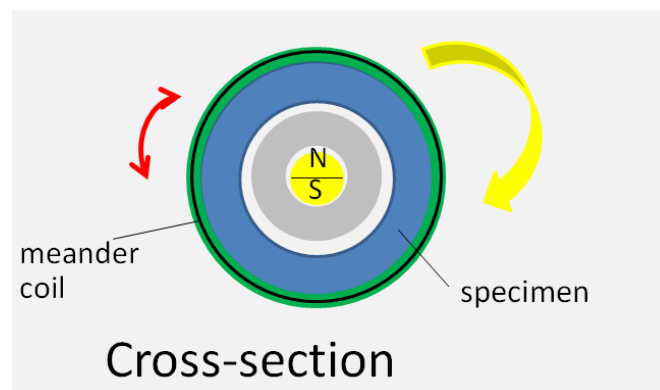


*Figure 2.2.2.10. Schematic of experimental test setup for torsional mode T(0,1) in pipe.*
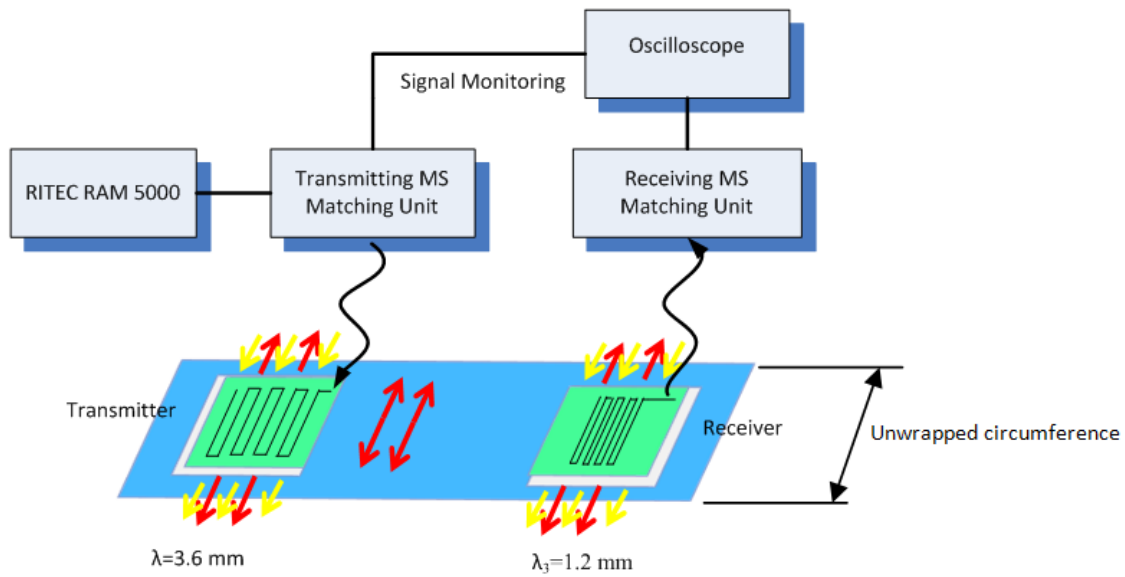
**Figure 2.2.2.11**. *Schematic of experimental test setup for torsional modes in pipe, shown here unwrapped as a rectangular sheet to show the analogy with shear horizontal modes in plate.*
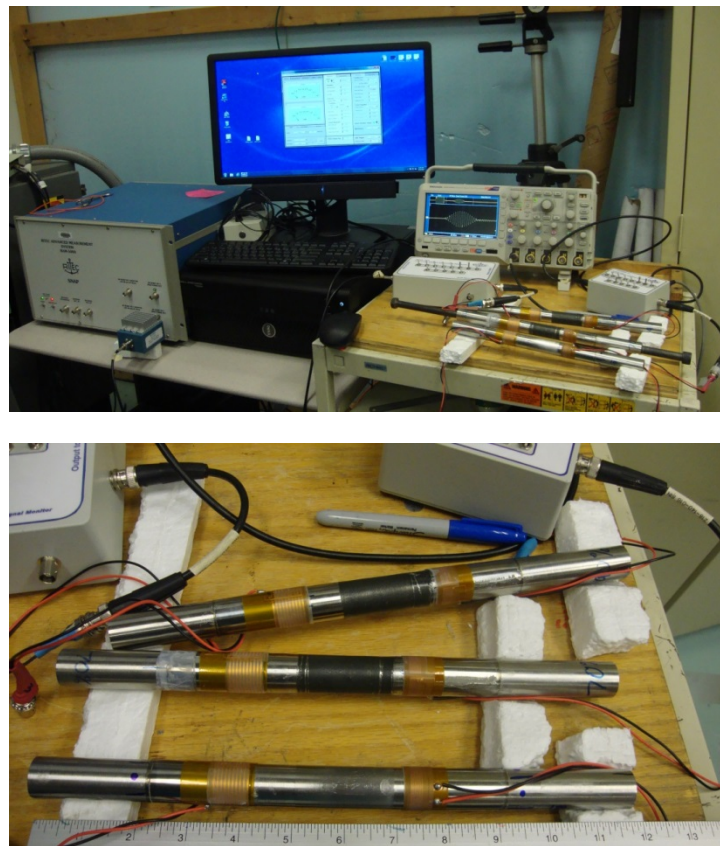




**Figure 2.2.2.12**. *Photographs of experimental setup and specimens (as received, 71% ad 58%).*
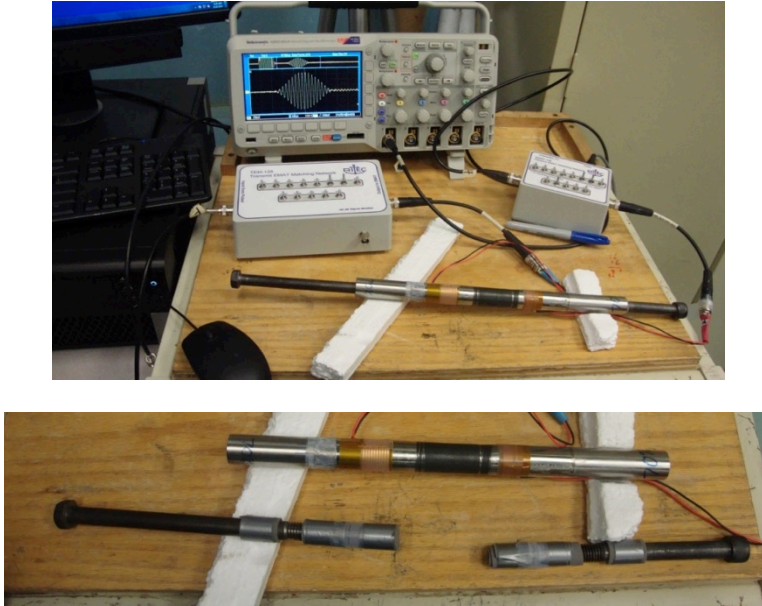
***Figure 2.2.2.13***. *Each magnet was attached to a metal rod and placed so that it was within the pipe and generally concentric with the meander electric coils (orange).*

To indirectly characterize the system nonlinearity from components such as the transducer and other electronics, we measure the modal amplitude ratio as a function of output power level for the Ritec system on the as-received specimen 4-17-1 with the magnetostrictive transducers prepared as noted earlier. These measurements demonstrate that a power output level between 80-100% is where the system nonlinearity contribution is overwhelmed by the material nonlinearity.
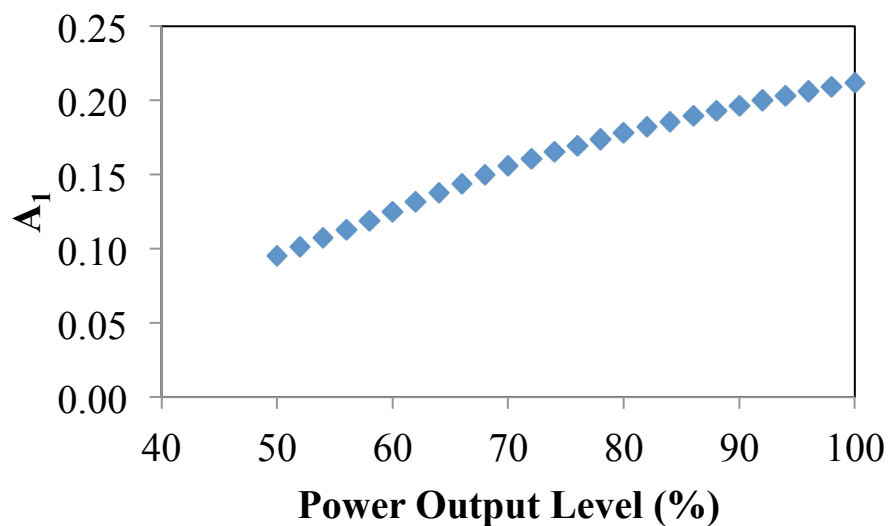


(a)
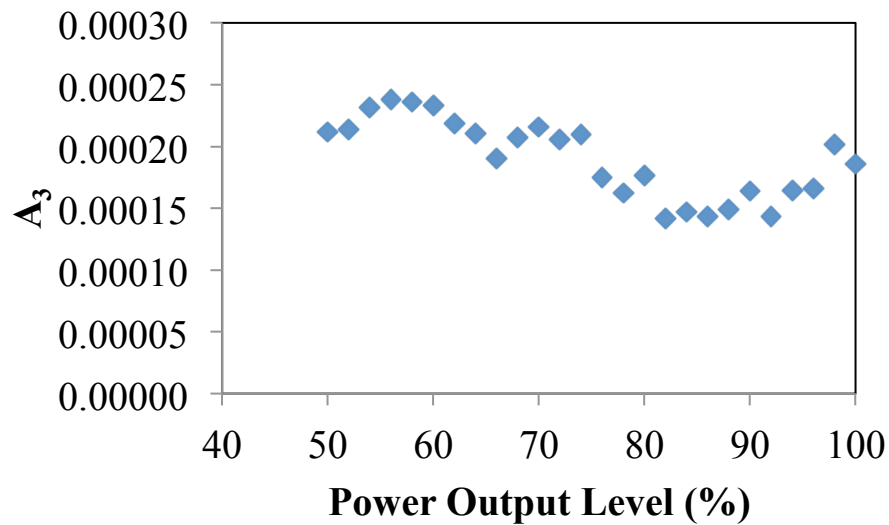
(b)
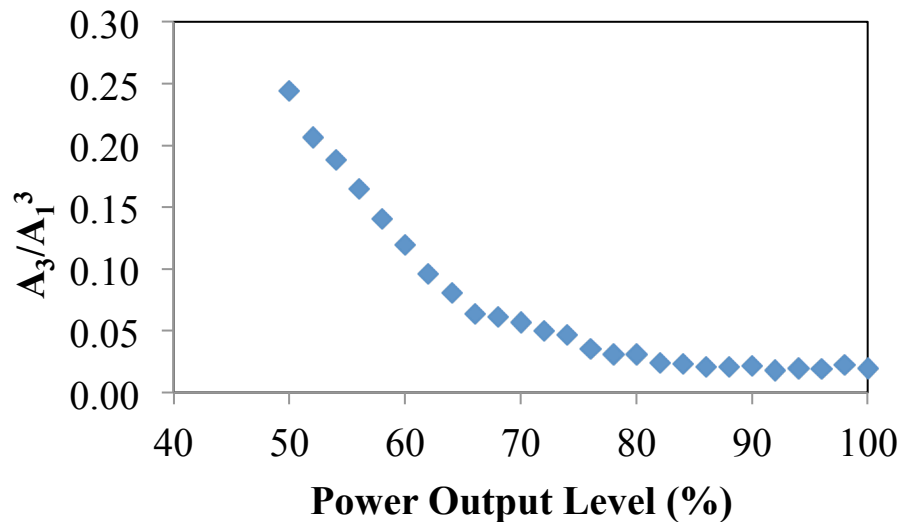


(c)

**Figure 2.2.2.14**. *(a) Amplitude of primary mode T(0,1), (b) amplitude of the third harmonic T(0,1), and modal amplitude ratio $A_3/A_1^3$ as a function of power output level (%).*

Further nonlinear ultrasonic guided wave measurements presented in the remainder of this section use a power output level of 100%, for Specimens 4-17-1, 4-17-7 and 4-17-8 where the accumulated axial strain values were 0, 58, and 71% of the strain at failure, respectively, for the 850°C biaxial creep-fatigue test noted earlier (Specimen 4-5-1). Fifteen A-scans were recorded for each of these three specimens after using the following procedure. The transmitter coil was translated from the inner edge of the iron cobalt foil typically less than 5 mm, while the receiver coil was translated from the inner edge of the foil until the primary mode amplitude observed through the oscilloscope was a maximum. One at a time,

each magnet was rotated for the maximum primary mode amplitude.  The A-scan signal was recorded through the oscilloscope. The procedure was repeated until fifteen measurements were obtained for each specimen.

Figure 2.2.2.15 is an example A-scan for Specimen 4-17-1. A fixed length Tukey window (orange frame in Figure 2.2.2.15a) was used to process the T(0,1) wave packet for all measurements. The smaller packet after the framed T(0,1) was produced due to wave interactions with the end of the iron-cobalt foil and specimen. Figure 2.2.2.15b shows the corresponding frequency spectrum for the T(0,1) excitation at 0.83 MHz, with the zoomed in plot between 1-3 MHz to observe the amplitude of the third harmonic. The following colors blue, red, and green correspond to the as-received specimen, 58%, and 71% deformed specimens respectively. The third harmonic amplitude for the 71% deformed specimen is noticeably larger than those of the as-received and 58% deformed specimens.



(a)

(b)
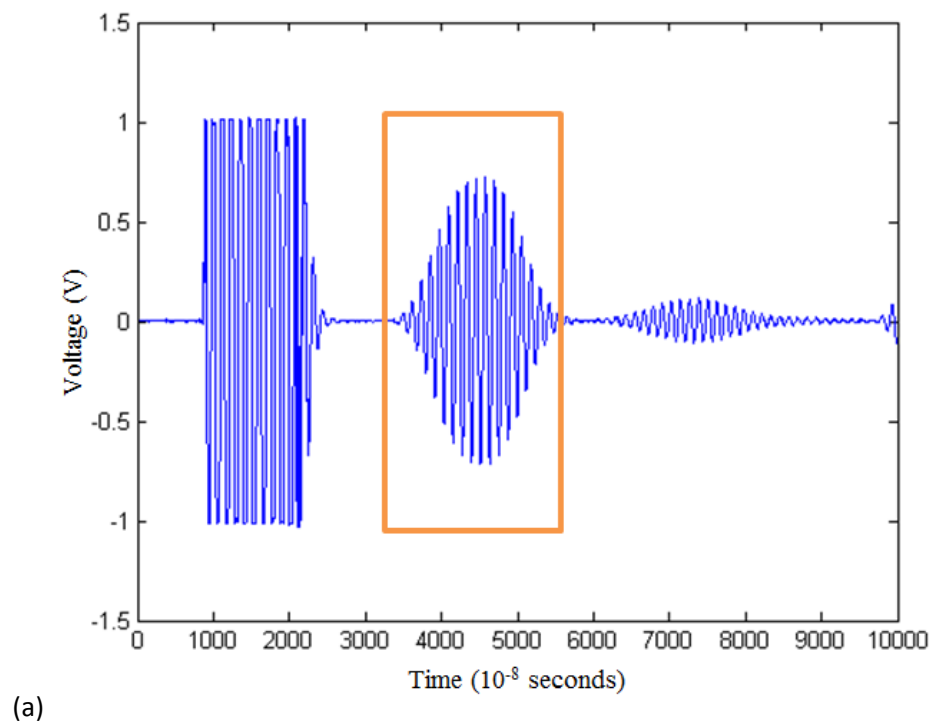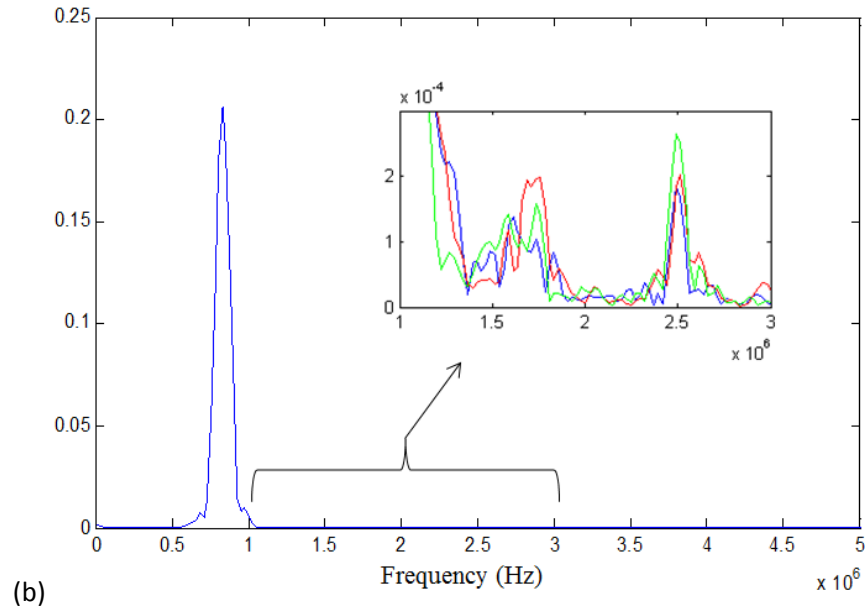
***Figure 2.2.2.15***. *(a) A-scan, (b) frequency spectrum for T(0,1) mode excitation at 0.83 MHz.*

The results shown in Figure 2.2.2.16 are for a 100% output power level. We see that the primary mode T(0,1) amplitude $A_1$ decreases some for samples with increasing damage. Due this change in primary mode amplitude between varying damaged specimens, the modal amplitude ratios trend versus damage % would further magnify the trend of the amplitude of the third harmonic. Yet, it is evident that the amplitude of the third harmonic and modal amplitude ratio is noticeably higher (3.7X) for the 71% damage specimen than that of the as-received specimen. The average modal amplitude ratio is slightly higher for the 58% damaged specimen, but closer to the as-received value than the average of the 71% specimen.
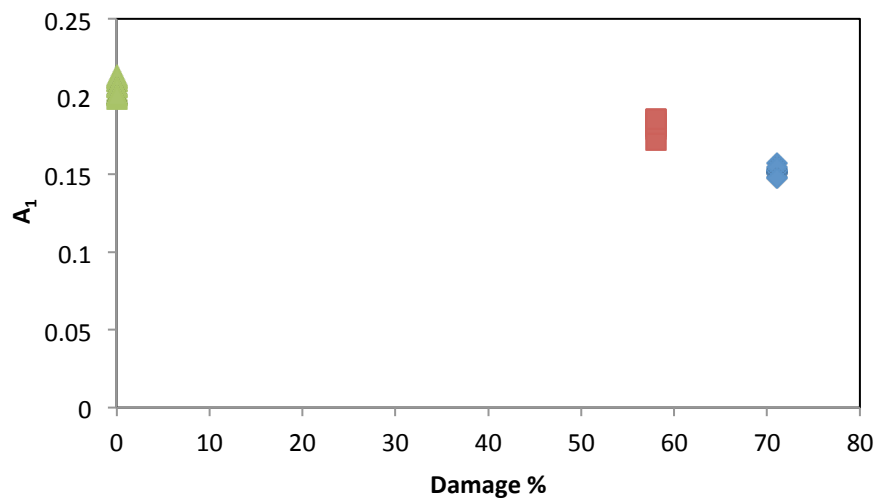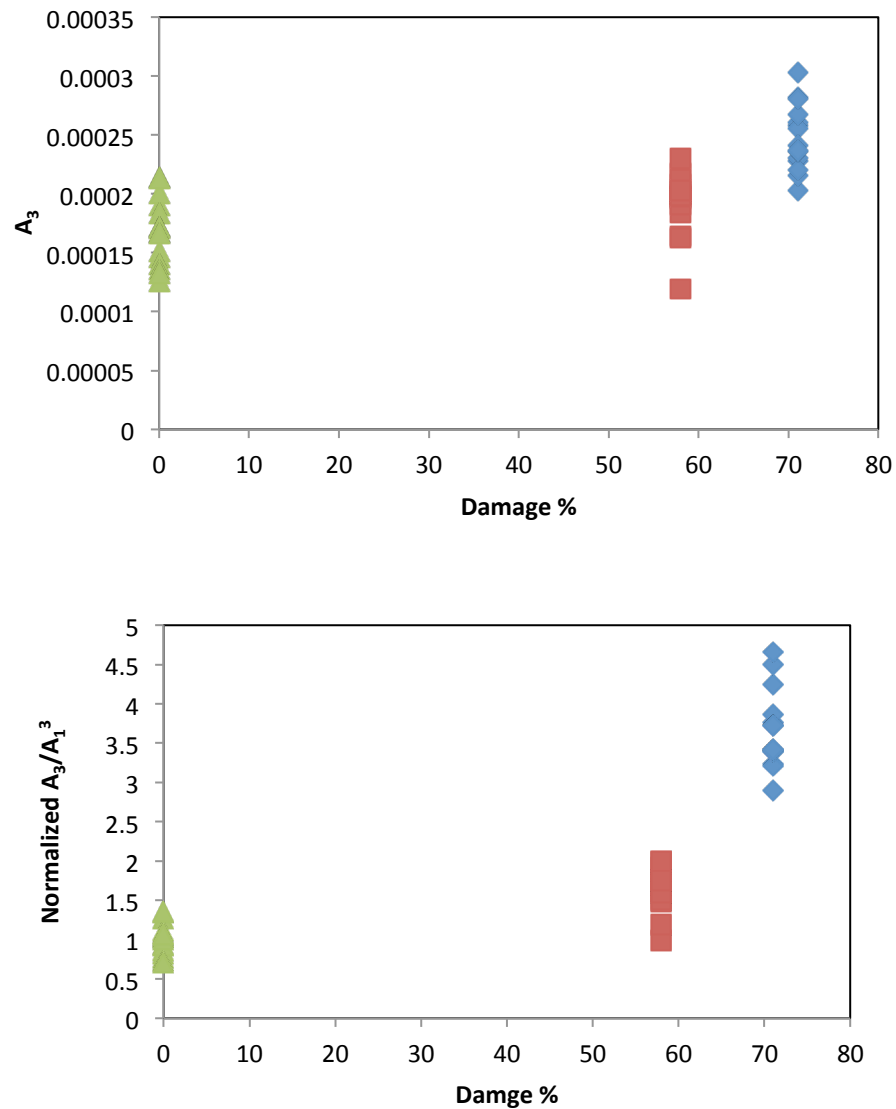
*Figure 2.2.2.16.* (a) Amplitude of primary mode T(0,1), (b) amplitude of third harmonic, (c) normalized modal amplitude ratio (with respect to 0.0194).

We view the results presented in Figure 2.2.2.16 as evidence that the third harmonic of the T(0,1) mode is sensitive to microstructural changes associated with damage. However, there is more research to be done. This work will continue even though the project has ended. We are in the process of refining the experimental procedures to optimize repeatability and reliability. Refinement of the procedure entails multiphysics modeling to optimize the transducer design by more closely examining the overlap of the Fe-Co foil, the meander electric coils, the magnet configuration, and sensitivity to pipe wall thickness variability. Further improvement in the procedure to bond the foil the pipe would also be beneficial.

The same magnetostrictive transducers were used to investigate linear guided wave techniques, i.e., the wave speed of the T(0,1) mode was calculated for the as-received, 58%, and 71% damaged specimens. For each specimen, an A-scan was recorded by a receiver located 89 mm from the transmitter. Subsequent measurements were made with longer propagation distances. The difference in propagation distance was divided by the difference in arrival time of the peak amplitude. The resulting wave speed measurements are shown in Figure 2.2.2.17. The specimens strained to 0% and 78% of failure had very similar wave speeds; while the wave speed for the specimen strained to 58% was slightly lower. Further study is needed to explain these results, as the velocity changes do not have a simple explanation. However, it is worth noting that the wave speed axis is zoomed in on the data and that the 15% difference in wave speed is miniscule compared to the 370% increase in the modal amplitude ratio $A_3/A_1{}^3$.
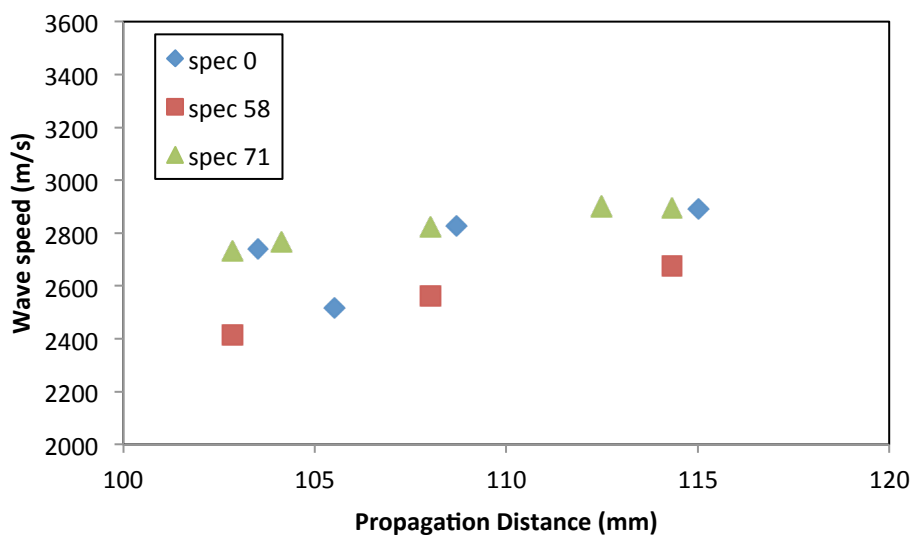


**Figure 2.2.2.17.** *Wave speed measurements of T(0,1).*

### 2.2.2.2 Nonlinear Acoustic Guided Wave Spectroscopy

A provisional patent application entitled "System and method for characterization of materials using nonlinear acoustic guided wave spectroscopy," has been submitted to the U.S. Patent Office by Y. Liu, C.J. Lissenden, G. Choi, X. Yao, J.L. Rose. It was assigned serial number 62/066,650. This section describes the invention.

*Summary*

Nonlinear acoustic guided wave spectroscopy can be used to scan the local material state for the purposes of materials characterization, structural health monitoring, and condition based maintenance. Acoustic guided waves are stress waves in solid media that rely on interactions with boundaries and interfaces to propagate as coherent wave packets. The term nonlinear is used to connotate that the interrogation signal is at a frequency other than the central frequency of the excitation signal. In fact, signals from multiple sources at different positions and activated at different frequencies are mixed together in this method. Spectroscopic analysis of sum and difference frequencies is shown to be very sensitive to the local material state, thus enabling characterization or material state awareness significantly earlier than possible with current state of the art nondestructive systems.

The spectroscopy method for plate-like and shell-like structures involves multiple acoustic transducers, one is a receiver and the others are actuators setup to send stress waves in prescribed directions such that they intersect at a point. The receiver is located to acquire the signal interaction; especially the nonlinear content at frequencies $\pm N_1 f_1 \pm N_2 f_2 \pm \cdots$, where $N_i$ denotes a nonnegative integer such that $N_i \leq N$ and $\sum N_i = N$ and $N$ denotes the order of the harmonic associated with self and mutual interactions. Likewise, $f_i$ denotes the central frequency of actuator $i$. Scanning in 1D or 2D is then achieved by adjusting the intersection point from position to position. The received signal at each intersection point is windowed and transformed to the frequency domain to enable determination of the amplitudes of the harmonics of interest. In this way the entire structure between the actuators, or a subdomain of it, can be scanned.

### *Brief Background and General Purpose*

In many cases once detectable macroscale damage initiates, failure soon follows, leaving little time to implement a maintenance strategy. The detection and subsequent characterization of microstructure evolution that precedes macroscopic damage is absolutely critical to the effort to shift condition-based remaining life prediction to an earlier time in the service life of the structure. This shift of damage detection to the left along the lifetime axis depicted schematically in Figure 2.2.2.18 provides obvious advantages for safety, maintenance actions, logistics, retirement for cause, as well as maximizing availability of the structure and minimizing life cycle costs.
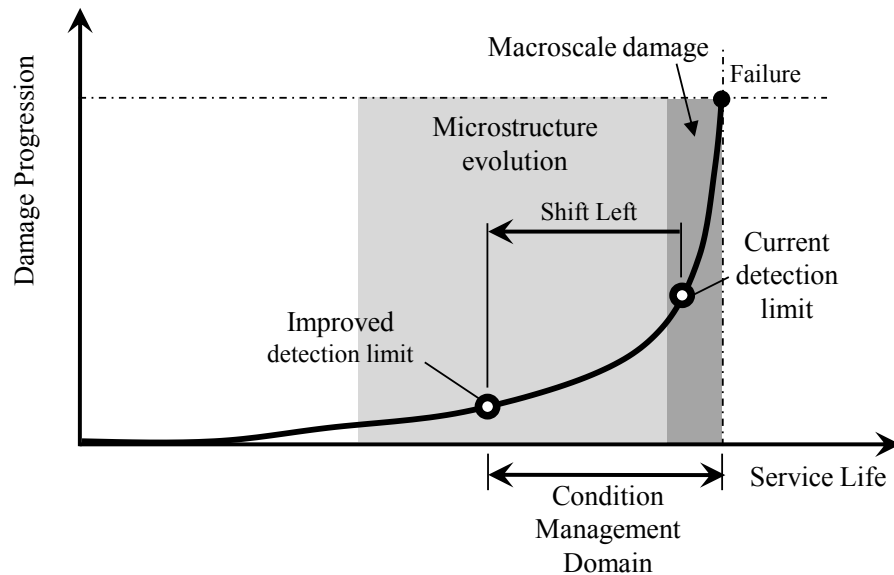
**Figure 2.2.2.18**. *Schematic diagram showing benefit of earlier detection of damage*

Despite the success in nondestructive testing (NDT) and structural health monitoring (SHM) of macro scale defects such as open cracks or large scale corrosion, there are precious few methods capable of in-situ nondestructive characterization of the microstructure. Grain boundary backscatter noise can enable grain size measurement [Turner and Weaver, 1995]. Careful measurement of acoustic emissions can indicate formation of slip bands [Huang et al., 1998]. Likewise, Barkhausen noise in magnetic materials is sensitive to dislocation density and slip band density, but the relationship between Barkhausen noise and the many microstructural parameters is very complex and still under investigation [Sagar et al., 2005 and Kasai et al., 2013]. See also the review of nondestructive characterization techniques by Raj et al. [2003].

Conventional ultrasonics is one of the most powerful tools in the areas of NDT and SHM. Ultrasonic bulk waves are commonly used in regular inspections as they are easy to implement. However, the bulk wave inspection methods are time-consuming and tedious as limited area can be achieved for each inspection. Guided waves are ultrasonic waves traveling in bounded waveguides, such as plates, rods, pipes, and rails. Compared with bulk waves, guided waves can propagate long distances with little energy loss. Thus guided waves are extremely important for the rapid inspection of aircraft, pipelines, pressure vessels, rails, etc. Generally speaking, linear ultrasonics with bulk waves can detect anomalies of the order of a wavelength [Dace et al., 1991]. Ultrasonic guided waves can do significantly better by properly selecting a mode with a wave structure sensitive to the defect [Alleyne and Cawley, 1992].

As a finite amplitude monochromatic wave propagates through a weakly nonlinear material, higher harmonics are generated due to the wave scattering [Jones and Kobett, 1963; Childress and Hambrick, 1964] associated with anomalies in lattice structures and anharmonic interatomic potentials [Cantrell, 2003 and 2004; Cantrell and Yost, 2013]. The second order harmonic generation due to the quadratic

interactions of bulk longitudinal and transverse waves was investigated by Gol'dberg [1960], Jones and Kobett [1963], Childress and Hambrick [1964], Taylor and Rollins [1964], Rollins et al. [1964] and Bender et al. [2012] based on Landau and Lifshitz's [1954] qualitative formulation of anharmonic vibration. Deng [1998 and 1999], de Lima and Hamilton [2003 and 2005], Srivastava and Lanza di Scalea [2009 and 2010], Müller et al. [2010], Liu et al. [2013a, 2013b, 2013c, 2014a, and 2014b] extend the study of nonlinear generation to the mode interactions in waveguides: i.e., plates, rods, and rails, etc.

The generation of measurable higher harmonics is extremely useful because these harmonics are sensitive to the micro-structural features that precede the occurrence of macroscale damage modes. Second and third harmonic generation that is involved with mode self interaction of a wave mode has proven to be sensitive to global material degradations, such as fatigue-generated dislocation substructures [Hikata et al., 1963; Hikata and Elbaum, 1966a and 1966b], persistent slip bands [Cantrell, 2009], thermal aging and creep related precipitates-dislocation interactions [Xiang and Deng, 2008; Xiang et al., 2012], irradiation-induced nanoclusters [Matlack et al., 2012], and localized plastic deformation regions [Lissenden et al., 2014].

Among all the applicable fields of SHM and NDT, e.g., complex civil, aerospace, mechanical, and marine structural systems, failure tends to occur at discontinuities of geometry or composition. The material microstructural evolution exhibits a localized behavior due to high stress concentrations. The SHM/NDT capability for these "localized hot spots" is of significance to ensure the structural integrity. The scanning spectroscopy described in this disclosure can effectively characterize the location and severity of the localized microstructural features.

### *Technical Description of Nonlinear Wave Mechanics*

The following technical description is based on sections 4.3.4 and 5.7 of Yang Liu's thesis entitled, "Characterization of global and localized material degradation in plates and cylinders via nonlinear interaction of ultrasonic guided waves."

### *Full length scanning with nonlinear mode interactions*

The presence of instrumentation nonlinearity is inevitable for the nonlinear measurements associated with wave self interactions (i.e. second harmonic and third harmonic measurements). A successful nonlinear experiment requires the measured material nonlinearity to overwhelm the system nonlinearity. On the other hand, the nonlinear measurements involving the mode mutual interactions are particularly interesting as they occur at frequencies other than integer multiples of the primary excitations, thus they are much less sensitive to system nonlinearity [Croxford et al., 2009]. In this section, we focus on the numerical evaluation of the generation of internally resonant sum and difference harmonic frequencies at quadratic nonlinearity. Furthermore, we propose a full length scanning to characterize the localized material degradation with the mode mutual interaction of guided waves.

The schematic of the full length scanning of material degradation is shown in Figure 2.2.2.19. Two counter-propagating primary waves with different central frequencies ($f_1$ and $f_2$) were generated by two

independent transducers. The primary mode pairs should be selected to generate internally resonant sum or difference harmonics. Time delays were applied in order to enable the waves to mix at arbitrary locations between the two transmitters. A third transducer was used to pick up the sum or difference harmonics at frequencies $f_1+f_2$ and $f_1-f_2$. The localized material degradations can be identified by the sum or difference harmonics due to the interaction of two primary waves when compared to the baseline measurement obtained before the introduction of localized material microstructural evaluation.
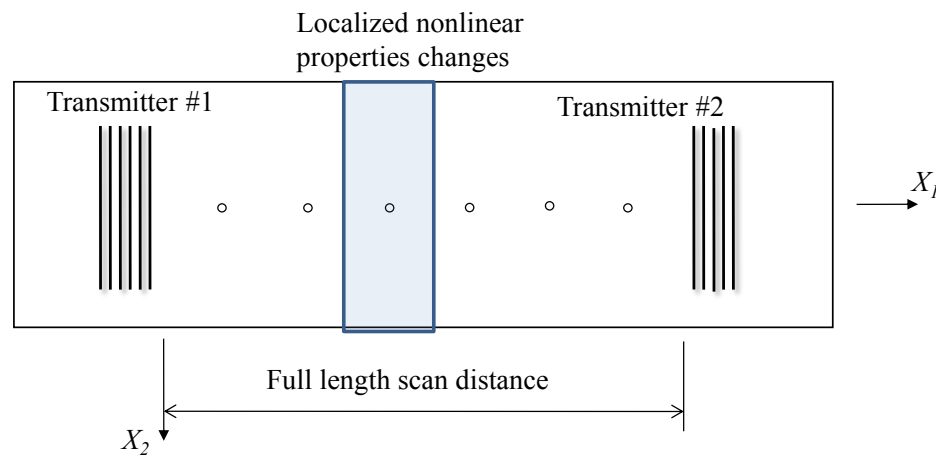


**Figure 2.2.2.19.** *Schematic for the method of full length scanning by primary mode mutual interaction. The circles represents for mode interaction positions.*

Table 2.2.2.5 presents some primary interacting mode pairs that generate internally resonant sum or difference harmonics. These secondary modes receive non-zero power flux from the corresponding primary mutual interactions. The synchronism condition is also met as indicated in the table. Numerical evaluations were conducted in a 2D aluminum plate for mode pair 1 (primary A0 and S1 generating sum harmonic A1) and mode pair 2 (primary A0 and S1 resulting in internal resonant A2) in Table 2.2.2.5.

**Table 2.2.2.5.** *Example internal resonant mode pairs that generate internal resonant A1 sum or difference harmonics at quadratic interactions.*

| Mode pair | Wave field | | Frequency (MHz) | $C_p$ (mm/μs) | Wavelength (mm) | Wavenumber |
|---|---|---|---|---|---|---|
| 1 | Primary modes | A0 | 0.58 | 2.429 | 4.1879 | 1.51 |
| | | S1 | 1.60 | 6.708 | 4.1925 | 1.49 |
| | Sum harmonics | A1 | 2.18 | 4.5612 | 2.09229 | 3.00 |
| 2 | Primary modes | A0 | 3.76 | 2.9328 | 0.78 | 8.05 |
| | | S1 | 2.40 | 5.709 | 2.3785 | 2.63 |
| | Sum harmonics | A2 | 6.16 | 3.6212 | 0.588 | 10.68 |
| 3 | Primary modes | SH2 | 1.78 | 6.30 | 3.54 | 1.77 |
| | | SH4 | 3.56 | 6.30 | 1.77 | 3.55 |
| | Diff harmonics | S1 | 1.78 | 6.30 | 3.54 | 1.77 |
| 4 | Primary modes | SH1 | 1.08 | 4.45 | 4.12 | 1.52 |
| | | SH3 | 3.03 | 4.84 | 1.60 | 3.93 |
| | Diff harmonics | S1 | 1.95 | 5.06 | 2.60 | 2.41 |
| 5 | Primary modes | SH0 | 0.60 | 3.11 | 5.18 | 1.21 |
| | | S0 | 1.80 | 3.11 | 1.72 | 3.65 |
| | Diff harmonics | SH0 | 1.20 | 3.11 | 2.59 | 2.43 |
| 6 | Primary modes | SH1 | 1.20 | 4.06 | 3.38 | 1.86 |
| | | S2 | 3.71 | 6.18 | 1.67 | 3.76 |
| | Diff harmonics | SH3 | 2.51 | 8.23 | 3.28 | 1.90 |
| 7 | Primary modes | S1 | 1.78 | 6.30 | 3.54 | 1.77 |
| | | S2 | 3.56 | 6.30 | 1.77 | 3.54 |
| | Sum harmonics | S3 | 5.34 | 6.30 | 1.18 | 5.32 |
| 8 | Primary modes | A0 | 0.61 | 2.47 | 4.05 | 1.55 |
| | | A1 | 1.80 | 5.39 | 3.00 | 2.10 |
| | Sum harmonics | A1 | 2.41 | 4.14 | 1.72 | 3.65 |

*Case 1: Primary A0 and S1 mutual interaction results in sum harmonic A1*

Two independent inter digital transducers (IDT) are modeled to generate the primary A0 mode and S1 modes. The A0 mode ($f_1$=0.58 MHz) was generated by a 6-element IDT with a 15-cycle tone burst surface traction applied in the out-plane $X_3$ direction, while a 30-cycle tone burst surface traction was exerted in

the in-plane $X_1$ direction for the excitation of the primary S1 mode ($f_1$=1.60 MHz). The simulations are conducted on homogeneous and localized degraded plates, respectively. The homogeneous plates are modeled with material parameter Set 1 and treated as a baseline. The localized material degradation region of length 0.1$R$ was represented by increasing the third order elastic constants twice while keeping the linear elastic constants unchanged (Set 2). The material outside of the localization domain is described by material parameter Set 1. The center of material degradation region was arranged 0.7R to the A0 transmitter while 0.3R to S1 transmitter. Time delay was applied to the two transmitters to enable the primary A0 and S1 mode interaction at arbitrary points between the two transmitters.

Figure 2.2.2.10 shows the primary A0 and S1 signals before interaction. It is observed that good excitations are obtained for both primary modes. The frequency spectra for the primary A0 and S1 modes are shown in Figure 2.2.2.20 (b) and (d). The magnified spectra indicate that no harmonic component exists at the sum frequency before the two mode mixing. Figure 2.2.2.21 shows the signals when the two waves mix at the center of the material degradation region. The red solid lines and the black dashed lines represent the signals obtained from the homogeneous and  localized degraded plates, respectively. A time domain window with a fixed length is applied to extract the mixed wave packets for FFT and the frequency spectra are as shown in Figure 2.2.2.21 (b). The sum harmonic A1 mode ($f_1$+$f_2$=2.16 MHz) is observed for both homogeneous and localized material degraded plates. Figure 2.2.2.21 indicates that the A-scan and the primary harmonics are insensitive to localized material degradations, while the generation of sum harmonics is very sensitive to the change of material third order elastic constants.
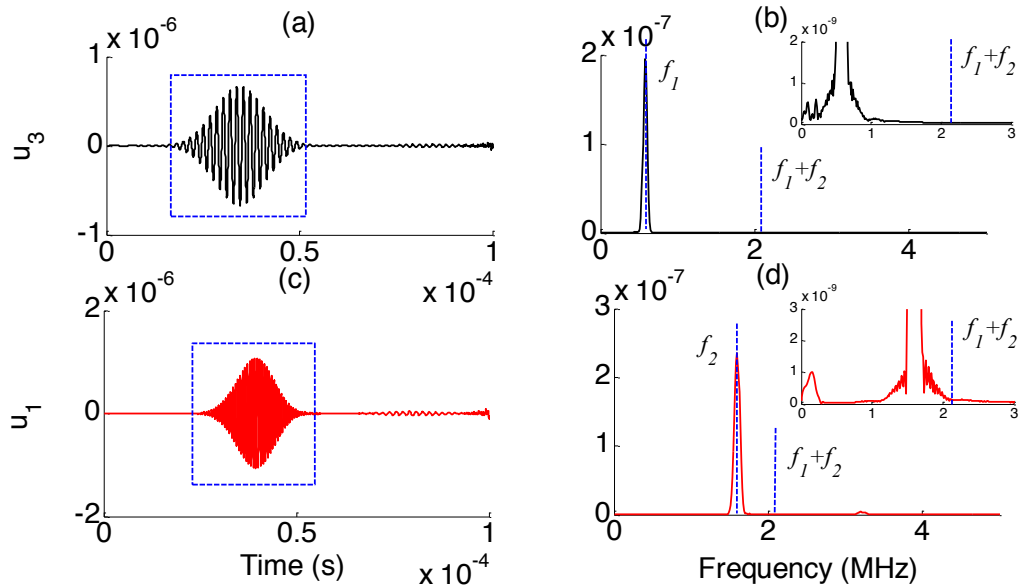


*Figure 2.2.2.20. The primary A0 at 0.58 MHz and S1 at 1.60 MHz before interaction. (a) Time domain signal of A0 mode, (b) the FFT results for the first receiving signal as indicated by the blue rectangle. (c) Time domain signal for S1 mode, (d) the corresponding frequency spectra.*
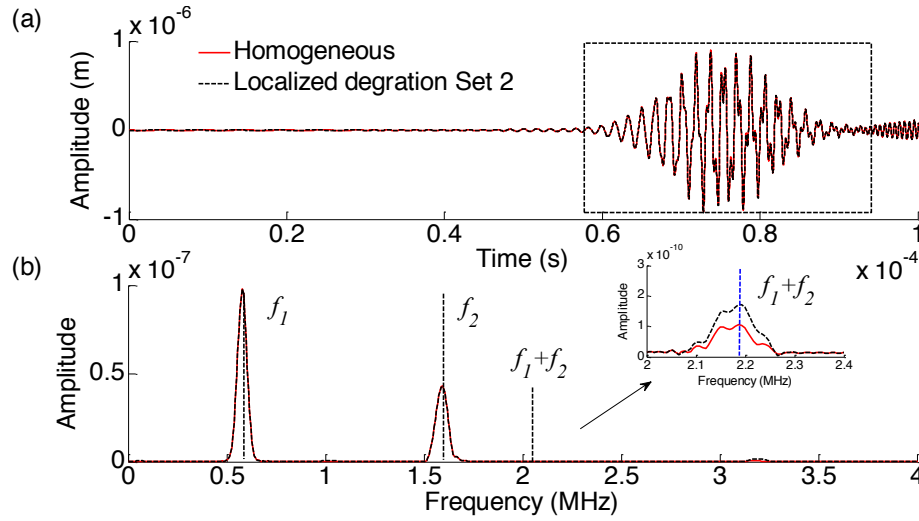
**Figure 2.2.2.21.** *Signals for primary A0 and S1 mutual interaction generating internal resonant A1 mode for material parameters Set 1 and Set 3, (a) time domain signal for the mixing signal, and (b) the corresponding frequency spectra.*

Appropriate time delays are applied on the two transmitters independently to ensure that the two primary waves interact at seven different positions. The sum harmonics generated at each interaction site were extracted for localized degraded plates, for which the amplitude is denoted as $A_{sum\_D}$. These values were compared with the sum harmonic generations within the homogeneous plate, denoted as $A_{sum\_H}$. The sum harmonic increment ratio is defined as

$$\varepsilon = \frac{A_{sum\_D} - A_{sum\_H}}{A_{sum\_H}}. \tag{1}$$

Figure 2.2.2.22 shows the sum harmonic increment ratio versus primary interaction positions, which successfully identified the localized material degradation. The sum harmonic generation due to the mutual interaction at the center of localized material degradation region increased by 65% (for Set 2), while the variation of sum harmonic is less than 1% out of the degradation region. A full length scanning of the plates microstructure evolution was successfully conducted by the sum harmonics due to primary A0 and S1 mutual interaction.

**Figure 2.2.2.22.** *Sum harmonic incremental ratio for primary A0 and S1 mutual interaction generating internal resonant A1 mode. The scanning successfully identified localized material degradation.*

*Case 2: Primary A0 and S1 mutual interaction results in sum harmonic A2*

In this section, we present the results of full length scanning using primary A0 ($f_1$=3.76 MHz) and S1 ($f_2$=2.40 MHz) interaction that generates internal resonant A2 mode ($f_1 + f_2$=6.16 MHz). The simulations are conducted on two types of aluminum plates: a homogeneous plate with material parameters given by Set 1, and another plate with localized material degradation which is modeled by material Set 3. The localized material degradation region was arranged at the middle of the two transmitters.

Figure 2.2.2.23 presents the signals obtained for primary A0 and S1 excitation before the two waves mixing. Good mode excitation was obtained for both A0 and S1 waves. Time domain windows with fixed window length (indicated by the blue dashed rectangles) were applied to extract the first received wave packet for the FFT, the corresponding frequency spectra were shown in Figure 2.2.2.23 (b) and (d). The magnified frequency spectra indicate that no sum harmonic component is present before the wave interaction. Time delays are applied to the two transmitters which enables the two primary waves to interact at an arbitrary point within the propagation distance. Figure 2.2.2.24 shows the signals obtained when the primary modes interact at the center of the localized degradation region, which indicates that the A-scan and the primary frequency components are insensitive to localized material degradation. Figure 2.2.2.24 (b) also indicates that the sum harmonic is very sensitive to the localized material degradation. A full length sum harmonic scan was conducted by adjusting the time delays that enable the primary waves interacting at ten different locations. Figure 2.2.2.25 (a) presents the amplitude of the sum harmonics in the homogeneous and the localized degraded plates, respectively, which indicates that the sum harmonic generation within the localized degraded region changes dramatically, while minimal variation is observed in other locations. The sum harmonic increment plot given by Figure 2.2.2.25 (b) successfully identified the localized material degradation regions.
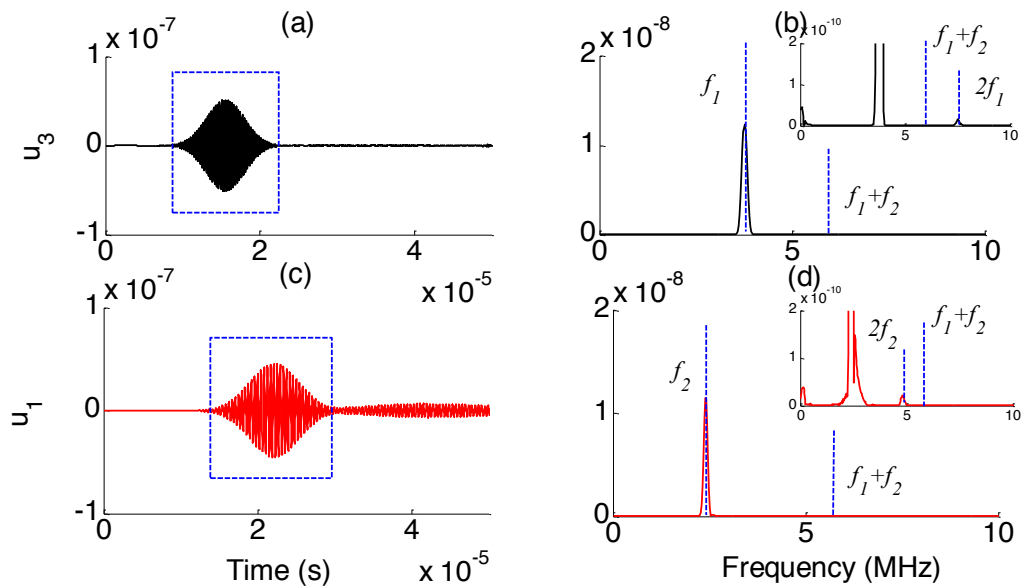
**Figure 2.2.2.23.** *The primary A0 at 3.76 MHz and S1 at 2.40 MHz before interaction (a) Time domain signal of A0 mode, (b) the FFT results for the first receiving signal as indicated by the blue rectangle. (c) Time domain signal for S1 mode, (d) the corresponding frequency spectra.*
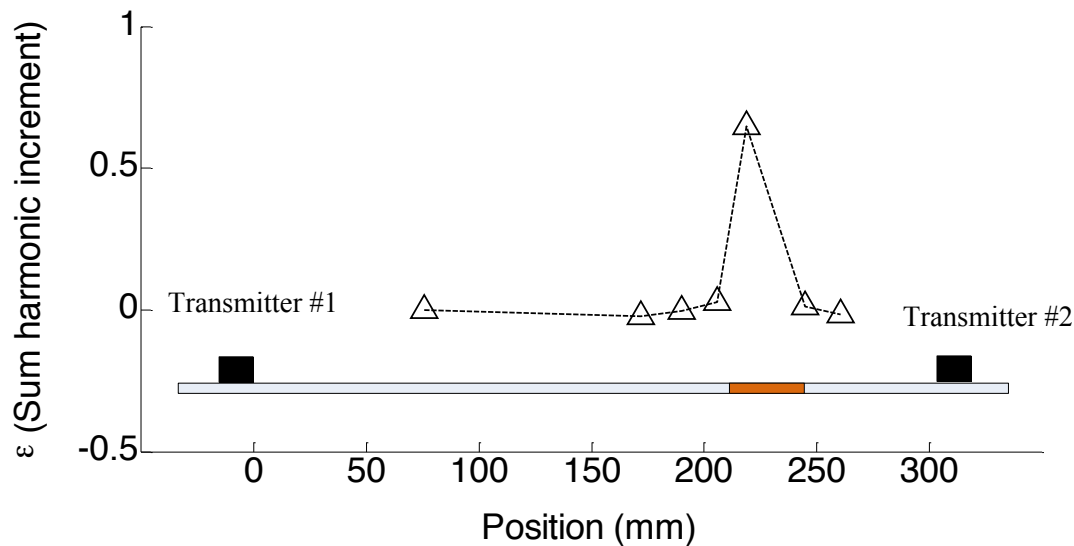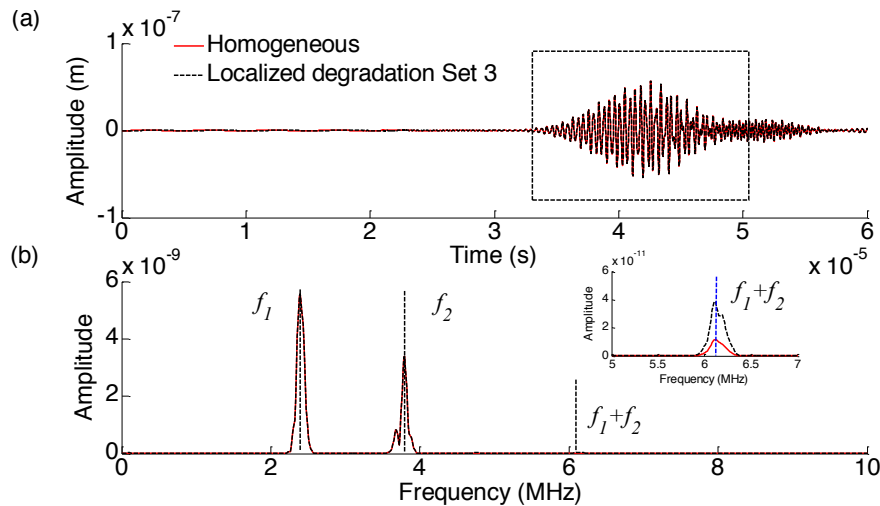


**Figure 2.2.2.24.** *Signals for primary A0 and S1 mutual interaction generating internal resonant A2 modes for material parameters Set 1 and Set 3, (a) time domain signal for the mixing signal, and (b) the corresponding frequency spectra. The figure shows the signal when the two primary waves interacting at the center of the material degradation region.*

(a)



(b)
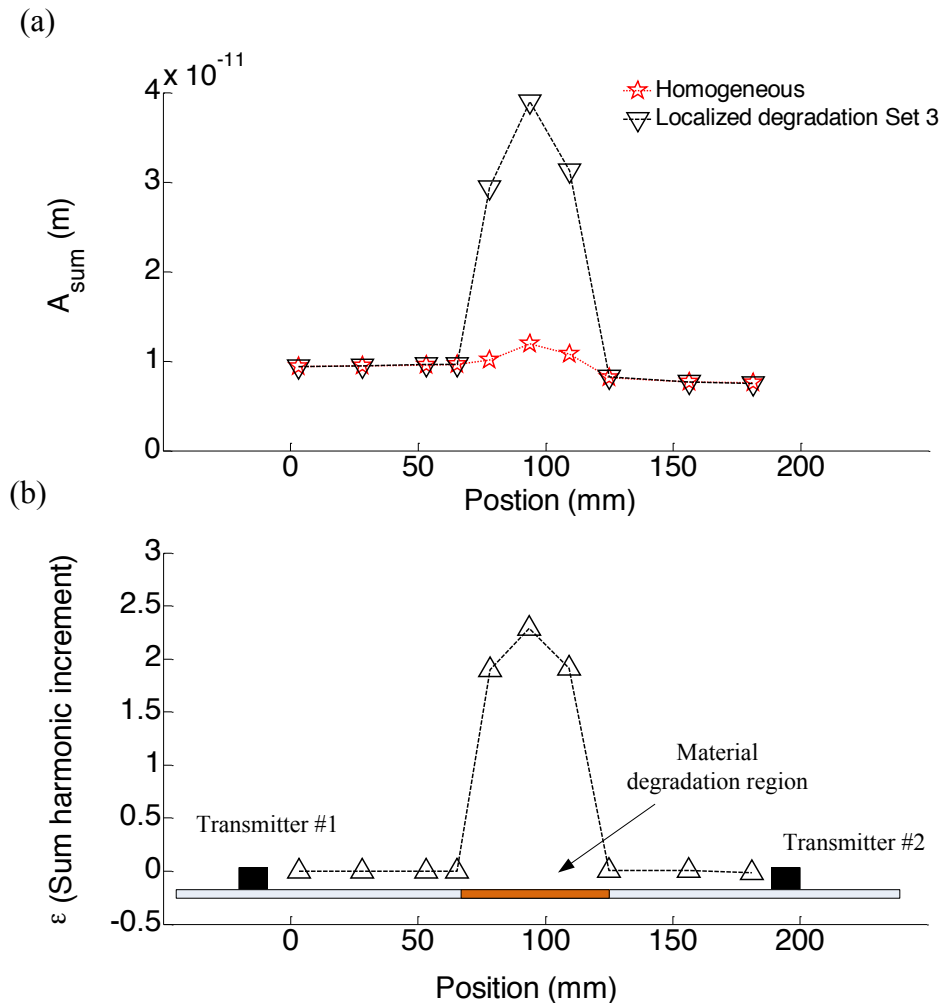


*Figure 2.2.2.25. The scanning results for A0 and S1 mutual interaction results A2 mode as internal resonant sum harmonic, (a) sum harmonic amplitude for the baseline (red dashed line) and localized degraded (black dashed line) plate, (b) Sum harmonic incremental ratio.*

*Tomo-scanning of localized material degradation in pipes by mode interactions*

Cylindrical waveguides such as pipelines, pressure vessels, and heat exchangers are widely used in many industries for the transportation and storage of gas, oil, chemicals and other products. Material degradation exhibits a localized behavior as high stress concentration happens in the discontinuity of geometry or composition in these structures. Therefore, techniques that are capable to characterize the localized material degradation in cylinders are highly demanded. Similarly to the full length scanning technique just described, the nonlinear interaction of two guided waves are used to construct a tomogram of the localized material degradation in cylinders.

The schematic methodology of the nonlinear tomo-scanning of material degradation is illustrated in Figure 2.2.2.26. Two counter propagating guided wave modes are excited with two independent transmitters. The primary wave modes should be selected according to the analysis to generate

internally resonant sum or difference harmonics. Precise time delays can be applied to the transmitters and enable the waves to interact at all axial distance of interest. The circumference is covered by 360 degrees as the flexural wave fields distributed all around the pipe. Multi-channel receivers are distributed around the perimeter in the vicinity of localized material degradatioin to detect the sum and difference harmonics due to the nonlinear interaction of the two primary waves. Comparison with the baseline measurement obtained in the health condition allows the tomogram to identify the localized material degradation zones.
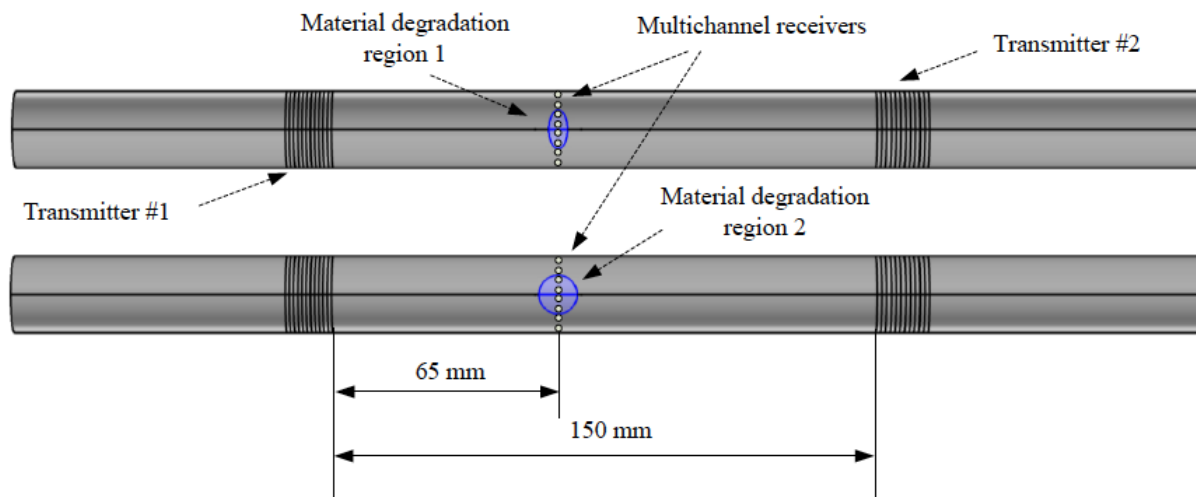


**Figure 2.2.2.26.** *Schematic illustration of the nonlinear tomo-scanning conception. Two localized material degradation regions are introduced into the pipe. The material degradation is represent by increasing the third order elastic constants while keeping the linear elastic properties unchanged.*

A steel pipe is modeled for the illustrative purpose. Two localized material degradation regions are introduced into the pipe as shown in Figure 2.2.2.26. The material degradation 1 is a through-thickness elliptical region with third order elastic constants increased by 100%, while the material degradation 2 is a through-thickness circular region with third order elastic constants increased by 200%. According to the analysis in the previous sections in this chapter, the primary $T(0,1)$ mode ($f_1$=0.7 MHz) and $L(0,2)$ mode ($f_2$=1 MHz) mutual interaction (mode pair 7) that results in internal resonant $T(0,2)$ mode ($f$= $f_1$+$f_2$=1.7 MHz) is selected to construct the nonlinear tomogram. The $T(0,1)$ and $L(0,2)$ modes are generated with parametric inter digital transducers and the signals are acquired with a circular point array as indicated in Figure 2.2.2.26.

The mutual interaction of axisymmetric torsional and longitudinal modes can result in internally resonant sum or difference harmonics of torsional nature. Therefore the analysis focuses on the circumferential components ($u_\Theta$) of the displacement field. Figure 2.2.2.27 shows the signals obtained from the channel where the two primary waves interact at the center of the material degradation region 1; while Figure 2.2.2.28 displays the results where the waves mix at the material degradation region 2.

Figures 2.2.2.27 and 2.2.2.28 imply that the changes of the linear characteristics of the signal are minimal, thus are insensitive to this type of material degradation. In contrast, the magnified frequency spectra show that the sum harmonics increase by 75% for the wave mixing in material degradation 1 and 172% for that in material degradation region 2. Time delays are applied on the two transmitters independently to enable the primary waves to interact at axial distance from 11 mm to 113 mm in increments of 3 mm. The signals are collected by a point array that covers the entire circumference. The sum harmonic due to the primary mode interaction is extracted through a FFT with the same window type and length. Figure 2.2.2.29 shows the nonlinear tomogram which displays the sum harmonic incremental ratio. The result indicates that the nonlinear tomo-scanning is capable to fully characterize localized material degradation in cylinders, i.e. (i) axial and circumferential locations, and (ii) severity of the material degradation.
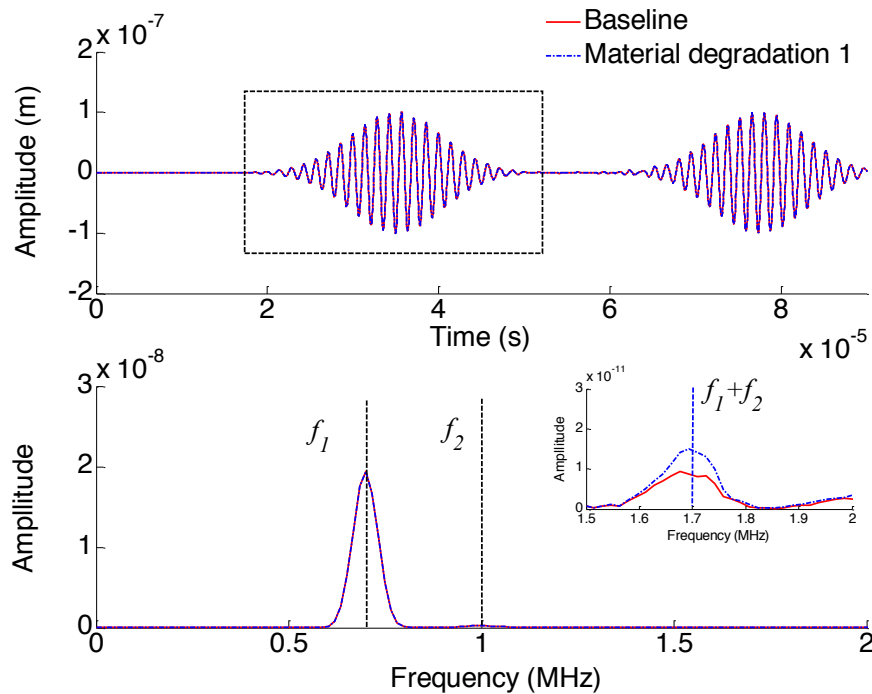


*Figure 2.2.2.27.* Signals for primary T(0,1) and L(0,2) mutual interaction. The signals are obtained through a point source where the two primary modes mixing in material degradation region 1.
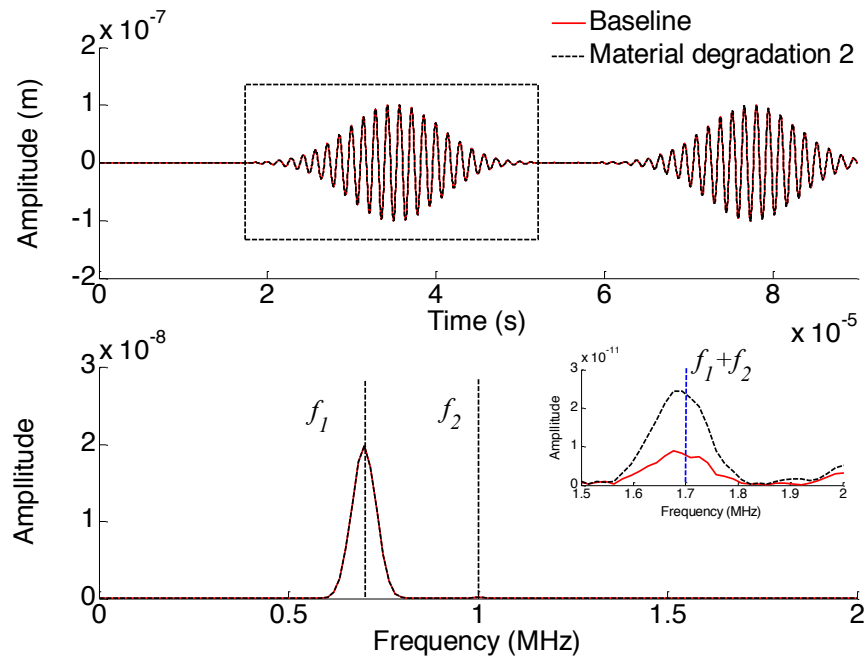
**Figure 2.2.2.28.** *Signals for primary T(0,1) and L(0,2) mutual interaction. The signals are obtained through the channels where the two primary modes mixing in material degradation region 2.*
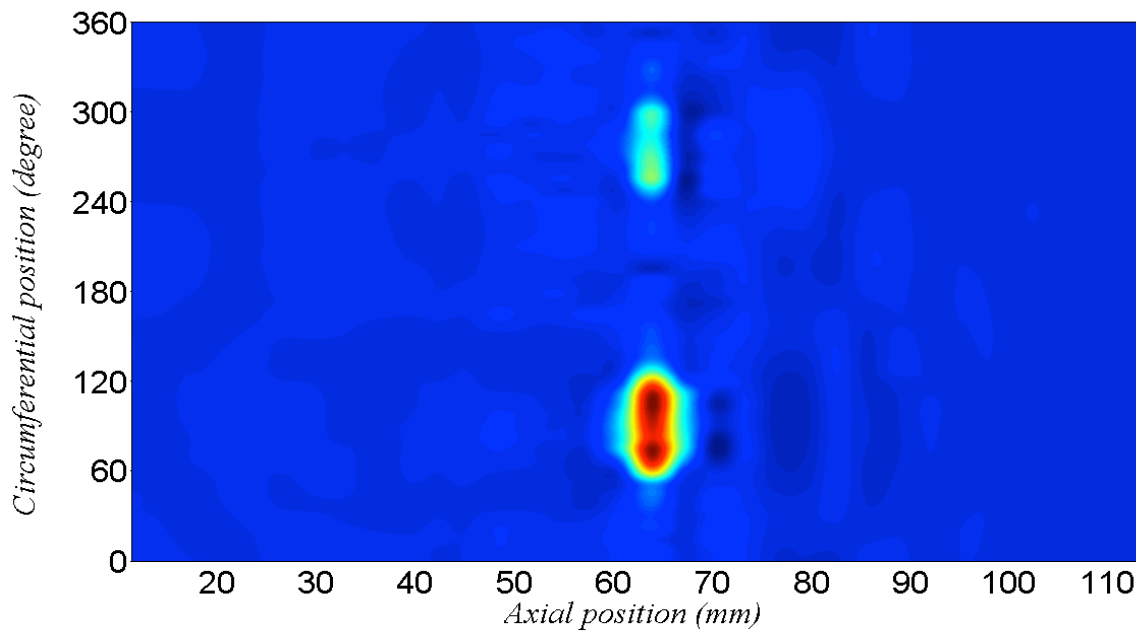


**Figure 2.2.2.29.** *Tomogram of localized material degradation regions by the mode mutual interaction of two guided wave modes in a steel pipe.*

97

*Advantages and Improvements*

The primary advantage is that nonlinear acoustic guided wave spectroscopy is sensitive to features of the microstructure of materials. The evolution of these microstructural features precedes the development of macroscale damage. Thus nonlinear acoustic guided wave spectroscopy can provide a very early indication of material degradation, which cannot be seen by eye or detected with conventional nondestructive evaluation methods such as dye penetrant, ultrasonics, or eddy currents. One improvement is that it enables the prediction of remaining useful life at a much earlier point in the service life of the structural system, which in turn enables a paradigm shift from schedule based maintenance to condition based maintenance. Another improvement is due to its ability to nondestructively characterize materials; e.g., porosity estimation in rock formations.

*References*

Alleyne DN, Cawley P (1992) The interaction of lamb waves with defects. IEEE Trans Ultrasonic, Ferroelectrics and Frequency Control, 39(3):381–387.

Cantrell JH (2004) Substructural organization, dislocation plasticity and harmonic generation in cyclically stressed wavy slip metals. Proc R Soc London A460:757-780.

Cantrell JH (2009) Nonlinear dislocation dynamics at ultrasonic frequencies. J Appl Phys 106:043520.

Cantrell JH and Yost WT (2013) J. Appl. Phys. 113:153506.

Childress JD, Hambrick CG (1964) Interactions between elastic waves and an isotropic solid. Phys Rev 136:411-418.

Dace GE, Thompson RB, Brasche LJH, Rehbein DK, Buck O (1991) Nonlinear acoustics, a technique to detect micrsostructural changes in materials," Rev Prog Quant Nondestr Eval 10B:1685-1692.

de Lima, WJN, Hamilton MF (2003) "Finite-amplitude waves in isotropic elastic plates. J Sound Vibration 265:819-839.

de Lima, WJN, Hamilton MF (2005) "Finite amplitude waves in isotropic elastic waveguides with arbitrary constant cross-sectional area. Wave Motion 41:1-11.

Deng M (1998) Cumulative second-harmonic generation accompanying nonlinear shear horizontal mode propagation in a solid plate. J Appl Phys 84:3500-3505.

Deng M (1999) Cumulative second-harmonic generation of Lamb-mode propagation in a solid plate. J Appl Phys 85:3051-3058.

Gol'dberg ZA (1960) Interaction of plane longitudinal and transverse elastic waves. Sov Phys Acoust 6:307-310.

Hikata A, Chick BB, and Elbaum C (1963) Appl Phys Lett 3:195.

Hikata A, Elbaum C (1966) Generation of ultrasonic second and third harmonics due to dislocations. I. Phys Rev 144(2):469-477.

Hikata A, Elbaum C (1966) Generation of ultrasonic second and third harmonics due to dislocations. II. Phys Rev 151(2):442-449.

Huang M, Jiang L, Liaw PK, Brooks CR, Seeley R, Klarstrom DL (1998) Using acoustic emission in fatigue and fracture materials research. JOM-e 50(11).

Jones GL, Kobett DR (1963) Interaction of elastic waves in an isotropic solid. J Acoust Soc Am 35:5-10.

Kasai N, Koshino H, Sekine K, Kihira H, Takahashi M (2013) Study on the effect of elastic stress and microstructure of low carbon steels on Barkhausen noise. J Nondestruct Eval 32:277-285.

Landau LD, Lifshitz EM (1954) Mechanics of Continuous Media. GITTL, Moscow.

Lissenden CJ, Liu Y, Choi GW, Yao X (2014) Effect of localized microstructure evolution on higher harmonic generation of guided waves," J Nondestruct Eval 33(2):178-186.

Liu Y, Chillara VK, Lissenden CJ (2013a) On selection of primary modes for generation of strong internally resonant second harmonics in plate. J Sound Vib 332(19):4517-4528.

Liu Y, Khajeh E, Lissenden CJ, Rose JL (2013b) Interaction of torsional and longitudinal guided waves in weakly nonlinear circular cylinders. J Acoustic Soc Am 133(5):2541-2553.

Liu Y, Lissenden CJ, Rose JL (2013c) Cumulative second harmonics in weakly nonlinear plates and shells. In: Kundu T (ed) Health Monitoring of Structural and Biological Systems, Proceedings of SPIE, Vol. 8695, paper 869528.

Liu Y, Lissenden CJ, Rose JL, 2014a, "Higher order interaction of elastic waves in weakly nonlinear circular cylinders. I. analytical foundation," *J. Appl. Phys*. Vol. 115:214901.

Liu Y, Khajeh E, Lissenden CJ, Rose JL, 2014b, "Interaction of elastic waves in weakly nonlinear circular cylinders. II. physical interpretation and numerical simulation," *J. Appl. Phys*. Vol. 115:214902.

Matlack KH, Wall JJ, Kim JY, Qu J, Jacobs LJ, Viehrig HW (2012) Evaluation of radiation damage using nonlinear ultrasound," J Appl Phys 111:054911.

Müller MF, Kim JY, Qu J, Jacobs LJ (2010) Characteristics of second harmonic generation of Lamb waves in nonlinear elastic plates. J Acoust Soc Am 127(4):2141-2152.

Raj B, Moorthy T, Jayakumar T, Bhano Sankara Rao K (2003) Assessment of microstructures and mechanical behavior of metallic materials through non-destructive evaluation. Int Matls Rev 48:273-325.

Rollins FR, Taylor LH, Todd PH (1964) Ultrasonic study of three-phonon interactions. II. experimental results. Phys Rev 136:597-601.

Sagar SP, Parida N, Das S  Dobmann G, Bhattacharya DK (2005) Barkhausen emission to evaluate fatigue damage in a low carbon structural steel. Int J Fatigue 27:317-322.

Srivastava A, Lanza di Scalea F (2009) On the existence of antisymmetric or symmetric Lamb waves at nonlinear higher harmonics. J Sound Vibration 323:932-943.

Srivastava A, Bartoli I, Lanza di Scalea F (2010) Higher harmonic generation in nonlinear waveguides of arbitrary cross-section. J Acoust Soc Am 127:2790-2796.

Taylor LH, Rollins FR, (1964) Ultrasonic study of three-phonon interactions. I. theory. Phys Rev 136:591-596.

Turner JA, Weaver RL (1995) Time dependence of multiply scattered diffuse ultrasound in polycrystalline media. J Acoust Soc Am 97(5):2639-2644.

Xiang Y, Deng M, Xuan F, Liu C (2012) J Appl Phys 111:104905.

**2.3 Microstructural Evaluation**

Alloy 617 samples were viewed via optical microscopy, scanning electron microscopy, and transmission electron microscopy. The samples were extracted from specimens that were: as-received, thermally aged, crept in tension, fatigued with uniaxial loading, and subjected to cyclic biaxial loading. This section is organized based upon the type of microscopy.

*2.3.1 Optical Microscopy*

This section is adapted from the undergraduate honors thesis of Brett Corl.

*Sample Preparation*

The experimentation portion of this work was included in developing a sample preparation technique in order to prepare tested samples for optical microscopy. This includes removing a small portion of the tested samples then mounting it in a fast-curing resin. Once mounted, the samples must undergo grinding, polishing and etching to remove all surface debris and scratches, yielding a mirror-like surface capable of being viewed at high magnification and resolution within the optical microscope. The two most challenging portions of the sample preparation process were polishing and etching, which took multiple attempts to discover how to obtain the best results.

*Sample Cutting*

The process begins with a saw specially designed for sample preparation purposes to remove a small portion of tested samples to be observed with the optical microscope. Also, when using the saw, specific blades and machine settings must be used depending on the sample material. All equipment and materials used for the entirety of the sample preparation are purchased from Struers. Saw machinery being used is an Accutom-5 cut-off saw, with a silicon carbide cut-off wheel. The speed of the cut-off wheel during sample cutting is 3000 rpm, with a feed of 0.015 mm/s. Through the duration of cutting, water is applied to the blade in order to maintain low temperature of the blade and limit the opportunity for failure. Figure 2.3.1.1 is a photograph of the saw. The sample is placed in a holder underneath the plastic hood to protect the operator from any projected fragments.

***Figure 2.3.1.1.*** *Struers Accutom-5 sample cut-off saw*

*Sample Mounting*

Once the sample has been cut from the tested specimen, it must be mounted in a fast-curing resin, allowing the sample to be ground, polished, etc. without having to touch the surface to be examined, which could potentially jeopardize the final results.  The mechanism used to mount the samples is a ProntoPress-20 as seen in Figure 2.3.1.2, which melts the powdery resin material, then cures it by rapid cooling.



***Figure 2.3.1.2.*** *Struers ProntoPress-20 sample mounting machine*

Resin used for mounting samples of Alloy 617 is Isofast, which is a diallyl phthalate hot mounting resin with glass fibers in it.  The complete mounting process takes 11 min., 7 of which are for heating at 180°C, the other 4 are for high-rate cooling.  The final result of sample mounting is the formation of a green puck made of the cured resin, with the mounted sample visible within the puck's cross-section as within the examples in Figure 2.3.1.3.
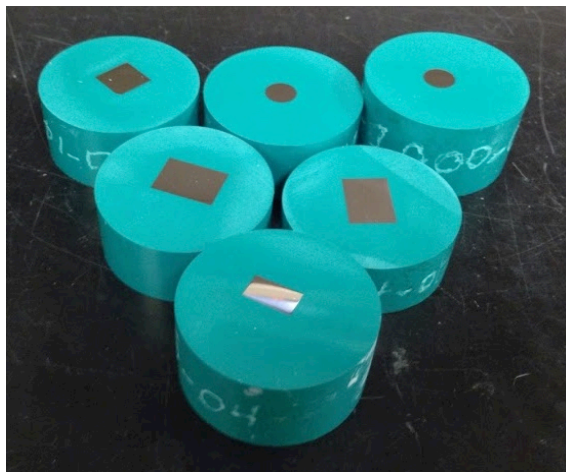


*Figure 2.3.1.3.* *Several mounted samples of Alloy 617*

*Sample Grinding*

Upon completion of the mounting phase, the mounted sample must undergo grinding in order to remove debris from cutting and mounting, as well as large surface scratches, which are often visible to the naked eye.  Grinding takes place on a RotoPol-22 grinding and polishing machine, which is shown in Figure 2.3.1.4.

***Figure 2.3.1.4**. Struers RotoPol-22*

As with the cut-off wheel, grinding is done using silicon carbide paper pads.  Also, water is continuously applied to the silicon carbide for two reasons.  First, the water keeps both the silicon carbide and sample cool in order to avoid damage to sample.  Second, the water removes debris on the silicon carbide papers, as the sample is grinded.  This debris mainly consists of large pieces of the sample that are removed, for example, edges produced during cutting.  The water facilitates removal of this debris by causing it to proceed off the edge of the pad as it spins at a speed of 150 rotations per minute.  There are five cycles of grinding each sample must undergo.  These include using silicon carbide papers numbered 180, 220, 320, 1200, and 2400 in that order.  Silicon carbide paper number 180 has the coarsest grit, while 2400 has the finest.  In order to proceed to finer grit silicon carbide paper, the surface is examined under a simple microscope at ten times magnification to ensure there are no large surface scratches.  Once this is confirmed, the next silicon carbide paper in the sequence is used for grinding until the 2400 paper has been applied, which then completes the grinding phase.  Notably, for grinding, no sample holder is used.  Each sample is held by hand, and is stabilized on the spinning silicon carbide paper by applying a small, immeasurable amount of force vertically on the sample.

*Sample Polishing*

Following sample grinding is sample polishing.  Each sample undergoes three rounds of polishing, two of which are using the same polishing materials.  The machine used for polishing is the same used for grinding.  However, for polishing, a mechanical sample holder is used which, in addition to the spinning polishing pad, also spins and applies a user-specified amount of force to the sample being polished.  Figure 2.3.1.5 shows a sample undergoing the process of polishing.  It is worth noting that for polishing, only one sample is prepared at a time.

**Figure 2.3.1.5**. Alloy 617 sample being polished

The polishing portion of sample preparation must be completed in the manner that best removes all residues, scratches and other flaws on the surface that have been created during other stages of sample preparation.  If not done properly, significant surface flaws such as residues or scratches will remain, resulting in tainted images from the optical microscopy.  Figure 2.3.1.6 presents a sample that has not been properly polished, and shows the existence of substantial surface scratches that must be removed.
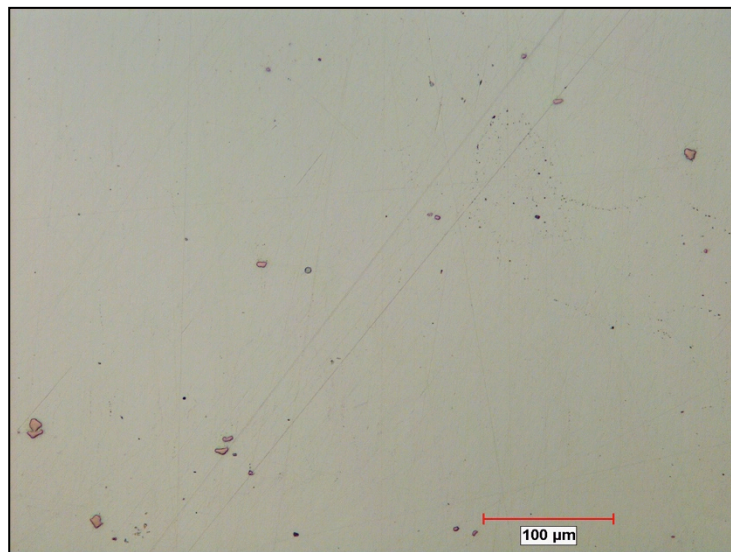


*Figure 2.3.1.6. Improperly polished sample with clear surface scratches*

Removal of such flaws is done by determining the right polishing procedures, which include type and amount of polishing solution used, what polishing pads are best suited for the material as well as polishing time and amount of vertical force needs to be applied to the samples.  The three stages, which

the samples of Alloy 617 have endured, are necessary in order to best remove all flaws and prepare the samples for optical microscopy.

The first round of polishing is accomplished on an MD-Dac polishing cloth with DiaPro polishing solution. DiaPro polish is a water based 3-micron diamond suspension with lubricants. For this phase of polishing, the pad platform and sample holder spin in the same clockwise direction at 150 rpm for a total of three minutes. During the three-minute span, the sample holder also applies a 30 N force to the sample being polished. Throughout the duration of this phase of polishing, additional polishing suspension and distilled water are applied to the polishing pad. Additional solution is applied every 20 s after polishing begins, while distilled water is applied to the pad every 30 s after polishing begins. The reason for adding polishing solution is due to the fact that as the pad platform spins it causes the solution to be forced to the edge of and eventually off of the pad, thus resulting in the need of additional solution. Also, distilled water is applied in order to remove any large sample fragments, which could potentially scratch the polished face of the sample.

The second and third rounds of polishing are completed using the same polishing pad and solution. The pad used is an MD-Chem cloth final polish pad made of porous neoprene. The polishing solution used is OP-AA suspension, which is an acidic alumina suspension. Polishing time using this pad and solution combination is two minutes, for both the second and third polishing phases. The differences between the phases are in the force applied to the samples as well as the spin direction. In the second polishing phase, a force of twenty newtons is applied to the sample, which is being rotated by the sample holder in a counterclockwise manner, while the polishing pad continues to be rotate clockwise. For the latter polishing phase, a fifteen-newton force is applied to the sample, and the polishing pad and sample holder rotate in a clockwise fashion. For both the second and third rounds of sample polishing, the sample holder and polishing pad still rotate at a speed of 150 rpm. Also, through the duration of these two phases, similar to the first round of polishing, additional polishing suspension and distilled water are applied to the polishing pad, with polishing solution applied every twenty seconds and distilled water being applied every thirty seconds.

Once mechanical polishing of a sample using the MD-Chem cloth pad and OP-AA suspension is completed, a residue from the polishing suspension is evident on the surface of the sample. In order to remove this, an additional MD-Chem cloth pad is needed. The pad used to remove the residue has had no prior use in polishing samples. This pad is wetted using distilled water and the sample surface is lightly slight across the wet pad. During this process, not vertical force is applied to the sample. Removal of the residue marks the conclusion of the polishing portion of sample preparation.

*Sample Etching*

Etching marks the final step in optical microscopy sample preparation. Etching includes using an acid or other penetrating solution to remove excess residues or surface particles such as dust or other small artifacts not removed by polishing. The result of etching includes clear exposition of grain boundaries, voids and other aspects that are incapable of being focused within the optical microscope without the use of a surface etchant. However, in order to be able to see such microstructural aspects, a sample must be etched with the proper etchant for the appropriate amount of time. Under-etching results in the inability to clearly see aspects of sample microstructure, while over-etching removes certain aspects entirely. Figure 2.3.1.7 shows a micrograph of Alloy 617, which has been under etched, while Figure 2.3.1.8 shows a sample that has been over etched. In order to compare the effects of under and over etching, Figure 2.3.1.9 shows a properly etched sample. All three of these figures are at a magnification of 200X.
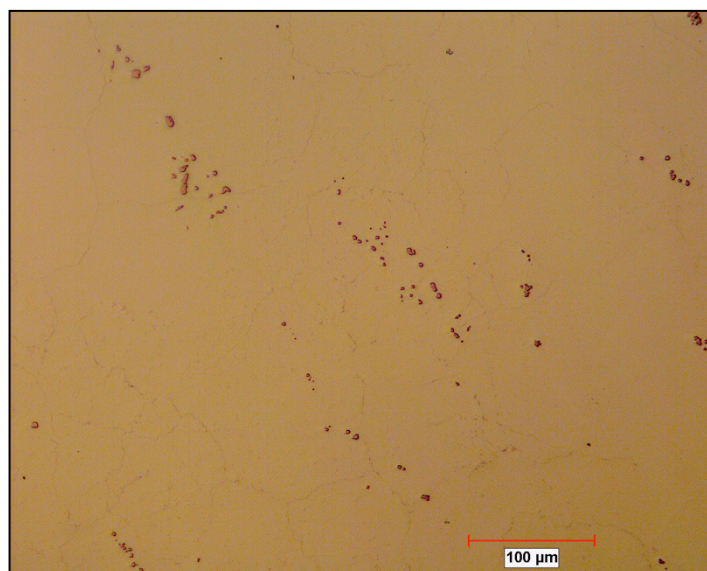
*Figure 2.3.1.7.* Under etched sample of Alloy 617
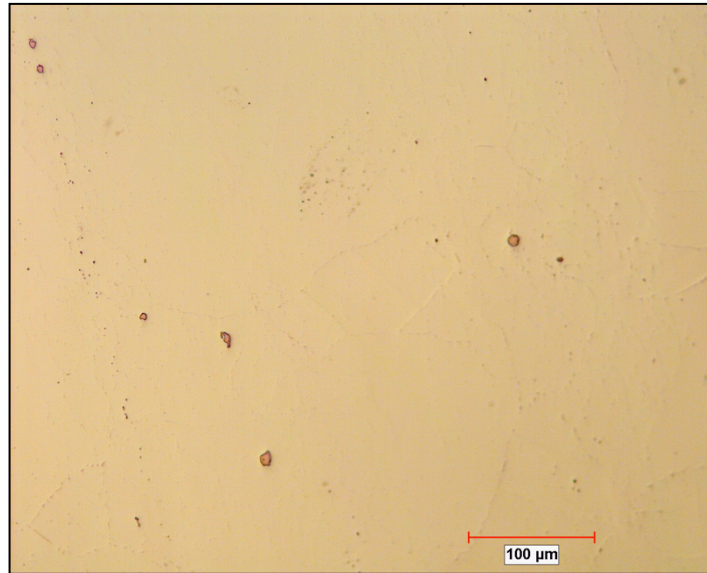
*Figure 2.3.1.8. Over etched sample of Alloy 617*
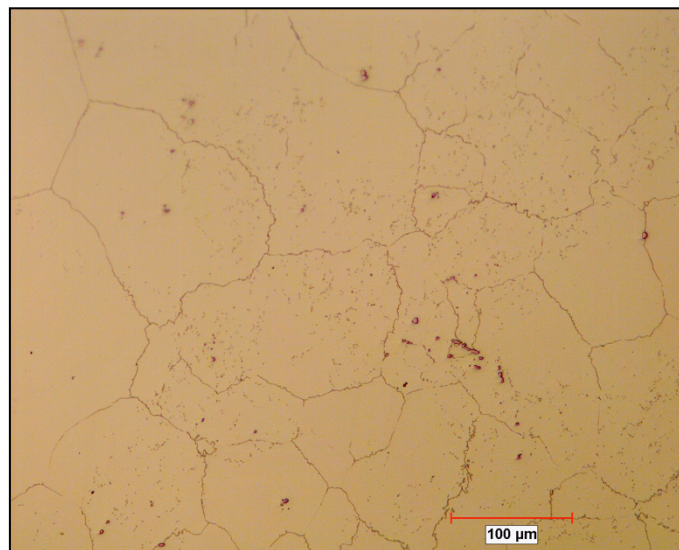


*Figure 2.3.1.9. Properly etched sample of Alloy 617*

In order to properly etch the polished samples, a solution consisting of three acids was used.  The acids are hydrochloric, acetic and nitric acids at volumes of 30, 20, and 20 mL, respectively.  These three acids are mixed and applied to the surface of the samples via a dropper, and remain on the samples for 9.5 minutes.  The time duration that the samples were exposed to the etchant was determined by means of trial and error.  Experimentation with etching times of 1-12 minutes was conducted.  From this, it was determined that etching for 9.5 minutes resulted in good clarity of grain boundaries, with little over

etching.  Once the etching period is complete, the etchant is then removed and distilled water is applied to the samples, which are then ready for optical microscopy.

*Results and Analysis*

Each form of testing differently impacts the microstructure of Alloy 617.  As a result of the testing conditions, in each sample there are different aspects that will be focused on during analysis.  Within thermally aged samples, the oxide thickness and thickness of the carbide depletion region will be the main focus. However, for creep-tested samples, precipitate identification and precipitate concentrations are the key areas of interests.  Finally, for low-cycle fatigue tested samples, emphasis will be on twinning and precipitate concentration, especially those around grain boundaries. All samples will then be compared to the as-received material, and is shown in Figure 2.3.1.10.
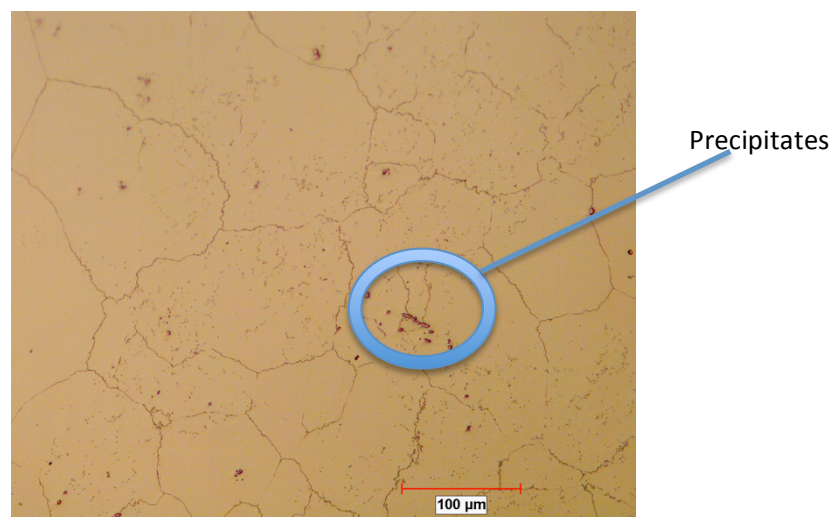


**Figure 2.3.1.10.** *As-received Alloy 617*

Within Figure 2.3.1.10 there is clear evidence that precipitates exist.  By using ImageJ analysis software, 21,657 particles of size 0.225 um exist in an area of 0.252 mm$^2$ with an average particle size of approximately 1 um.  It is assumed that the majority of these particles are some form of precipitate.  In addition, the precipitates do not appear to be at the grain boundaries.  Also, there appears to be no twinning evident in this image.

*Analysis of Thermally Aged Samples*

Of the four samples exposed to thermal aging, those exposed for 312 and 1248 h will be assessed in order to establish a comparison.  Figures 2.3.1.11 and 2.3.1.12 show the material near the surface for aging times of 312 and 1248 h respectively.
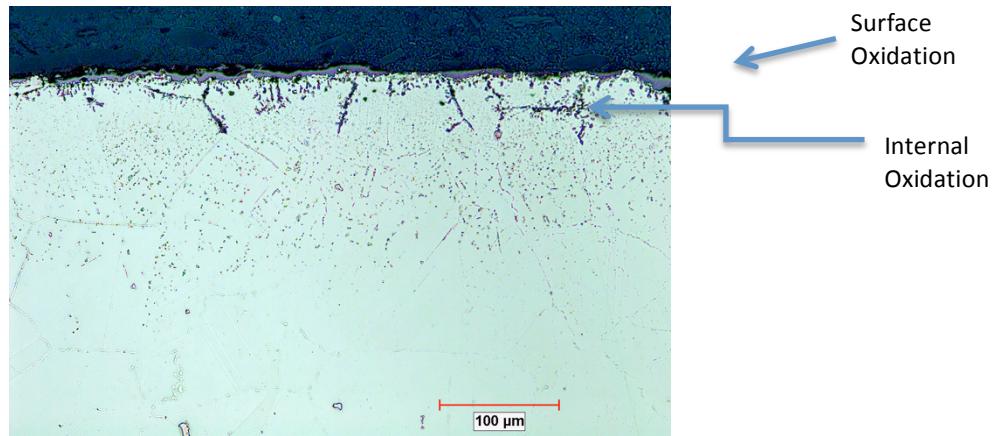
*Figure 2.3.1.11. Alloy 617 thermally aged for 312 h at 950°C*

As anticipated, surface and internal oxidation is evident as well as a carbide-depleted region is evident in Figure 2.3.1.11. Within this sample, the measured thickness of the surface oxidation layer is approximately 9 um, while that of the internal oxidation is approximately 55 um at the deepest point. In addition, the thickness of the carbide-depleted region is approximately 95 um from the surface of the sample, or 45 um from the deepest point of the internal oxidation.
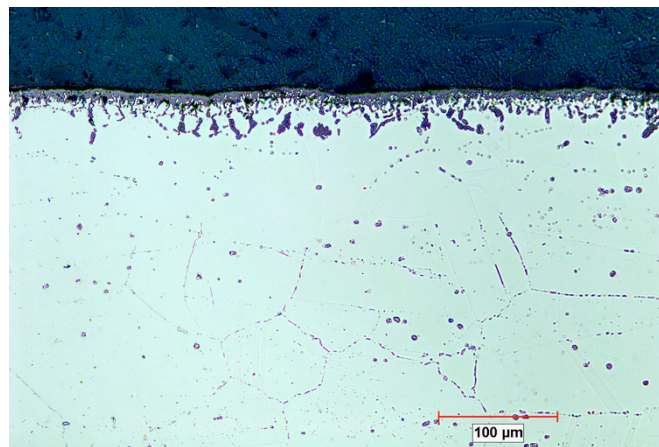


*Figure 2.3.1.12. Alloy 617 thermally aged for 1248 h at 950°C*

Figure 2.3.1.12 also indicates surface and internal oxidation, as well as a carbide-depleted region. However, in Figure 2.3.1.12 the thickness of the surface oxidation is approximately 10 um, while that of the internal oxidation is approximately 45 um. Also, the thickness of the carbide-depleted region is approximately 135 um from the sample surface or approximately 90 um from the deepest point of internal oxidation. Within both samples, no twinning is evident. It is worth noting that both micrographs show a large number of particles directly beneath the internal oxidation, which could suggest that these particles are carbides or other precipitates. However, they are not precipitates, they

are nothing more than dust, which had accumulated on the polished and etched face of the sample in the time frame of preparation completion and performing optical microscopy.

*Analysis of Creep-Tested Samples*

As previously stated, the key areas of interests for creep-tested samples are precipitate identification and their concentration in the samples.  The precipitates focused upon are those which are 0.2 um or larger.  This is due to results yielded from SEM.  When conducting SEM, it was found that the smallest evident precipitates had one dimension that was no smaller than 0.2 um.  In addition, there appeared to be two types of precipitates within the samples.  These were precipitates of size greater than 5 um and those of size less than 5 um.  It can also be stated that the precipitates of each category all had similar shape and color. Data regarding precipitate concentration in each of the creep-tested samples in provided in Table 2.3.1.1.

**Table 2.3.1.1.** *Creep-tested sample precipitate concentrations*

| Sample | Area Analyzed (square mm) | Total Precipitates | Precipitates of Size > 5 microns | Precipitates of Size < 5 microns | Average Size (microns) |
|---|---|---|---|---|---|
| C02 | 0.252 | 166 | 52 | 114 | 3.563 |
| C04 | 0.252 | 350 | 82 | 268 | 2.162 |
| C05 | 0.252 | 136 | 72 | 64 | 5.88 |
| C06 | 0.252 | 146 | 23 | 123 | 3.266 |
| Note: precipitates counted of size 0.2 micron or larger | | | | | |

From the data givin in Table 2.3.1.1, it appears that there is a direct correlation between engineering strain and average precipitate size, as well as time taken to get to 950°C and average precipitate size.  For example, the time necessary for sample C05 to get to 950°C was the shortest of all samples, and it has the largest average precipitate size.  However, sample C02 had the third shortest time necessary to get to 950°C, but it had the greatest engineering strain at removal, and the second largest average grain size.  Also, it seems that there is also a relationship between time taken for the samples to get to 950°C and number of precipitates.  Sample C04 was heated much faster than the other samples, and had many more precipitates than the others.

In order for the results of this research to be valuable to fellow members of the research group developing nondestructive testing methods, the composition of precipitates is needed in addition to their size and concentration. This analysis was performed on two creep-tested samples, C02 and C06.  In order to complete such analysis, scanning electron microscopy and electron dispersive spectroscopy were employed.  Figure 2.3.1.13 is an SEM generated image of sample C02 at a location near the failure surface.
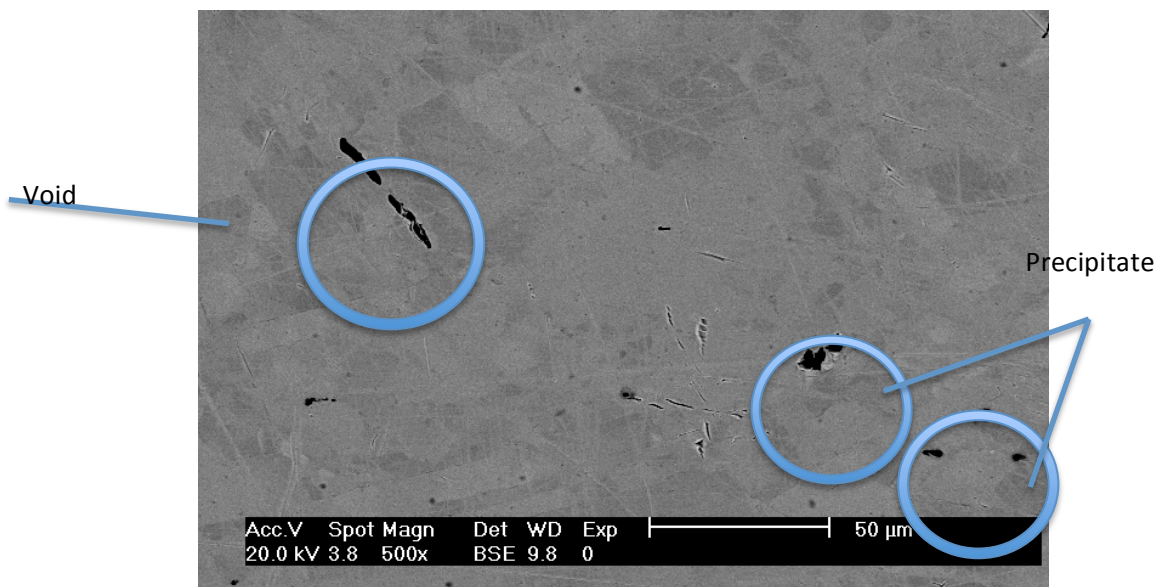
*Figure 2.3.1.13.* SEM image of creep tested Alloy 617 sample C02

In Figure 2.3.1.12, both precipitates and voids are present.  Voids have an elongated shape and form as the material approaches failure or rupture.  Also, the voids appear to grow along the grain boundaries. The precipitates have a more polygonal shape. Within Figure 2.3.1.14, the precipitates are dark, almost looking like voids; this is due to the fact that the precipitates are of lower density than the Alloy 617 matrix. The electrons within the beam generated by the SEM hit the precipitate material and go right through it, as do the ejected x-rays, which are caused by the electron beam contacting the Alloy 617. Both the beam and ejected x-rays fail to recognize the precipitate due to the density difference between it and the matrix.  Figure 2.3.1.14 shows another view of a precipitate within the same sample, but at a higher magnification.
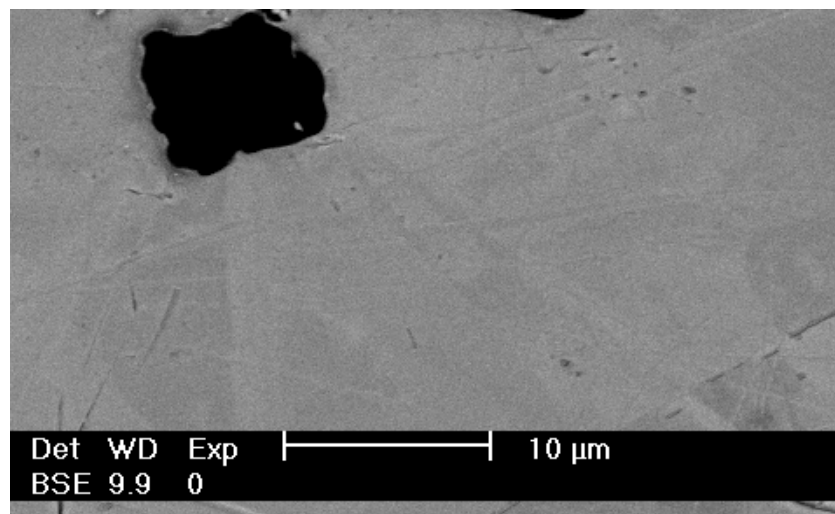


*Figure 2.3.1.14.* Precipitate in crept sample C02

The precipitate shape is very comparable to a square (Figure 2.3.1.14). This specific precipitate represents one of two common precipitate sizes found in the crept samples via SEM. It represents the

larger of the two types of precipitates.  Energy dispersive x-ray spectroscopy (EDX) was conducted in order to determine its composition. The EDX results provide the basis for concluding that the larger precipitates are titanium nitride rich carbides as shown in Figure 2.3.1.15.
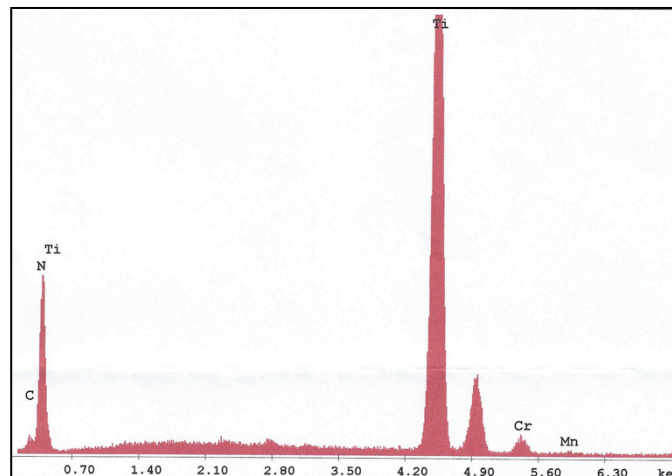


**Figure 2.3.1.15.** *EDX results for larger size precipitate*

As mentioned above, smaller size precipitates were also found.  These precipitates are smaller than 5 um and are located primarily along grain boundaries in the crept samples. Examples of these precipitates are shown in Figure 2.3.1.16, which is at a much higher magnification than Figure 2.3.1.14.
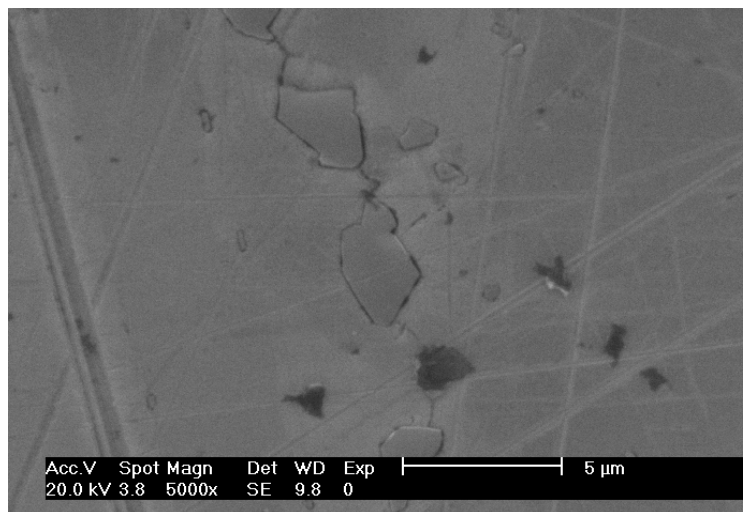


**Figure 2.3.1.16.** *Smaller precipitates in crept sample C02*

EDX results for the small precipitates in Figure 2.3.1.16 are shown in Figure 2.3.1.17 and indicate Cr and Mo are primary consituents, rather than Ti. Due to their constituents, these carbides are expected to be much more brittle than the larger Ti ones.  Also, because of their location and orientation, buildup of these carbides with increasing strain will likely cause voiding along the grain boundaries. SEM and EDX

were also conducted on sample C06, which yielded the same results as sample C02, thus confirming the existence of the carbides in multiple samples. Rao et al. also identified two types of carbides in crept Alloy 617 samples; Ti(C,N), which is the same as the larger titanium nitride rich carbide we found, and $M_{23}C_6$ as well as the variant form $M_6C$. These carbides are chromium and molybdenum rich, as are the smaller carbides that we found along the grain boundaries.
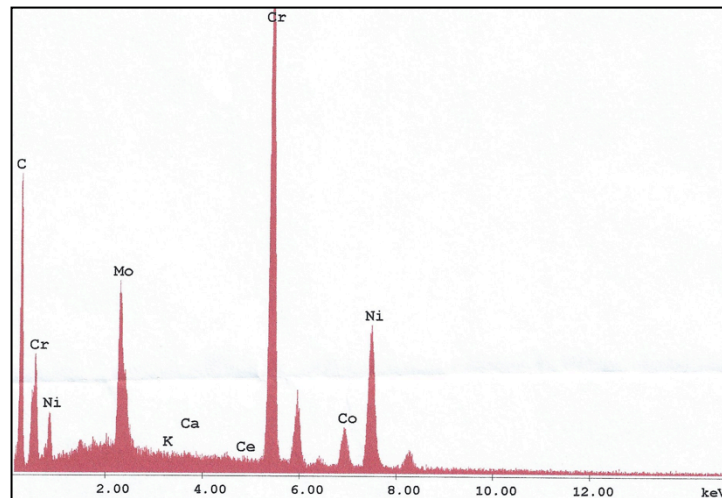


*Figure 2.3.1.17.* EDX results for smaller precipitates

*Analysis of Low-Cycle Fatigue Tested Samples*

The precipitate concentration in the low-cycle fatigue samples was investigated. As with the crept samples, ImageJ was used for precipitate analysis. However, SEM and EDX were not used to confirm the composition of precipitates. Table 2.3.1.2 provides the precipitate data for the fatigue-tested samples.

*Table 2.3.1.2.* Precipitate data for low-cycle fatigue samples

| Sample | Area Analyzed $(mm^2)$ | Total Precipitates | Size > 5 um | Size < 5 um | Average Size (um) |
|--------|------------------------|--------------------|-------------|-------------|--------------------|
| LCF-3  | 0.252 | 326 | 31 | 295 | 1.81 |
| LCF-5  | 0.252 | 679 | 42 | 637 | 2.09 |
| LCF-17 | 0.252 | 534 | 21 | 513 | 2.099 |
| Note: precipitates counted are 0.2 um or larger | | | | | |

It is clear that there are many more precipitates in the low-cycle fatigue samples than there are in the creep samples. In addition, the average size of the precipitates is much smaller. It appears that the majority of the precipitates accumulate along the grain boundaries as shown in Figure 2.3.1.18, similar to the smaller precipitates in the creep samples.
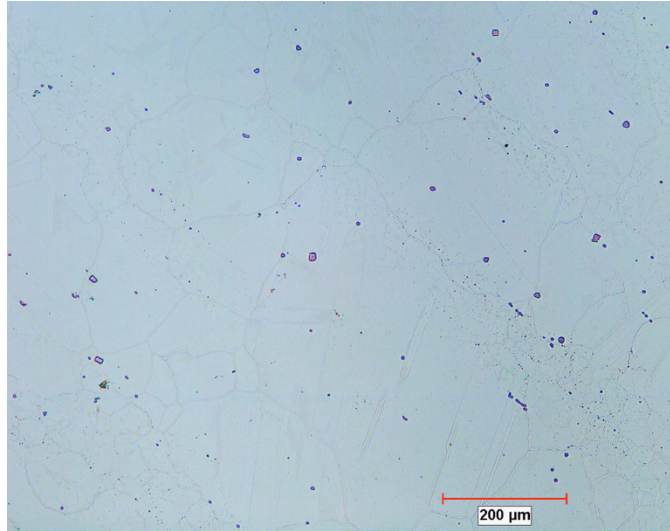
*Figure 2.3.1.18.* Low-cycle fatigue sample LCF-5

### 2.3.2 Scanning Electron Microscopy

Scanning electron microscopy was conducted on creep samples as described in section 2.3.1 and Xiaochu Yao's M.S. thesis, which is included in this report as Appendix B.

### 2.3.3 Transmission Electron Microscopy

### 2.3.3.1 Thermally Aged Specimen

Sample T-2 was taken from a specimen that was thermally aged at 950$^o$C for 26 days (624 hours), while sample T-0 was taken from as-received material. TEM samples are required to be very thin in order to have electron transparency. The TEM images of samples T-0 and T-2 are shown in Figures 2.3.3.1 and 2.3.3.2 respectively.
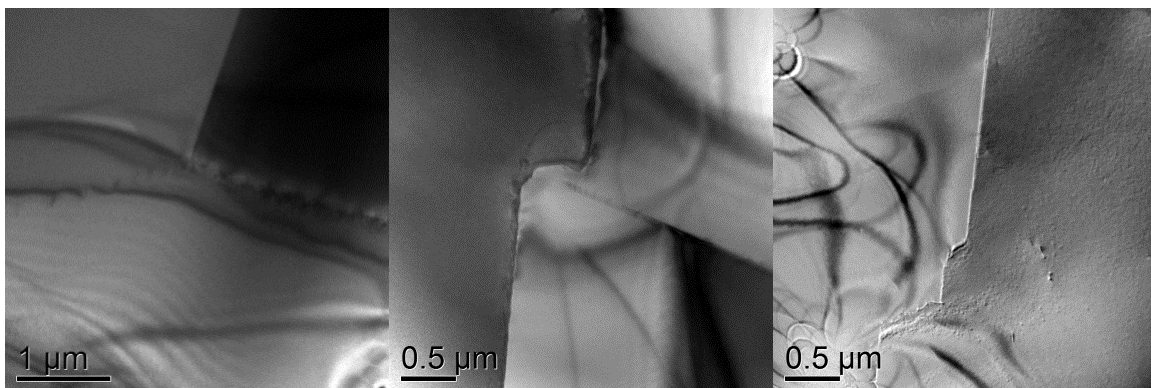


*Figure 2.3.3.1.* Sample T-0 partial view of grain boundaries with very low dislocation densities and thickness fringes (thicker dark bands)
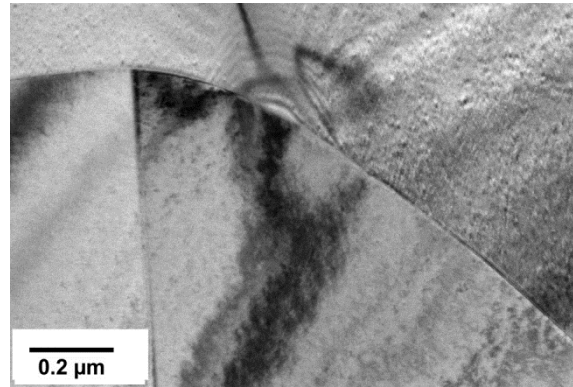
*Figure 2.3.3.2. Sample T-2 showing grain boundaries*

17 precipitates were imaged from the as-received T-0 sample and 19 precipitates were imaged from sample T-2 (aged 624 h). It is important to remember that the TEM samples of these specimens are thin slices of 3D material, thus care must be taken when making conclusions based on measured cross-sectional areas of precipitates. By increasing the number of measurements, the trend should approach the 'true' value. Measured areas of cross-sectional slices of precipitates were tracked in a histogram to compare sizes between samples T-0 and T-2. The sizes of these precipitates ranged between 0.04 and 0.83 um$^2$. From the histogram in Figure 2.3.3.3, it appears that the number of finer precipitates decreases with thermal aging for 624 h. This agrees with Chomette et al.'s (2010) observation where fine Cr-rich precipitates disappeared after 1000h at 950C.
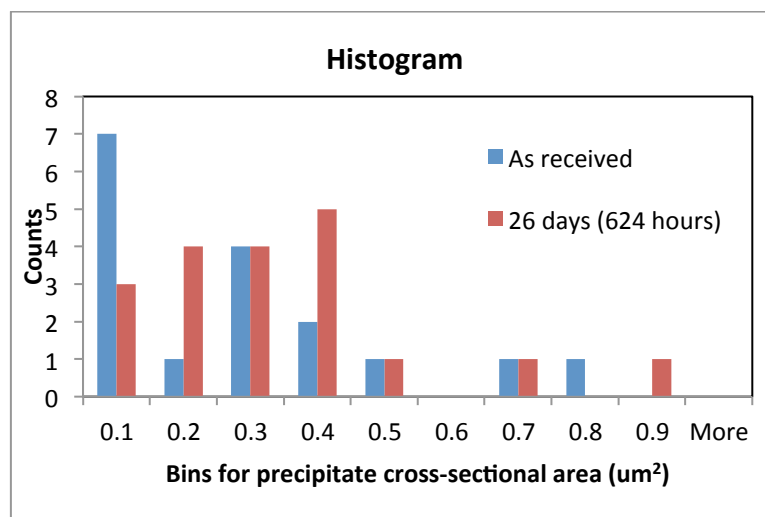


*Figure 2.3.3.3. Histogram for measured cross sectional area of precipitates of T-0 and T-2*

Both isolated and groups of precipitates were found for both samples T-0 and T-2. Based on the EDX analysis of both as-received and crept samples, it is highly likely that all imaged precipitates of T-2 are the M$_{23}$C$_6$ type. Many of the precipitates of the as-received samples exhibited sharper/straighter edges with a variable number of sides (2, 4, and more) as shown in Figure 2.3.3.4. The precipitates in aged T-2

were mostly polygonal with more rounded edges as shown in Figure 2.3.3.5. In addition, there was one unusual precipitate shown in Figure 2.3.3.6, which appears to be stuck between grain boundaries and flattened with straight edges when compared to the other more round precipitates. Chomette et al., 2010 have also noted $M_{23}C_6$ precipitates have appeared to be more globular after 1000 h at $950^{o}$C.
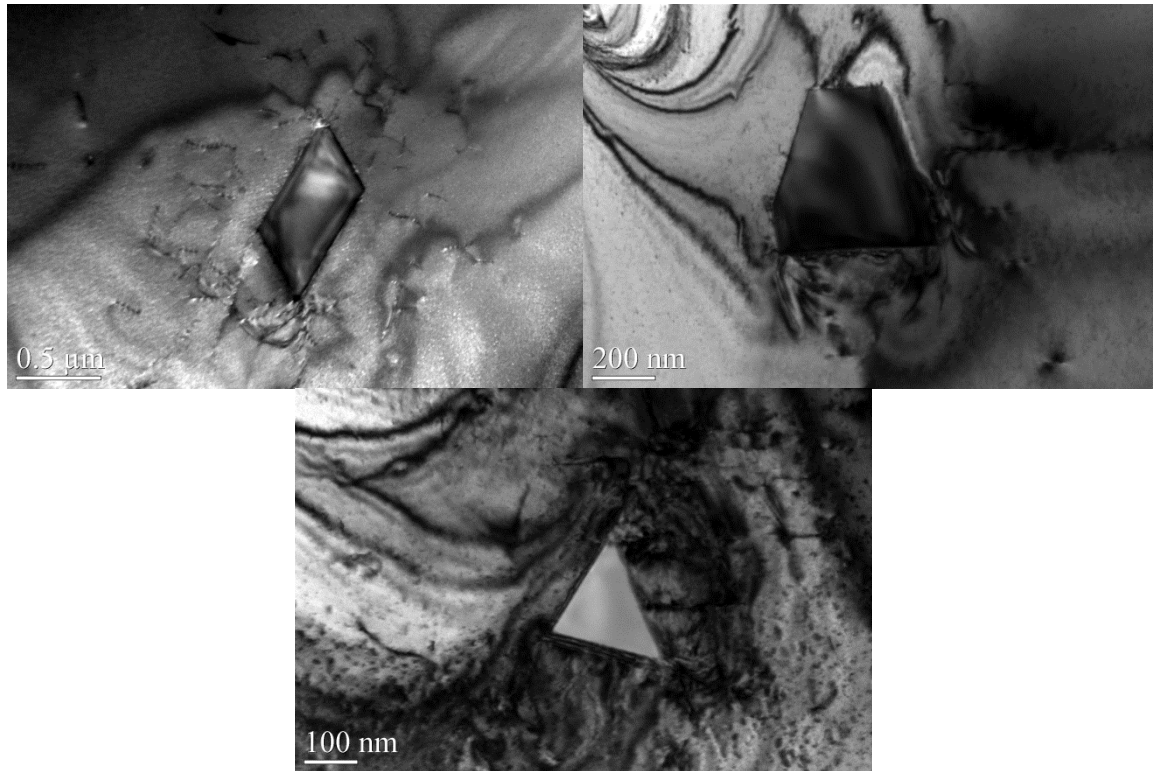


*Figure 2.3.3.4.* Precipitates observed within T-0 (as received)
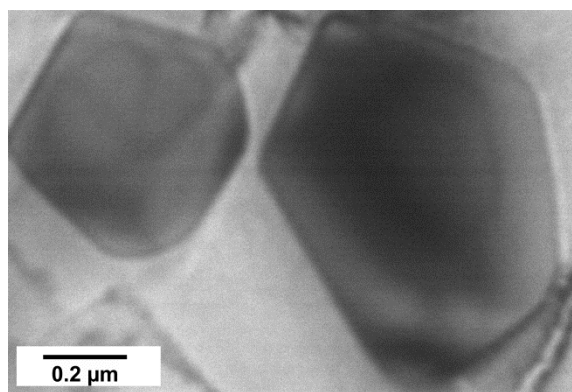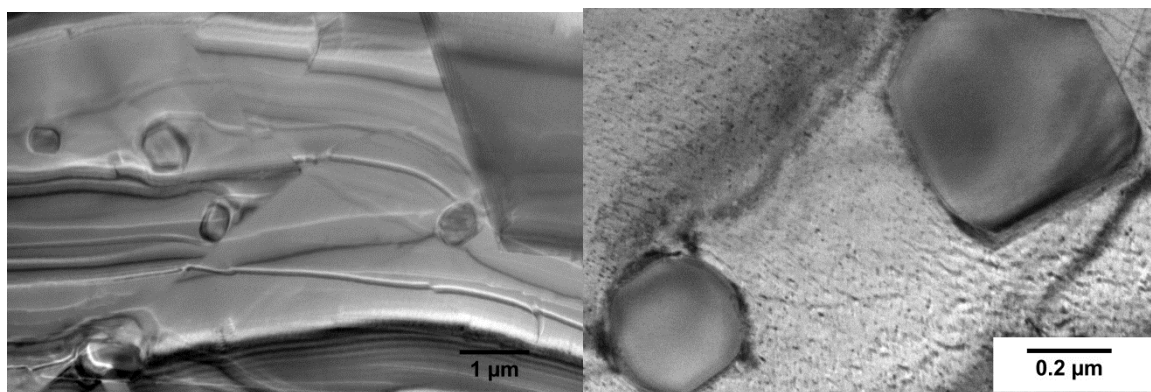
**Figure 2.3.3.5.** *Precipitates observed in sample T-2*
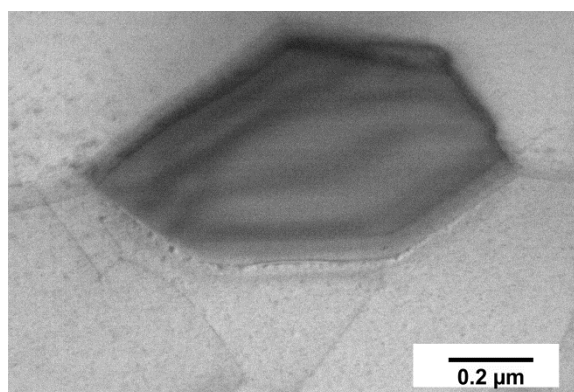


**Figure 2.3.3.6.** *Unusual precipitate from sample T-2*

*2.3.3.2 Biaxial Loading Specimen*

This section presents transmission electron microscopic (TEM) images of specimen 617-3, which was subjected to load path MR1 at 950$^o$C. The specimen endured 900 cycles (shear strain amplitude of 0.002 rad at a rate of 0.001%/s with a constant axial stress of 12 MPa). After 900 cycles the specimen had a large transverse crack, but had not separated into two pieces. Three samples were cut from specimen 617-3, each at a different orientation with respect to the cross-sectional plane of the specimen, as shown in Figure 2.3.3.1. Orange outlines in the figure are used to indicate the orientation of the slice plane with respect to the generator of the cylinder. The purpose of three views (at 0, 45, and 90 degrees) is to more completely investigate the deformation mechanisms of a polycrystalline material at high temperature under complex biaxial loading that induced creep-fatigue interactions. Samples from the pristine undeformed material were also examined.
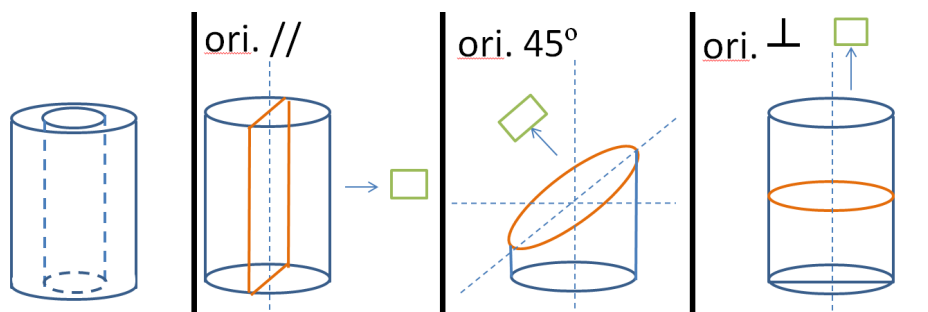


**Figure 2.3.3.1.** *Sectioning of tubular specimen for TEM viewing. Sections were oriented parallel (// or 0$^o$), at 45 degrees (45$^o$), and perpendicular ($\perp$ or 90$^o$) to the generator axis of the cylindrical tube.*

A medium speed saw was used to cut smaller pieces from the cylindrical specimen in order to have pieces sufficiently small to fit into the low-speed saw apparatus. The rectangular dimensions had cross-sections that fit within a 3mm diameter TEM sample holder with a slit. Both sides were mechanically and hand polished using diamond-grit embedded films with at least 5 um. The first polished side is bonded to the TEM sample holder using a 2-part epoxy and then heated for curing, before the second side is polished and the sample is thinned to less than 70 um. The slit in the TEM sample holder allows for dual beam ion milling near the center to form a small hole, via the Fischione instrument's low angle ion milling and polishing system such that the material region near the hole is electron transparent for TEM viewing.

A few of the images shown in this section were from the pristine sample T-0 as observed through the JEOL 2010F TEM/STEM, but since the maximum possible tilt angle was limited to about ±20°, there was difficulty in tilting for a proper diffraction zone of the precipitates. An additional viewing of the T-0-1 sample was conducted to reinvestigate the TiN and other precipitates with proper scale bars (ensured proper connection between microscope and recording computer). Three samples of specimen 617-3 and

another sample of T-0 were investigated using the JEOL 2010 LaB6, which has a larger tilt angle capability of ±40°.

The grain size of the as-received specimen T-0 was much larger than that observed from samples of speciman 617-3, as observed in the optical images of the ion milled surface of specimen T-0 shown in Figure 2.3.3.2. Additional TEM images of cross section areas/scaling are included as Figure 2.3.3.3 for later comparison with the highly deformed specimen 617-3. Dark long wavy bands are not real physical features of the specimen, but are fringes as a result of viewing through a thick region of the specimen. Contrast is noticeable between adjacent grains, and there are small dashed features representing a low density of dislocations that occur sparsely through the material and typically are located near grain boundaries or precipitates.

(a)



(b)
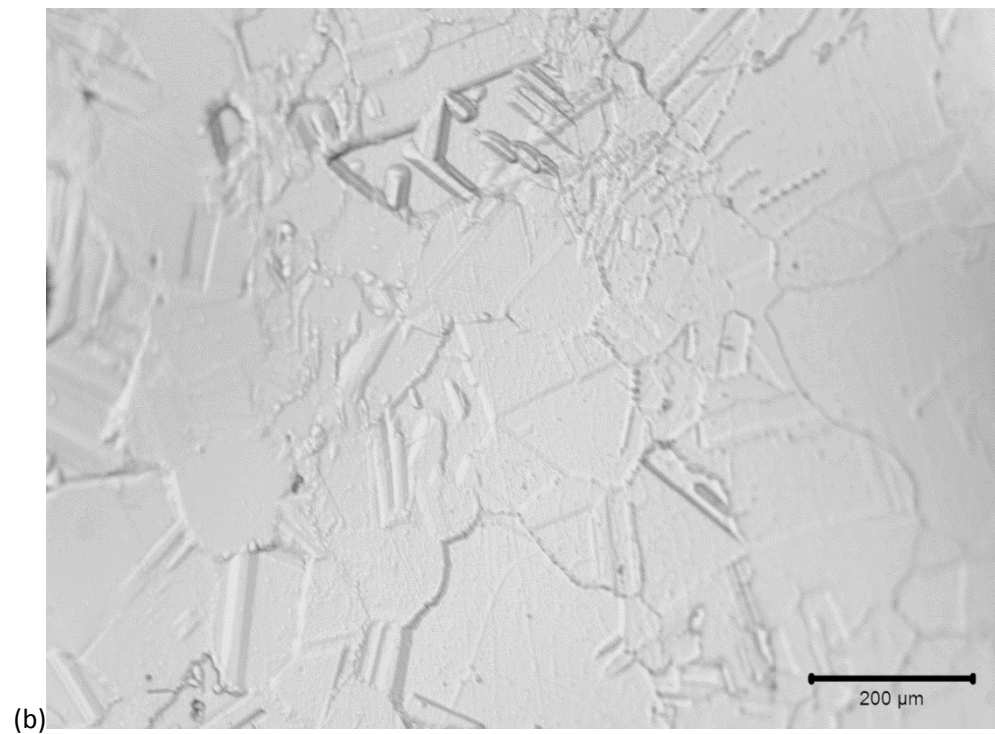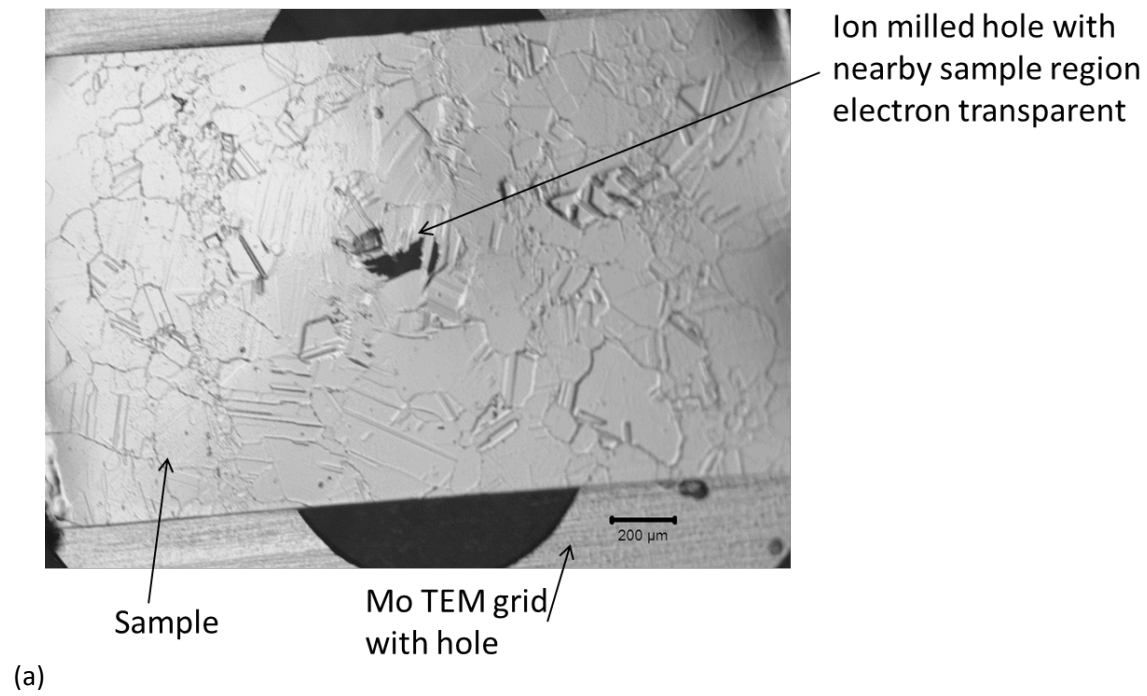
**Figure 2.3.3.2.** *Ion milling of the TEM sample T-0 from the as-received material polished the surface and revealed grain boundaries; these images are from an optical microscope.*
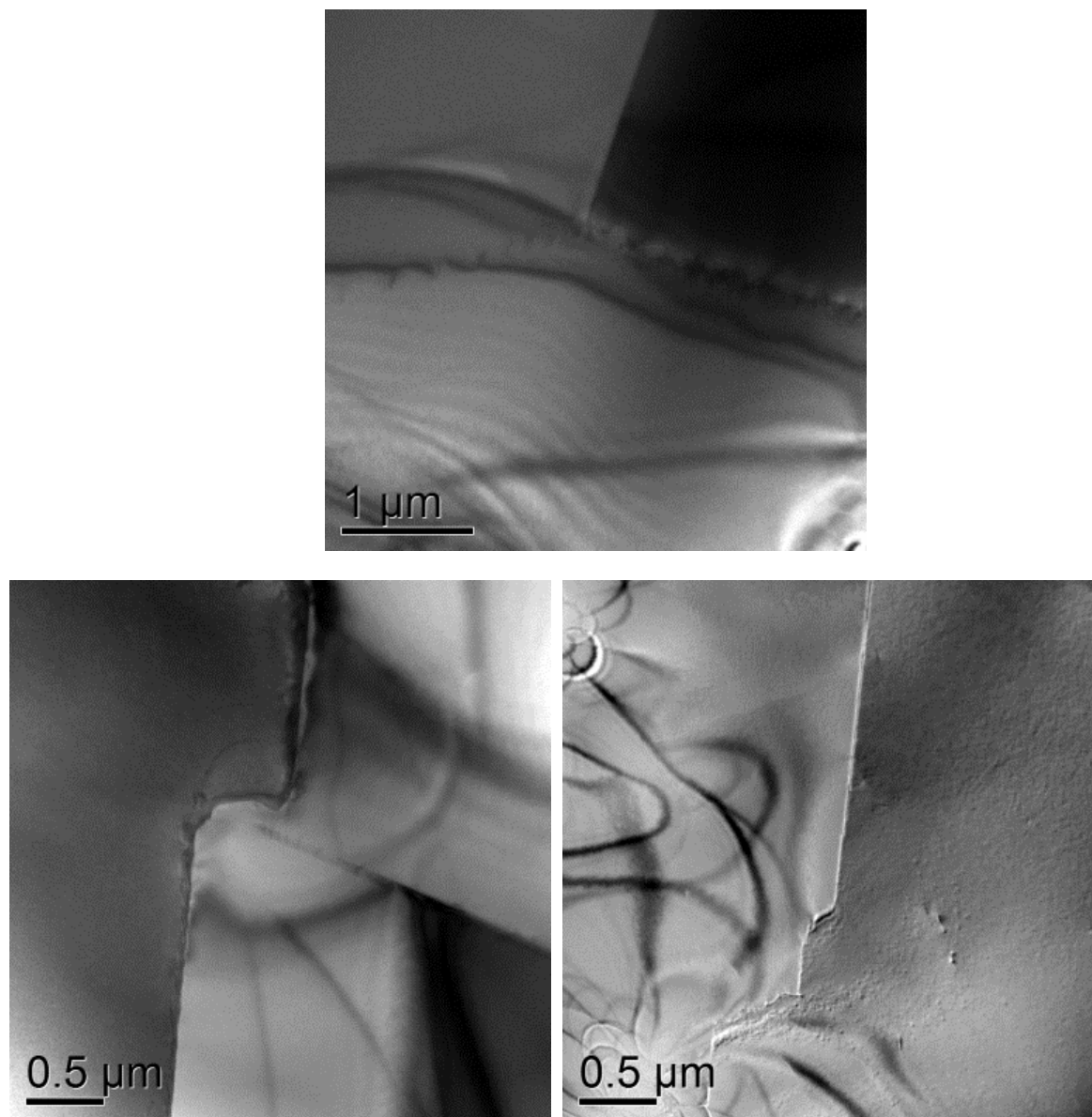
**Figure 2.3.3.3.** *As-received T-0 sample views by TEM provide partial views of grain boundaries with very small dislocation densities and thickness fringes (thicker dark bands).*

Closer examination of some of the edges of these grain boundaries revealed ordered networks of dislocations with nearly dislocation free regions within these grain boundaries. Groups of images are ordered according to the slice orientation of the sample, such that Figures 2.3.3.4, 2.3.3.5, and 2.3.3.6 correspond to orientations $0^o$, $45^o$, and $90^o$ respectively. These features could be a result of dislocation-dislocation interactions, where a decrease in dislocation density is exhibited in the interior and eventually caused the formation of low-angle grain boundaries in association with the loading and the high temperature, which arranged the dislocations into a lower energy configuration. For Specimen 617-3; both the $0^o$ and the $45^o$ orientations resulted in several of the low-angle grain boundaries being

parallel to each other. The images from the 45$^o$ orientation exhibit several boundaries with more clearly defined dislocations patterns than the other two orientations. Dislocation density within these unusual boundaries is very low for the 0$^o$ orientation, but slightly higher for the 45$^o$ and 90$^o$ orientations. With consideration to the torsional loading, comparison of other samples should be done for the 45$^o$ orientation.
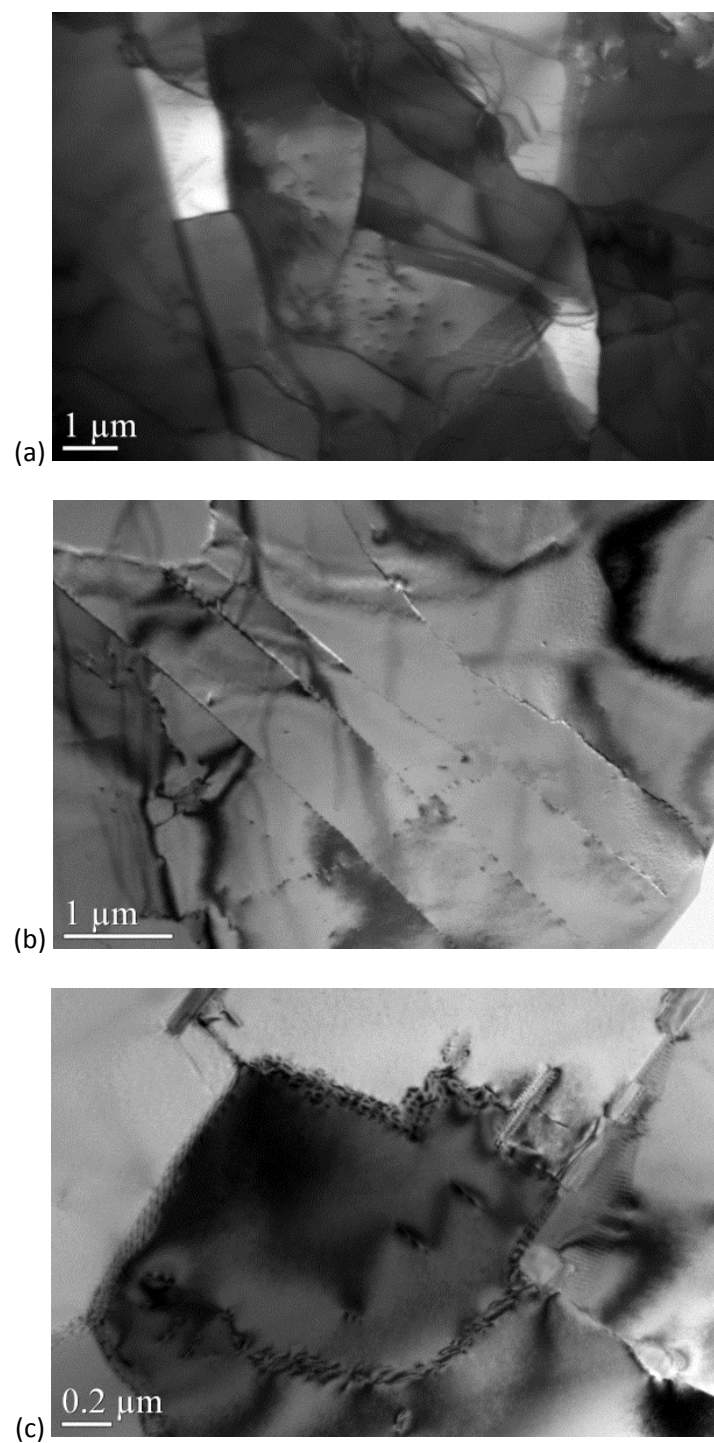
*Figure 2.3.3.4.* TEM sample images from specimen 617-3 viewed at $0^o$; smaller grains and dislocation networks at grain boundaries are evident.

(a)

(b)

(c)
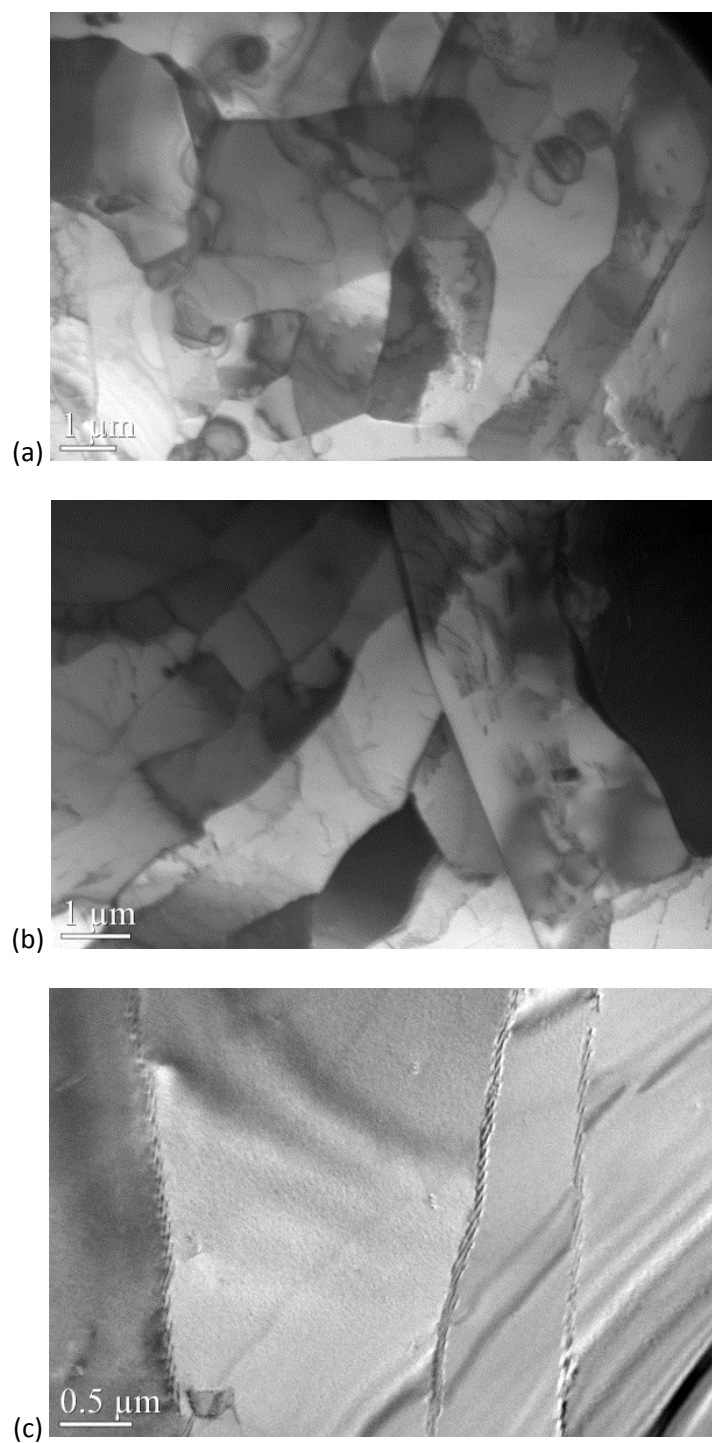
**Figure 2.3.3.5.** *TEM sample images from specimen 617-3 viewed at 45$^{o}$; smaller grains and dislocation networks at grain boundaries are evident.*
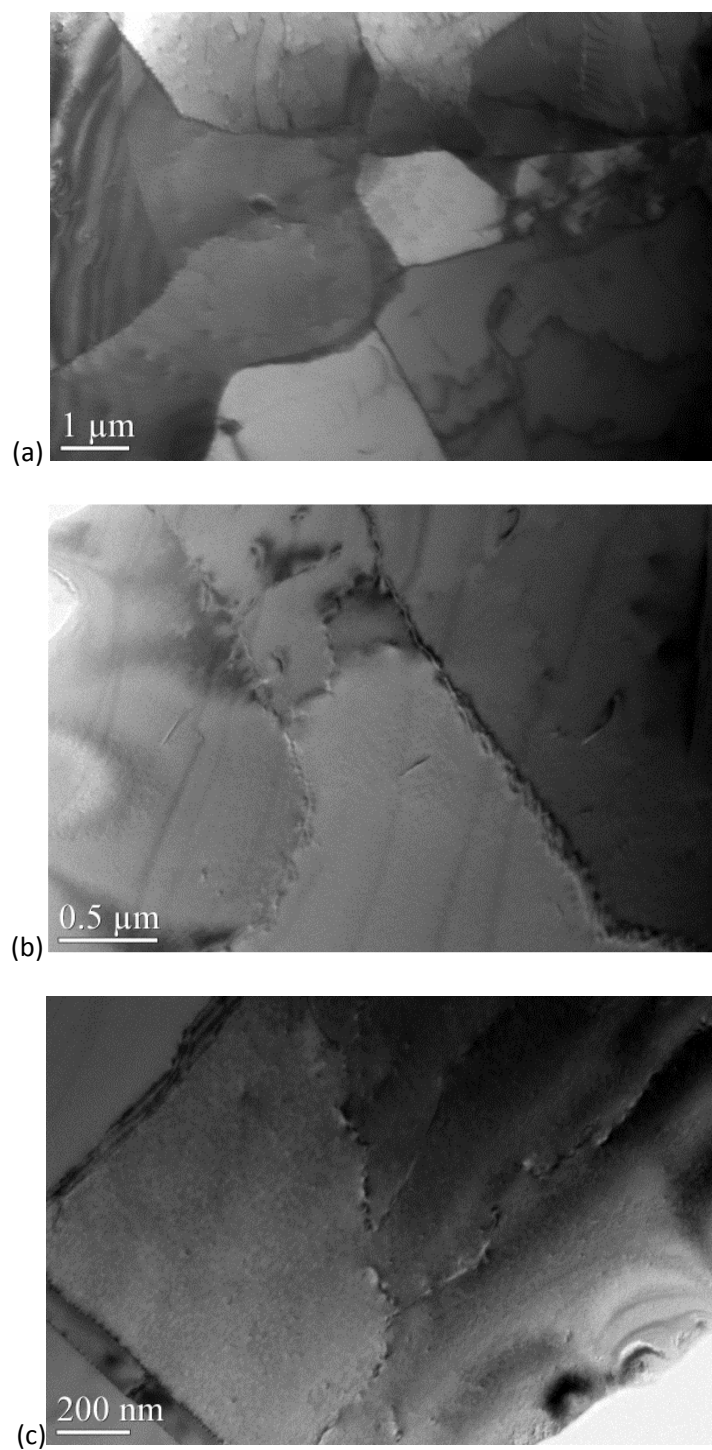
**Figure 2.3.3.6.** *TEM sample images from specimen 617-3 viewed at 90$^{o}$; smaller grains and dislocation networks at grain boundaries are evident.*

Energy dispersive X-ray spectroscopy (EDX) of most precipitates observed in the as-received sample T-0 were Cr-rich, indicating that they are of the $M_{23}C_6$ type based on comparison with the literature. The EDX spectrum of the matrix is also included below. However, $M_6C$ (Mo-rich) precipitates were not observed. A low density of dislocations are present near, and some are within, these Cr-rich precipitates (darker shaded shapes), which are shown to have irregular 2D cross-sections of 3D finite volumes, and could be explained due to the heat treatment causing strain mismatch between the precipitate and the matrix. The various shapes observed via 2D cross sections include long thin shapes and small triangular, rectangular, or circular shapes, some of which are shown in Figures 2.3.3.7 and 2.3.3.8. In addition, these single precipitates or small clusters (2 or 3) of precipitates are generally located far from each other. Figures 2.3.3.9 and 2.3.3.10 are TEM images of precipitates in samples from specimen 617-3. The precipitates found in the viewable region of the $0^o$ samples are comparable in size to those in sample T-0. Within the samples from specimen 617-3, there are generally small clusters of Cr-rich precipitates that are spaced far apart. In addition, some isolated single precipitates have also been found. There are several possible explanations for this trend, such as precipitation of new precipitates at particular points in dislocation networks as a result of loading and temperature or slicing of precipitates induced by the complex cyclic loading, but further investigation is necessary.
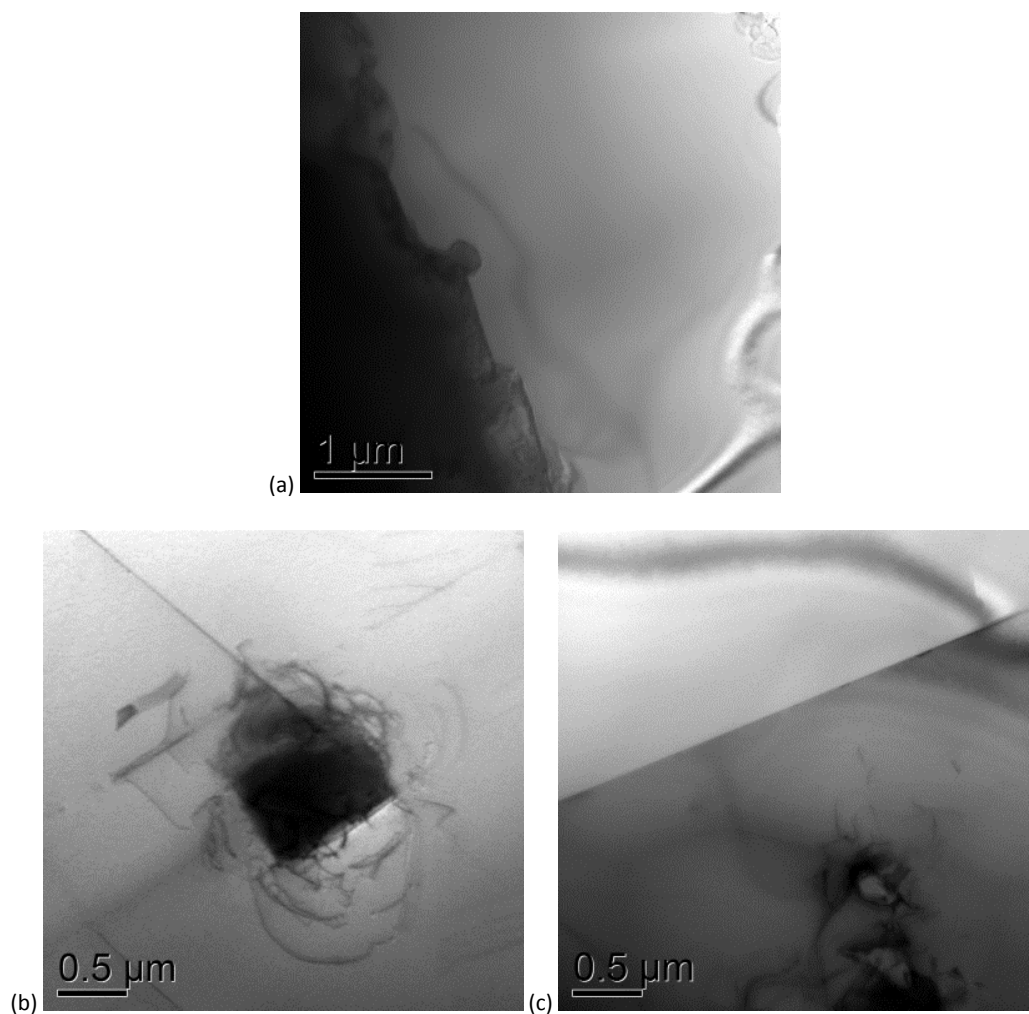
**Figure 2.3.3.7.** *As-received T-0 TEM images of isolated precipitates with a small surrounding region of dislocations; viewed with JOEL 2010F TEM/STEM.*
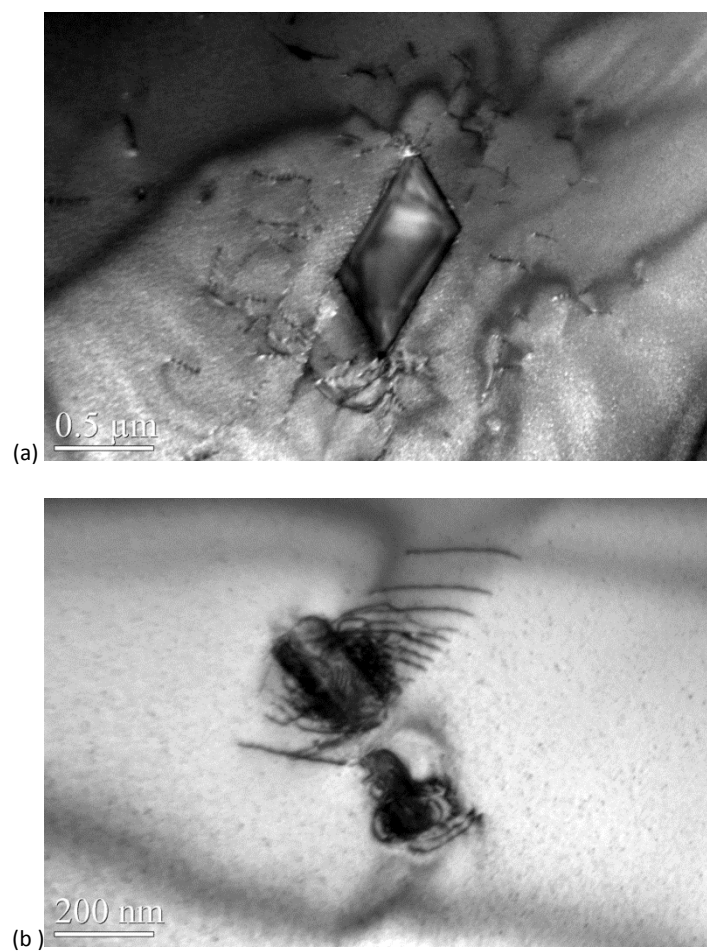
**Figure 2.3.3.8.** *As-received T-0 TEM images of isolated precipitates with a small surrounding region of dislocations; viewed with JOEL 2010 LaB6.*
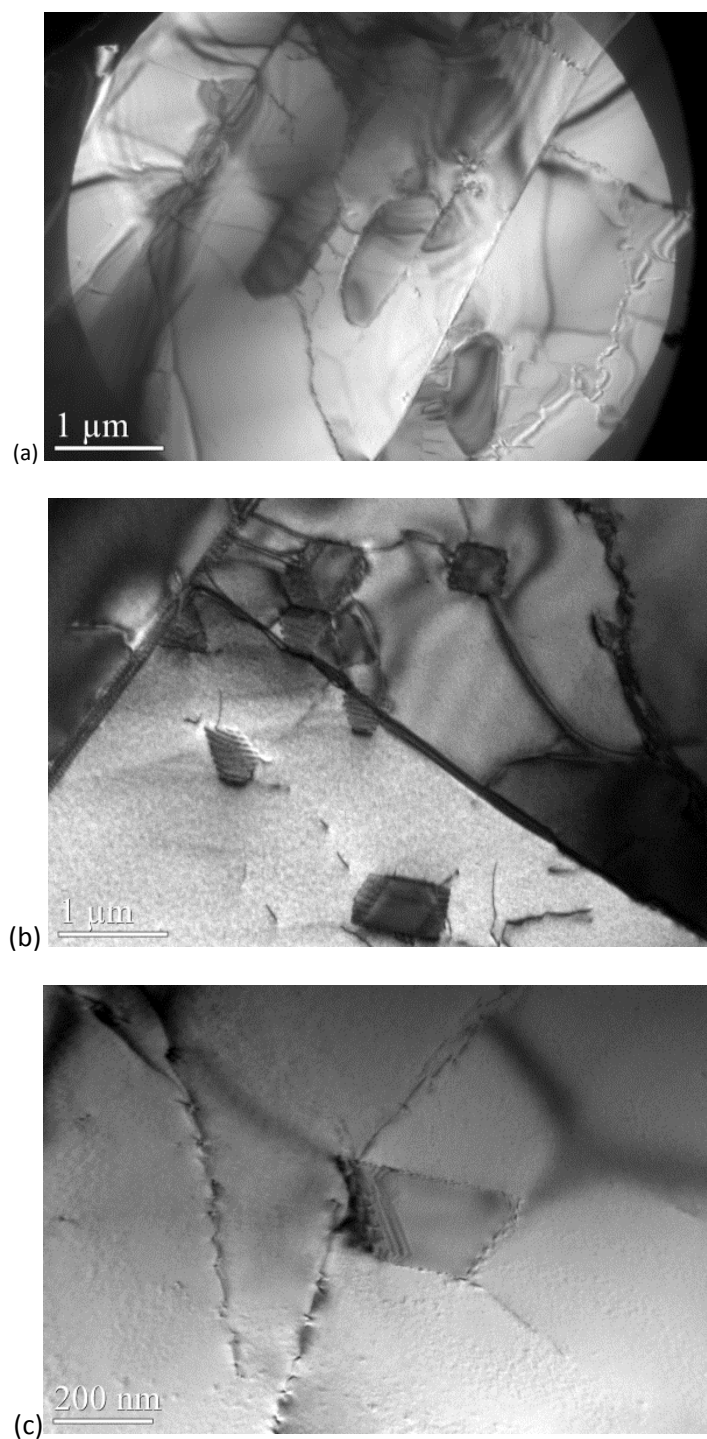
**Figure 2.3.3.9.** *TEM images from 0º samples from specimen 617-3 show isolated precipitates and clusters of precipitates with nearby dislocations; viewed with JEOL 2010 LaB6.*
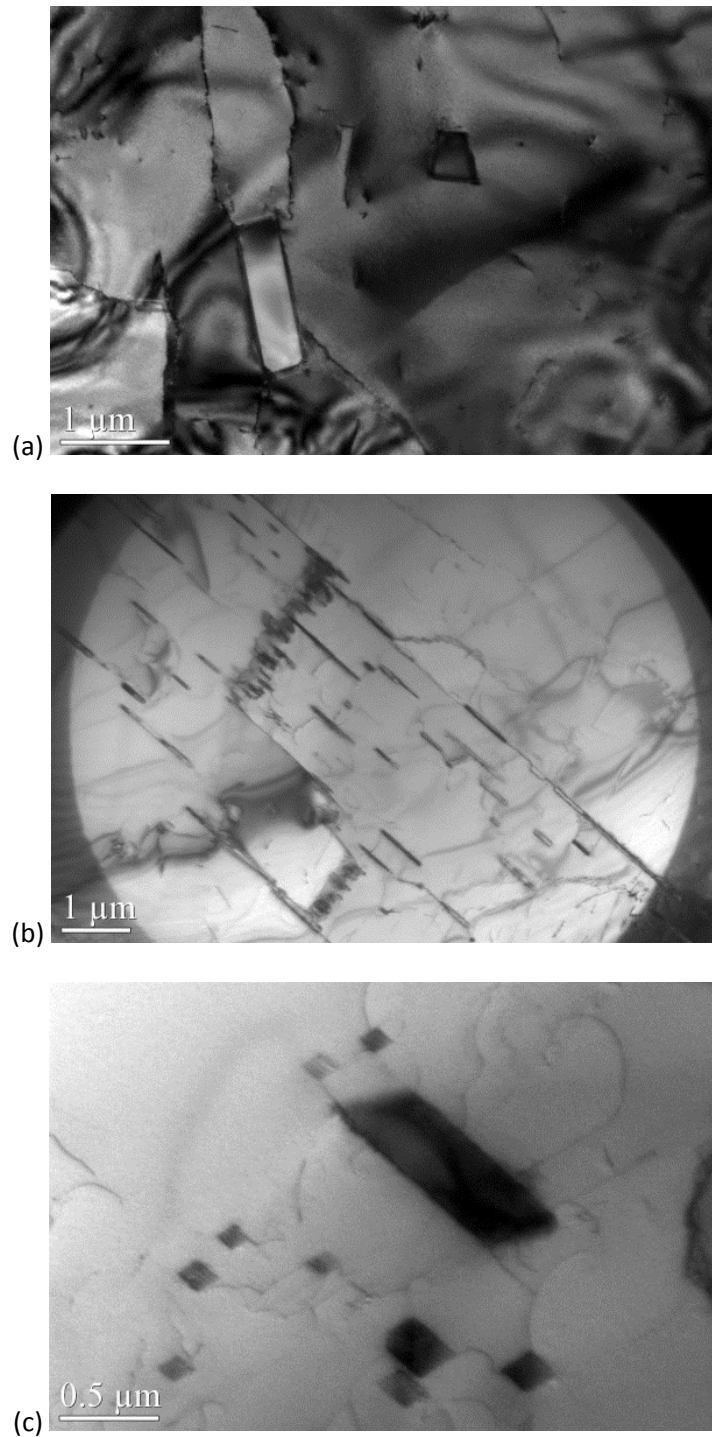
**Figure 2.3.3.10.** *TEM images from (a) 45$^o$ and (b and c) 90° samples from specimen 617-3 show isolated precipitates and clusters of precipitates with nearby dislocations; viewed with JEOL 2010 LaB6.*

In general there were more groupings of precipitates typically present in batches greater than 3 within specimen 617-3 than in as-received sample T-0, where the observed precipitates were typically present

as one or two in a given location, and yet isolated from other precipitates. However, depending on sample orientation with respect to the rolling direction, carbide banding has been observed by Benz et al. (and others in the literature). In carbide banding there are ~100-300 um wide bands having a high-density carbides alternating with carbide-free bands. However, this carbide banding was not observed in the as-received samples, and must be due to orientation with respect to rolling direction. Furthermore, in the $90^o$ sample for specimen 617-3 there was an isolated region containing many thin (both short and long) precipitates, where the diffraction pattern of a randomly selected region revealed the corresponding precipitates had diffraction spots that agreed with the matrix.

A Ti-rich phase was found only once in the as-received T-0-1 sample, and Ti is expected to be hard to find as it has a low weight percentage in Alloy 617. Figure 2.3.3.11 shows TEM images and EDX results for an as-received T-0 sample. The EDX analysis verifies that the lighter region, which has an unexpectedly dense dislocation distribution, is Ti-rich. It also shows that the darker outer region has the composition expected for the Alloy 617 matrix. A Ti-rich region was only observed once during inspection of the 0o sample from specimen 617-3, which is marked 1 in Figure 2.3.3.12 and EDX results are given in Figure. 2.3.3.12c. Nearby the Ti-rich region is a Cr-rich region, which is marked 2 in Figure 2.3.3.12 and the EDX results are given in Figure 2.3.3.12d. The Cr-rich region implies the presence of a $M_{23}C_6$ carbide. Region 3 marked in Figure 2.3.3.12 is the matrix as indicated in Figure 2.3.3.12e. Note that Figures 2.3.3.12a and 2.3.3.12b are the same location, but the images are taken at different tilt angles.

(a)



(b)

(c)



(d)
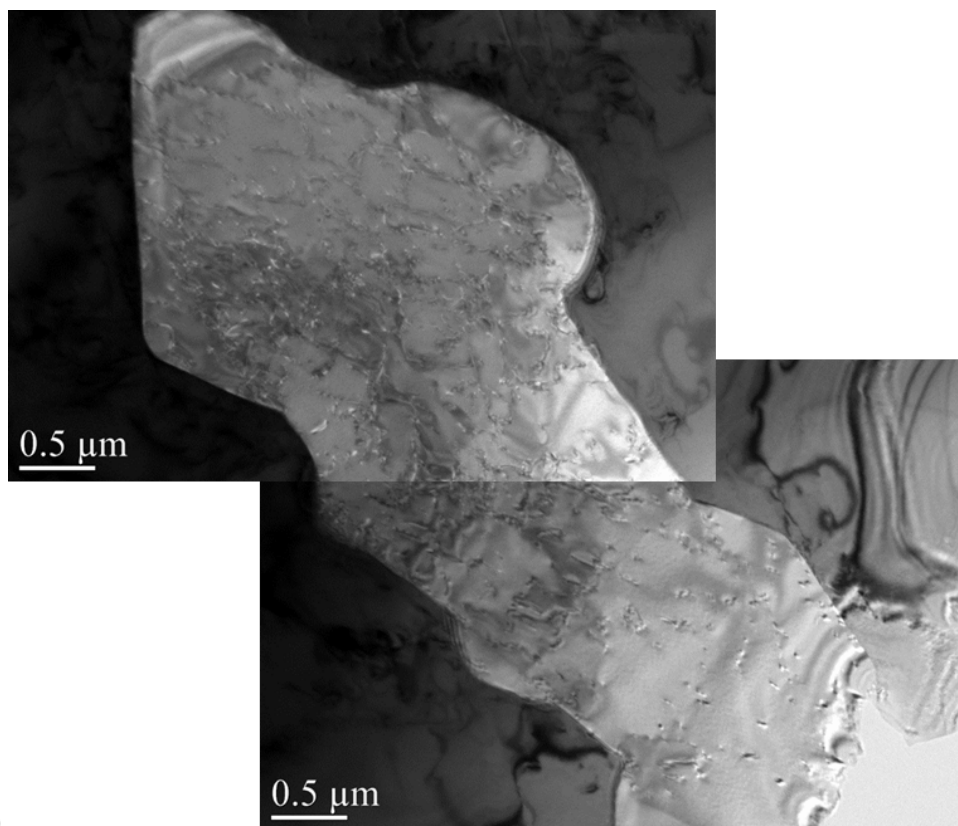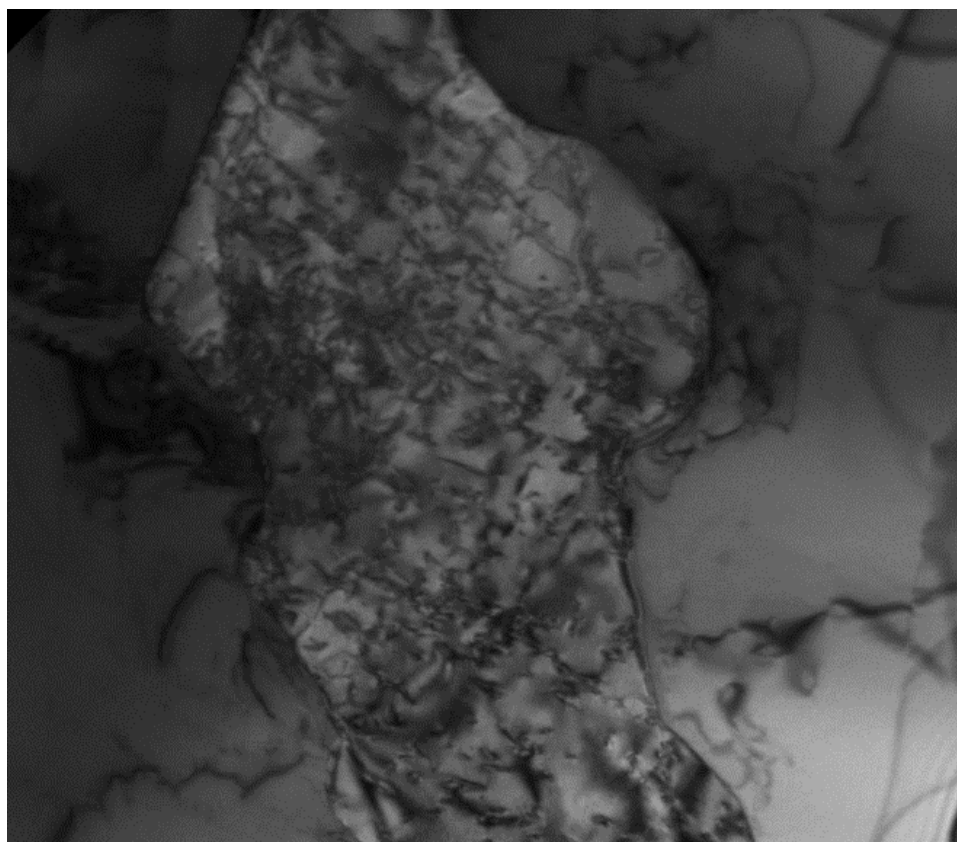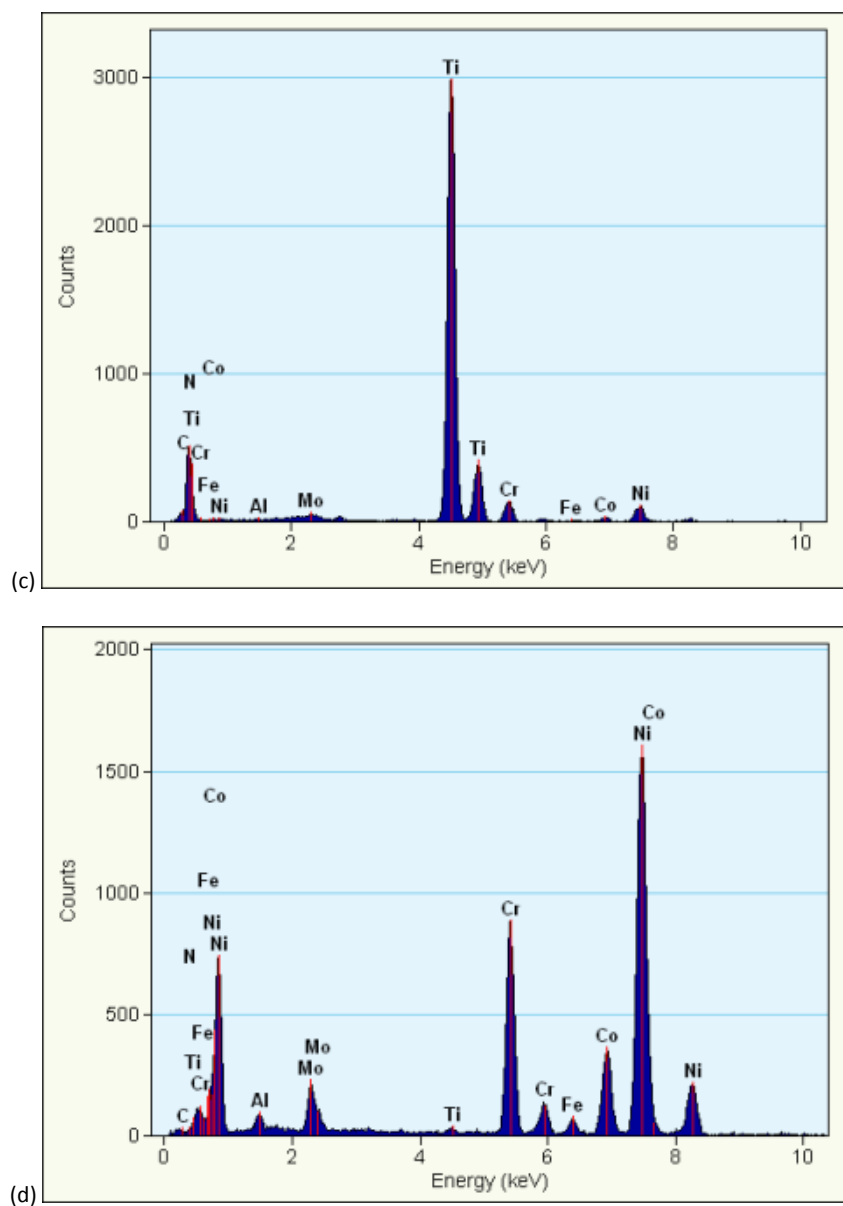
**Figure 2.3.3.11.** *(a and b)TEM images of as-received T-0-1 and XRD analysis of lighter region (c) and darker region (d).*

(a)



(b)

(c)



(d)



(e)
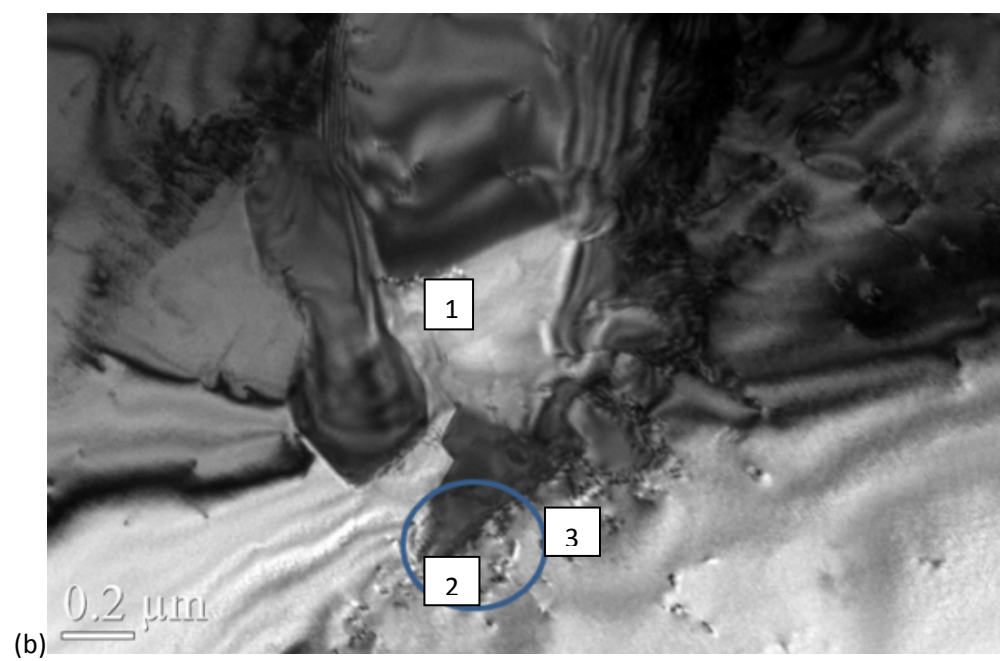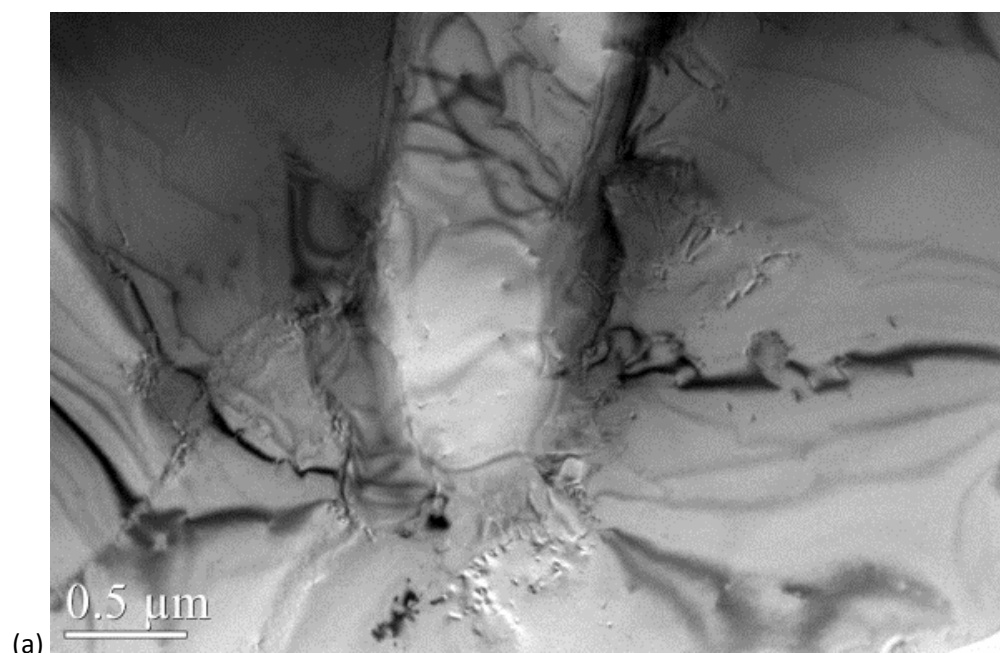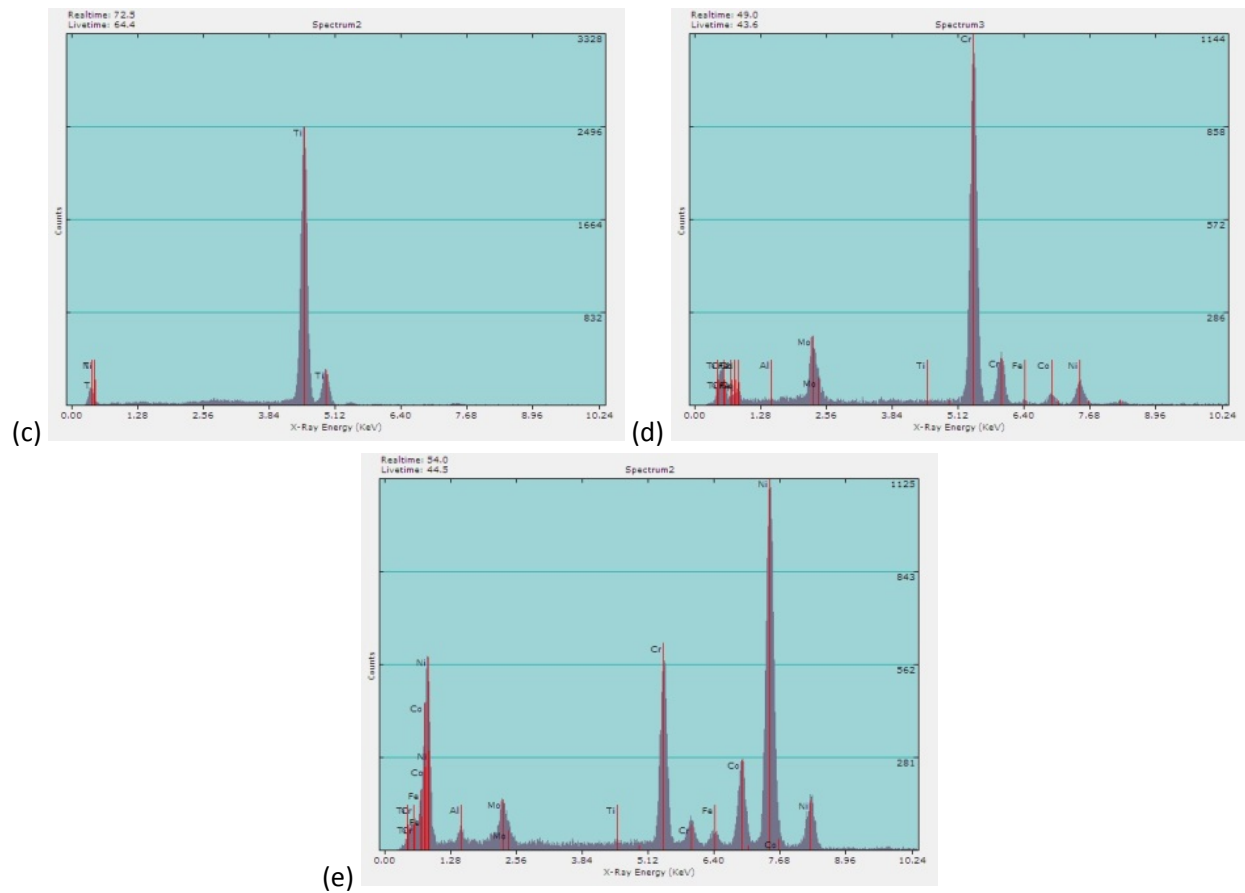
*Figure 2.3.3.12.* *(a) An unusual feature in 0° sample from specimen 617-3; (b) tilted specimen to a proper zone axis of TiN; (c) EDX of Ti-rich area 1; (d) EDX of Cr-rich area 2; and (e) EDX of area 3 matrix.*

## 2.4 Constitutive Model Development Based on Measurable Microstructural Variables

This section synthesizes an article submitted for publication and research presented at the Materials Science and Technology conference. The article was originally written in Latex, which did not make it amenable to the format of this report. The modeling in this section is critically important to the use of nonlinear ultrasonics for nondestructive damage characterization because it enables understanding of the correlation between higher harmonic generation and the underlying microstructure feature from which it results.

## 3. ACCOMPLISHMENTS

Tensile creep tests were conducted on Alloy 617 samples. Second harmonic generation measurements were made on the subset of the creep samples that were subjected to a nominal stress of 30% of the yield strength at 850C. One test was run to rupture and seven others were interrupted over a range of creep strains. With the exception of the sample that ruptured the samples exhibited steady state creep. Microscopy revealed that both void growth and dislocation density increased monotonically with creep, but that $M_{23}C_6$ precipitate size and quantity increased to a maximum and then decreased in an analogous fashion to thermal aging but with a compressed time scale. Nonlinear acoustics measurement of second harmonic generation using bulk waves revealed that the relative nonlinearity parameter (which is the modal amplitude ratio $A_2/A_1^2$) also increased to a maximum and then decreased. Both the microscopy results and the nonlinear acoustic results are in agreement with various related findings in the literature. The nonlinear acoustics results hold promise as a degradation technique despite the complex nature of creep damage because they appear to correlate to the precipitate distribution. Micromechanical modeling was initiated to develop a relationship between harmonic generation and microstructure. The modeling is intended to be applicable to both bulk wave and guided wave nonlinear ultrasonics as it is 3-dimensional rather than 1-dimensional as is typical for bulk waves. And it is expected to enable remaining useful life prediction based on the harmonic generation measurements.

Nonproportional tension-torsion cyclic loading of tubular Alloy 617 specimens enabled characterization of creep-fatigue-ratcheting material degradation from 650-950$^{\circ}$C. The tubular specimens provided a means to study higher harmonic generation with ultrasonic guided waves with two objectives; (i) characterize the degradation in the test specimens and (ii) develop a nondestructive characterization methodology for NGNP intermediate heat exchanger tubing specifically and other applications in general. While nonlinear acoustics with bulk waves is relatively mature technology, the use of guided waves to generate higher harmonics was immature, but promising and important because so many structural components are natural waveguides. Some of our important accomplishments with regard to nonlinear guided waves are listed below.

- An analysis framework based on the interaction of guided wave modes was developed to support selection of modes that generate cumulative second and third harmonics in plates. Plates were selected as a starting point because the geometry is more straight-forward than wave propagation in pipes.
- All possible primary modes that generate cumulative second harmonics were tabulated and magnetostrictive transducers were employed to demonstrate the shear-horizontal modes generate second harmonic symmetric Lamb modes.
- Time domain finite element analysis was employed to confirm theoretical model results. Simulations are also extremely valuable because the undesirable nonlinearities of measurement systems are absent.
- Nonlinear wave propagation characteristics in pipe geometries were shown to approach those characteristics in plates in the asymptotic limit.

- Analysis of higher harmonic generation in cylindrical waveguides was implemented using a curvilinear coordinate system. Thus, primary modes that generate cumulative second harmonics in pipes were identified.

- Because mode selection is so crucial when using guided waves, especially for nonlinear guided waves, the primary modes that generate cumulative second harmonics in plates and shells were tabulated. Group velocities and power flux between the primary and secondary modes were part of the tabulation.

- Numerical simulations were conducted that clearly show higher harmonic wave modes propagate independently from the primary wave mode that generates them.

- The fundamental shear-horizontal wave was shown to generate strong third harmonics of the same mode. In fact, all shear-horizontal wave modes at any frequency will generate a cumulative third harmonic mode. We call this holo-internal resonance. Primary Lamb wave modes that generate cumulative third harmonics were tabulated.

- Experimental results indicate that the third harmonic of the fundamental shear-horizontal mode are sensitive to localized plastic deformation. The amplitude of the modal ratio $A_3/A_1^3$ increases monotonically with the extent and intensity of plastic deformation. Furthermore, the modal ratio $A_3/A_1^3$ is sensitive to unseen fatigue damage; i.e., it changes due to dislocation substructures and persistent slip bands that precede macroscale crack initiation.

- Analysis of higher harmonics associated with flexural modes in pipes revealed that the internal resonance criteria can be applied to ascertain the scattering angle of the higher harmonic mode. By interpreting the flexural modes as wave modes that spiral along the pipe at a prescribed tilt angle a method of exciting a predominant flexural mode was proposed. This interpretation also enables prediction of the higher harmonic mode and its propagation direction based upon the primary wave mode or modes. Finite element simulations demonstrated and confirmed the theoretical modeling results, as well as showed the importance once again of mode selection.

- The axisymmetric torsional mode T(0,1) generated a third harmonic wave of the same mode that is sensitive to the degradation that occurred due to the nonproportional tension-torsion loading that caused creep-fatigue-ratcheting interaction in Alloy 617. Magnetostrictive transducers were used to generate and receive the guided waves in the pipe. While successful, this work is continuing as the experimental procedures are refined with an eye toward field measurements. Moreover, microscopy of these test specimens will be performed as the continuation of this research will conclude a Ph.D. thesis.

- A nonlinear acoustic guided wave spectroscopy method was developed that has several advantages over more conventional methods to detect early damage progression. The method is based on mixing two or more guided wave modes in a waveguide (e.g., pipe or plate). The interaction of these primary modes generates combinational harmonics that can be designed to occur at frequencies far from the known higher harmonics of the measurement system (e.g., integer multiples of the excitation frequencies). Thus, measurements of material nonlinearity can be made in the absence of instrument nonlinearity. Furthermore, time delays can be applied to the actuators in order to move the point of wave interaction along the material domain of interest. This scanning method enables sensitive detection of localized damage and the creation

of tomograms to visual the damage location and its extent. Finally, the method can be applied without a baseline obtained prior to damage initiation. These three features make the method attractive indeed; therefore a provisional patent has been filed with the U.S. Patent Office.

Over the course of the project 8 graduate students and 2 undergraduates have been supported and 6 theses have been completed (1 Ph.D., 3 M.S., and 2 honors). Two more Ph.D. degrees are expected this academic year. The project benefited tremendously from their efforts, and in return they were rewarded with invaluable experience.

The results of the project were widely disseminated in journals and at conferences. In total, 19 articles were published. Nine of those are in top archival journals [*J. Appl. Phys*. (4), *Ultrasonics* (2), *J. Sound & Vib*., *J. Acoust. Soc. Am*., *J. Nondestructive Eval*.]. We count a total of 19 presentations given at the following forums:

- *Review of Progress in Quantitative Nondestructive Evaluation*, Boise, Idaho, July 20-25, 2014.
- *Idaho National Laboratory*, Idaho Falls, Idaho, July 17, 2014.
- *Review of Progress in Quantitative Nondestructive Evaluation*, Baltimore, Maryland, July 21-26, 2013.
- *ASME 2013 Pressure Vessels & Piping Conference*, Paris, France, July 14-18, 2013.
- *13th International Symposium on Nondestructive Characterization of Materials*, Le Mans, France, May 20-25, 2013.
- *International Workshop on Acoustic Transduction Materials and Devices*, University Park, Pennsylvania, May 6-9, 2013.
- *Center for Acoustics and Vibration 22nd Annual Spring Workshop*, University Park, Pennsylvania, April 29-30, 2013.
- *ASNT 22nd Research Symposium*, Memphis, Tennessee, March 18-21, 2013.
- *SPIE Smart Structures/NDE*, San Diego, California, March 10-14, 2013.
- *Review of Progress in Quantitative Nondestructive Evaluation*, Denver, Colorado, July 15-20, 2012.

# PART III. LIST OF PUBLICATIONS

# 1. JOURNALS AND PROCEEDINGS

C.J. Lissenden, Y. Liu, G. Choi, X. Yao, 2014, "Effect of localized microstructure evolution on higher harmonic generation of guided waves," *J. NDE* Vol. 33:178-186.

Y. Liu, C.J. Lissenden, J.L. Rose, 2014, "Higher order interaction of elastic waves in weakly nonlinear circular cylinders. I. analytical foundation," *J. Appl. Phys*. Vol. 115:214901.

Y. Liu, E. Khajeh, C.J. Lissenden, J.L. Rose, 2014, "Higher order interaction of elastic waves in weakly nonlinear circular cylinders. II. physical interpretation and numerical simulation," *J. Appl. Phys*. Vol. 115:214902.

V.K. Chillara, C.J. Lissenden, 2014, "Nonlinear guided waves in plates: a numerical perspective," *Ultrasonics* Vol. 54, pp. 1553-1558.

Y. Liu, V.K. Chillara, C.J. Lissenden, J.L. Rose, 2013, "Cubic nonlinear shear horizontal and Rayleigh Lamb waves in weakly nonlinear plates," *J. Appl. Phys*. Vol. 114:114908.

Y. Liu, E. Khajeh, C.J. Lissenden, J.L. Rose, 2013, "Interaction of torsional and longitudinal guided waves in weakly nonlinear circular cylinders," *J. Acoustic Soc. Am*. Vol. 133(5):2541-2553.

V.K. Chillara, C.J. Lissenden, 2013, "Analysis of second harmonic guided waves in pipes using a large radius asymptotic approximation for axis-symmetric longitudinal modes," *Ultrasonics* Vol. 53:862-869.

Y. Liu, V. Chillara, C.J. Lissenden, 2013, "On selection of primary modes for generation of strong internally resonant second harmonics in plate" *J. Sound and Vibration*, Vol. 332(19):4517-4528.

V.K. Chillara, C.J. Lissenden, 2012, "Interaction of guided wave modes in isotropic nonlinear elastic plates: higher harmonic generation," *J. Appl. Phys*., Vol. 111(12) 124909 (7 pages).

September 2013, "Nonlinear ultrasonics for infrastructure management," *International Innovation*, pp. 21-23.

V.K. Chillara, C.J. Lissenden, 2014, "Guided wave mode conversions across waveguide transitions: a study using frequency domain finite element method," In: *Review of Progress in Quantitative Nondestructive Evaluation*, Vol. 33, D.E. Chimenti, L.J. Bond, D.O. Thompson, Eds., American Institute of Physics Proc. 1581, pp. 308-315.

G. Choi, Y. Liu, C.J. Lissenden, 2014, "Influence of localized microstructure evolution on second harmonic generation of guided waves," In: *Review of Progress in Quantitative Nondestructive Evaluation*, Vol. 33, D.E. Chimenti, L.J. Bond, D.O. Thompson, Eds., American Institute of Physics Proc. 1581, pp. 631-638.

Y. Liu, C.J. Lissenden, J.L. Rose, 2014, "Microstructural characterization in plates using guided wave third harmonic generation," In: *Review of Progress in Quantitative Nondestructive Evaluation*, Vol. 33, D.E. Chimenti, L.J. Bond, D.O. Thompson, Eds., American Institute of Physics Proc. 1581, pp. 639-645.

X. Yao, Y. Liu, C.J. Lissenden, 2014, "Nonlinear acoustics experimental characterization of microstructure evolution in Inconel 617," In: *Review of Progress in Quantitative Nondestructive Evaluation*, Vol. 33, D.E. Chimenti, L.J. Bond, D.O. Thompson, Eds., American Institute of Physics Proc. 1581, pp. 733-738.

Y. Liu, C. Lissenden, J. Rose, 2014, "Nonlinear ultrasonic guided waves for microstructure characterization of hollow cylinders," Symposium on Nondestructive Characterization of Materials, May 2013, www.NDT.net?ID=15519.

Y. Liu, G. Choi, C.J. Lissenden, J.L. Rose, 2013, "Effect of localized plastic deformation on higher harmonic guided wave mode generation in plate," In: *Structural Health Monitoring 2013*, F.-K. Chang, Ed., Destech, Lancaster, pp. 1992-1999.

S. Quayyum, M. Sengupta, G. Choi, C.J. Lissenden, T. Hassan, 2013, "Fatigue and ratcheting experimental responses of Alloy 617 under high temperature multiaxial loading," In: *Proceedings of the ASME 2013 Pressure Vessels & Piping Conference*, PVP2013-97252.

Y. Liu, C.J. Lissenden, J.L. Rose, 2013, "Cumulative second harmonics in weakly nonlinear plates and shells," In: *Health Monitoring of Structural and Biological Systems, Proceedings of SPIE*, Vol. 8695, T. Kundu, Ed., paper 869528, 12 pages.

V.K. Chillara and C.J. Lissenden, 2013, "Higher harmonic guided waves in isotropic weakly non-linear elastic plates," In: *Review of Progress in Quantitative Nondestructive Evaluation*, Vol. 32, D.O. Thompson and D.E. Chimenti, Eds., American Institute of Physics Proc. 1511, pp. 145-150.

Y. Liu, C.J. Lissenden, J.L. Rose, 2013, "Higher harmonic generation of guided waves in plate: power flux density and synchronism co-analysis for mode selection," In: *Review of Progress in Quantitative Nondestructive Evaluation*, Vol. 32, D.O. Thompson and D.E. Chimenti, Eds., American Institute of Physics Proc. 1511, pp. 151-158.

## 2. THESES

X. Yao, 2014, Bulk Wave Nonlinear Acoustics Evaluation of Crept Inconel 617, M.S. Thesis in Engineering Science and Mechanics, The Pennsylvania State University, University Park, PA.

Y. Liu, 2014, Characterization of global and localized material degradation in plates and cylinders via nonlinear interaction of ultrasonic guided waves, Ph.D. Thesis in Engineering Science and Mechanics, The Pennsylvania State University, University Park, PA.

G. Choi, 2013, Creep-fatigue-ratcheting behavior of Haynes 230 via isothermal multiaxial experimentation, M.S. Thesis in Engineering Mechanics, The Pennsylvania State University, University Park, PA.

V.K. Chillara, 2012, Higher harmonic guided waves in isotropic weakly non-linear elastic plates, M.S. Thesis in Engineering Mechanics, The Pennsylvania State University, University Park, PA.

B. Corl, 2013, Microstructural evolution of Inconel 617, Honors Thesis in Engineering Science, The Pennsylvania State University, University Park, PA.

J. Weigle, 2013, Nonlinear acoustic solutions for the nondestructive evaluation of Alloy 617, Honors Thesis in Engineering Science, The Pennsylvania State University, University Park, PA.

## 3. PRESENTATIONS (presenting author in **bold**)

V.K. **Chillara**, C.J. Lissenden, "Nonlinear guided waves in plates undergoing localized micro-structural changes," *Review of Progress in Quantitative Nondestructive Evaluation*, Boise, Idaho, July 20-25, 2014.

G. **Choi**, Y. Liu*, X. Yao, C.J. Lissenden, "Effect of localized microstructural evolution on higher harmonic generation of guided wave modes," *Review of Progress in Quantitative Nondestructive Evaluation*, Boise, Idaho, July 20-25, 2014.

Y. **Liu**, C.J. Lissenden, J.L. Rose, "NDE and SHM of pipes with acoustic guided wave: from macro to micro scale damages," *Review of Progress in Quantitative Nondestructive Evaluation*, Boise, Idaho, July 20-25, 2014.

G.W. Choi*, M. Sengupta*, C.J. **Lissenden**, "Creep-fatigue-ratcheting experiments on Inconel 617 at several temperatures," *Idaho National Laboratory*, Idaho Falls, Idaho, July 17, 2014.

V.K. **Chillara***, C.J. Lissenden, "Nonlinear guided waves in plates undergoing localized micro-structural changes," *Idaho National Laboratory*, Idaho Falls, Idaho, July 17, 2014.

G. **Choi***, Y. Liu*, X. Yao*, C.J. Lissenden, "Effect of localized microstructural evolution on higher harmonic generation of guided wave modes," *Idaho National Laboratory*, Idaho Falls, Idaho, July 17, 2014.

Y. **Liu***, C.J. Lissenden, J.L. Rose, "NDE and SHM of pipes with acoustic guided wave: from macro to micro scale damages," *Idaho National Laboratory*, Idaho Falls, Idaho, July 17, 2014.

V.K. **Chillara**, C.J. Lissenden, "Guided wave mode conversion across waveguide transitions: a study using frequency domain finite element approach," *Review of Progress in Quantitative Nondestructive Evaluation*, Baltimore, Maryland, July 21-26, 2013.

G. **Choi**, Y. Liu*, C.J. Lissenden, "Influence of local microstructure evolution on higher harmonic generation of guided waves," *Review of Progress in Quantitative Nondestructive Evaluation*, Baltimore, Maryland, July 21-26, 2013.

Y. Liu, C.J. **Lissenden**, J.L. Rose, "Characterization of microstructure evolution in plates using guided wave third harmonics," *Review of Progress in Quantitative Nondestructive Evaluation*, Baltimore, Maryland, July 21-26, 2013.

X. **Yao**, Y. Liu, C.J. Lissenden, "Nonlinear acoustics experimental characterization of microstructure evolution in Inconel 617," *Review of Progress in Quantitative Nondestructive Evaluation*, Baltimore, Maryland, July 21-26, 2013. (poster)

S. Quayyum, M. Sengupta, G. Choi, C.J. Lissenden, T. **Hassan**, "Fatigue and ratcheting experimental responses of Alloy 617 under high temperature multiaxial loading," *ASME 2013 Pressure Vessels & Piping Conference*, Paris, France, July 14-18, 2013.

Y. Liu, C.J. **Lissenden**, J.L. Rose, "Nonlinear ultrasonic guided waves for microstructure characterization of hollow cylinders," 13th International Symposium on Nondestructive Characterization of Materials, Le Mans, France, May 20-25, 2013.

Y. **Liu**, C.J. Lissenden, J.L. Rose, "Characterization of material microstructural evolution by nonlinear elastic waves," *International Workshop on Acoustic Transduction Materials and Devices*, University Park, Pennsylvania, May 6-9, 2013.

C.J. Lissenden, "Systems and structures health management," Center for Acoustics and Vibration 22nd Annual Spring Workshop, University Park, Pennsylvania, April 29-30, 2013.

Y. **Liu**, C.J. Lissenden, and J.L. Rose, "Conditions for cumulative second harmonic generation in plates and pipes," *ASNT 22nd Research Symposium*, Memphis, Tennessee, March 18-21, 2013.

Y. Liu, C.J. **Lissenden**, and J.L. Rose, "Cumulative second harmonics in weakly nonlinear plates and shells," *SPIE Smart Structures/NDE*, San Diego, California, March 10-14, 2013.

Y. **Liu**, C.J. Lissenden, J.L. Rose, "Higher harmonic generation of guided waves in plate: power flux density and synchronism co-analysis for mode selection," *Review of Progress in Quantitative Nondestructive Evaluation*, Denver, Colorado, July 15-20, 2012.

V.K. **Chillara** and C.J. Lissenden, "Higher harmonic guided waves in isotropic weakly non-linear elastic plates," *Review of Progress in Quantitative Nondestructive Evaluation*, Denver, Colorado, July 15-20, 2012.

# PART IV. FINAL QUAD CHART

# PART V. OTHER RELEVANT INFORMATION

# Graduate Student Support and Degrees Earned

The project supported a number of graduate students, whom are listed below along with the degrees that were earned.

Yang Liu, PSU, ESM, China, PhD August 2014

Brian Reinhardt, PSU, ESM, USA, PhD in-progress

Gloria Choi, PSU, ESM, USA, MSEM December 2013, PhD in-progress

Vamshi Chillara, PSU, ESM, India, MSEM May 2012, PhD expected May 2015

Hwanjeong Cho, PSU, ESM, South Korea, PhD in-progress

Xiaochu Yao, PSU, ESM, China, MSEM December 2014

Brett Corl, PSU, ESM, USA, BSES May 2013

John Weigle, PSU, ESM, USA, BSES May 2013

Fengtao Bai, NCSU, CE, China

Paul Barrett, NCSU, CE, USA, PhD expected May 2015

**Appendix A (292 pages):**
**Creep-Fatigue-Ratcheting Experiments on Inconel 617 at Several Temperatures**

**(originally submitted along with NEUP quarterly report Year 4 Quarter 2)**

**Appendix B (76 pages):**

**Bulk Wave Nonlinear Acoustics Evaluation of Crept Inconel 617**

**(M.S. thesis of Xiaochu Yao, Fall 2014)**

## Appendix C (103 pages):

## Nonlinear Ultrasonic Guided Waves for Microstructure Characterization

## Key Publications

V.K. Chillara, C.J. Lissenden, 2012, "Interaction of guided wave modes in isotropic nonlinear elastic plates: higher harmonic generation," *J. Appl. Phys*., Vol. 111(12):124909.

Y. Liu, V.K. Chillara, C.J. Lissenden, J.L. Rose, 2013, "Cubic nonlinear shear horizontal and Rayleigh Lamb waves in weakly nonlinear plates," *J. Appl. Phys*. Vol. 114:114908.

Y. Liu, C.J. Lissenden, J.L. Rose, 2014, "Higher order interaction of elastic waves in weakly nonlinear circular cylinders. I. analytical foundation," *J. Appl. Phys*. Vol. 115:214901.

Y. Liu, E. Khajeh, C.J. Lissenden, J.L. Rose, 2014, "Higher order interaction of elastic waves in weakly nonlinear circular cylinders. II. physical interpretation and numerical simulation," *J. Appl. Phys*. Vol. 115:214902.

Y. Liu, V. Chillara, C.J. Lissenden, 2013, "On selection of primary modes for generation of strong internally resonant second harmonics in plate" *J. Sound and Vibration*, Vol. 332(19):4517-4528.

Y. Liu, E. Khajeh, C.J. Lissenden, J.L. Rose, 2013, "Interaction of torsional and longitudinal guided waves in weakly nonlinear circular cylinders," *J. Acoustic Soc. Am*. Vol. 133(5):2541-2553.

V.K. Chillara, C.J. Lissenden, 2013, "Analysis of second harmonic guided waves in pipes using a large radius asymptotic approximation for axis-symmetric longitudinal modes," *Ultrasonics* Vol. 53:862-869.

V.K. Chillara, C.J. Lissenden, 2014, "Nonlinear guided waves in plates: a numerical perspective," *Ultrasonics* Vol. 54, pp. 1553-1558.

Y. Liu, C.J. Lissenden, J.L. Rose, 2013, "Cumulative second harmonics in weakly nonlinear plates and shells," In: *Health Monitoring of Structural and Biological Systems, Proceedings of SPIE*, Vol. 8695, T. Kundu, Ed., paper 869528, 12 pages.

C.J. Lissenden, Y. Liu, G. Choi, X. Yao, 2014, "Effect of localized microstructure evolution on higher harmonic generation of guided waves," *J. NDE*, Vol. 33:178-186.